Support Influence of Metallocene Catalysts on Ethylene Polymerization Activity

written by
Thimo S. Jacobs, BSc

February 2019

Support Influence of Metallocene Catalysts on Ethylene Polymerization Activity

Thimo S. Jacobs, BSc

Supervisors:
Silvia Zanoni, MSc
Dr. Florian Meirer
Prof. dr. ir. Bert M. Weckhuysen

In cooperation with Total Research and Technology, Feluy, Belgium

A thesis presented for the degree of
Master of Science

Inorganic Chemistry and Catalysis
Debye Institute for Nanomaterials Science
Utrecht University

February 2019

Abstract

Metallocenes give the possibility to tailor the structure of polymers in a way that has not been reached before by either Phillips or Ziegler-Natta catalysts. Heterogeneous metallocene catalysts are activated by methylaluminoxane (MAO) and generally supported on porous materials, overcoming the issues of reactor fouling and lack of morphology control that are present when metallocenes are used as homogeneous catalysts. It was reported that the polymerization activity was enhanced significantly (35%) upon the addition of titanium to the silica support, which resulted in a study to clarify the role of titanium in the support. In this thesis, several characterization techniques were used to study the promotor effect of titanium. First of all, the structure of the catalyst was characterized with both Fourier Transform Infrared (FTIR) spectroscopy and Scanning Electron Microscopy (SEM). The structural aspects of the bare supports, the supports after MAO impregnation and the full catalysts were studied. Next to that, FTIR spectroscopy with pyridine as probe molecule was used to study the Lewis acidity of these samples. It was verified that the catalyst acidity was not affected significantly by the addition of titanium as promotor, hence the acidity proved to be not the main contributing factor towards the significant increase in activity upon titanium addition. Diffuse Reflectance Infrared Fourier Transform Spectroscopy (DRIFTS) was used subsequently to study the fragmentation kinetics of ethylene polymerization. By performing *in situ* measurements on the samples, a trend in fragmentation time was observed, indicating an optimum of around 2-4 wt% titanium in the support. Finally, the catalysts were studied with Confocal Fluorescence Microscopy (CFM). The catalyst particles were stained with perylene and PTCDA to obtain fluorescence. The fluorescent particles were used for autoclave polymerization and studied afterwards using the CFM, which visualized the fragmentation and enabled the possibility to reconstruct the surface of the particle after polymerization. The combination of these techniques gave insight into the role of the titanium on the polymerization behavior of metallocene catalysts.

Contents

Figures

Tables

Abbreviations

MAO Methylaluminoxane

PE Polyethylene

PVC Polyvinylchloride

PET Polyethylene terephthalate

LDPE Linear low density polyethylene

LLDPE Low density polyethylene

HDPE High density polyethylene

TMA Trimethylaluminum

DCM Dichloromethane

Me Methyl group

Bu Butyl group

R Alkyl group

FTIR Fourier Transform Infrared

NMR Nuclear Magnetic Resonance

DRIFTS Diffuse Reflectance Infrared Fourier Transform Spectroscopy

CFM Confocal Fluorescence Microscopy

SEM Scanning Electron Microscopy

EDX Energy Dispersive X-ray Spectroscopy

ATR Attenuated Total Reflectance

UV/Vis Ultraviolet and Visible

LMCT Ligand-to-Metal Charge Transfer

MLCT Metal-to-Ligand Charge Transfer

Introduction

General introduction

Since the demand for polyolefins is continuously growing (estimated to be around 270 billion US dollars, an increase of 50% in five years), the interest of both the commercial and scientific fields towards polymerization catalysts is still vibrant [1]. The commercial market exhibits significant attention in high quality polymers, due to their enhanced sustainability. The ideal catalysts that allow for the synthesis of such polymers are metallocenes, which are organometallic structures that have a constrained metal atom in the center of two organic ligands. This metal atom can be active for olefin polymerization. The commercial value of these catalysts has increased enormously over the past three decades, since the characteristics of the polymers synthesized by this type of catalyst can be controlled in a way that has not been reached before by either Phillips of Ziegler-Natta catalysts [2, 3]. In the early days (around the 1980s), metallocenes were used as homogeneous catalysts, since this resulted in the highest activity. However, employing homogeneous catalysis for olefin polymerization has two disadvantages: reactor fouling and lack of control over polymer morphology [4]. Therefore, in order to be used as industrial catalysts, the metallocenes are generally immobilized on a support. This support typically consists of porous silica. The first generation of supported metallocene catalysts had a lowered activity when compared to their homogeneous equivalents, because the diffusion of the monomer into the pores of the catalyst is slower and the number of active centers is reduced [5]. In recent research however, researchers at Total found that the addition of a few weight percent titanium to the porous silica support significantly increases the olefin polymerization activity [6]. The reason(s) for this increase in activity upon titanium addition remain unknown and are relevant for understanding of the polymerization mechanism. A few possibilities are presented, namely the increase in acidity, number of active sites and/or the easier fragmentation of the support. In this thesis, the goal is to characterize the supports with different loadings of titanium by using several spectroscopic/microscopic techniques and understand the reason(s) for the significant increase in polymerization activity.

Polymers and Polyolefins

Polymers comprise a group of materials that consists of multiple linked monomers. These monomers are the building blocks for the structure and determine the chemical and physical properties of the material. Polymers can range from biopolymers, such as DNA and RNA, to industrially produced polymers like polyvinylchloride (PVC) or polyethylene terephthalate (PET). Due to their unique range of properties, such as toughness or visco-elasticity, polymers are of great interest in modern day science. Since polymers have a great number of applications, *e.g.* in plastics, adhesives or even resistant paints, their economical value is large. Synthesized by linking multiple units of ethylene, polyethylene is economically the most interesting polymer. Polyethylene alone has a demand for roughly 100 million metric tons (in 2018 alone), worth around $160 billion [1].

Polyethylene (PE) can be divided in three main different classes of polyethylene, namely high density PE (HDPE), low density PE (LDPE) and linear low density PE (LLDPE). HDPE is built up from linear chains with a few short branches. LLDPE is also a linear chain, however due to the copolymerization with higher 1-olefins, it forms a large number of branches. Finally, the third class of polyethylene is LDPE. LDPE has a main chain with randomly distributed longer and/or shorter side chains. In Figure 1.1, the three main classes of polyethylene are shown schematically. The differences in structure of the polyethylene classes are due to the different polymerization procedures, conditions and catalysts that are used to synthesize them. HDPE and LLDPE are synthesized by both homogeneous and heterogeneous catalysts (Phillips/Ziegler-Natta and metallocenes) at a temperature range of 353-463 K and with pressures of ethylene below 50 bar. On the contrary, LDPE is produced with free radical polymerization, which requires a higher temperature (523-573 K) and higher ethylene pressures (more than 50 bar) [7].

These three different classes of polyethylene are applied in different fields, due to their differences in properties. These differences in properties arise from the amount of branches that are present along backbone chain structure. In the case of HDPE, there is a low number of branches, which allows the polyethylene to organize in a highly crystalline material (hence the high density). This high crystallinity results in a material that has a high stiffness and low permeability [8]. HDPE is therefore used in for example the packaging of liquids, such as milk bottles or chemical storage tanks. It is also used in the toy industry, since this is type of PE is both rigid and translucent. Since LDPE has a higher number of branches, their ability to crystallize is hindered (resulting in a lower density). LDPE is used in plastic bags, since this type of PE has waxy solid properties. Generally, LLDPE is used in the same field of applications as LDPE. However, since LLDPE has slightly better properties (higher strength and flexibility), it is used to produce thinner films than possible with LDPE.

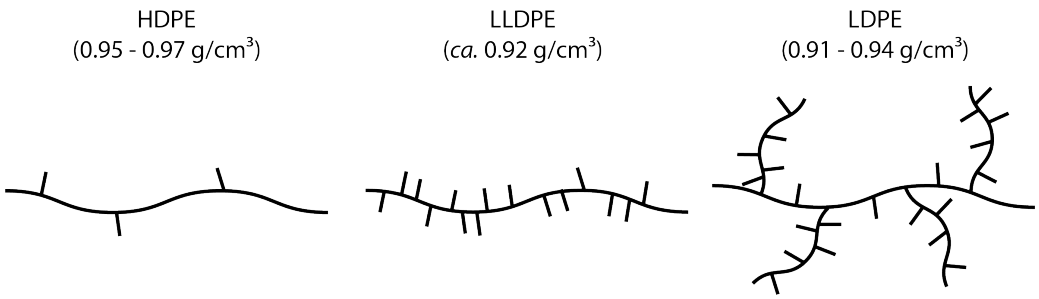

Figure 1.1: Overview of the different types of polyethylene, with included the densities [9].

Tacticity

Tacticity is the term used to describe the stereochemistry of adjacent repeating units of a polymer. It determines the physical properties of the polymer, such as the rigidity, melting point, solubility and mechanical properties. There are three main types of tacticity, shown in Figure 1.2: isotactic, syndiotactic and atactic. With isotactic polymers, all the substituents of the polymer are located on the same side of the polymer. In the case of a syndiotactic polymer, the substituents have alternating positions along the chain. The last type of tacticity that can be found is atactic, in which the substituents are distributed randomly across the polymer chain. When using metallocene catalysts, the ligands of the metallocene are the main factor contributing towards the different types of tacticity [10]. Their steric hinderance prevents certain types of olefin insertion (explained on page 18) from occuring.

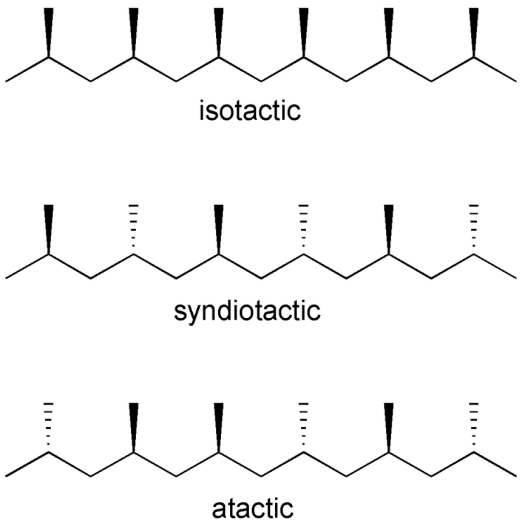

Figure 1.2: Schematic overview of the three types of tacticity that can be found in a polymer. Figure obtained from the paper of Hagen *et al.* [11].

As mentioned before, the tacticity determines the properties of the formed polymer. Isotactic polymers are the most interesting form in terms of their commercial application. These polymers exhibit high melting points, high mechanical strength (due to their crystallinity) and good workability. In the case of syndiotactic polypropene, the polymer is a rubber-like material with potential applicability. When polymers are formed with free radical polymerization, these polymers are usually atactic. A well-known example of this is the polymer polyvinylchloride. Soon after the discovery of Ziegler–Natta polymerization it was found that the use of solid-state catalysts in the polymerization of propene leads to the formation of polymers with high degrees of isotacticity. Syndiotactic polypropene was formed as well, but in very small quantities only. Metallocenes were the first olefin polymerization catalysts to form syndiotactic polypropylene and polystyrene, since the active sites of metallocenes are almost identical throughout a catalyst batch [12].

Polymerization catalysts

The aforementioned types of polyethylene are nowadays catalyzed by using either the Phillips catalyst, the Ziegler-Natta catalyst or the metallocene catalyst. The latter is the catalyst of interest for this thesis and will be discussed on the next page, but to give a broad overview, other types of polymerization catalysts are covered in this paragraph.

Phillips Catalyst

The Phillips catalyst (Figure 1.3a), discovered in the early 1950's by Hogan and Banks at the Phillips Petroleum Company, is one of the most important industrial catalysts for ethylene production [13]. First patented in 1953 and used for commercial applications four years later, Phillips catalysts are heterogeneous catalysts based on a metal oxide, generally chromium oxide (CrO_3), supported on silica (SiO_2) followed by calcination in dry air at high temperatures. It's the most used catalyst for the production of HDPE, comprising almost half of the market share [14].

Ziegler-Natta Catalyst

The Ziegler-Natta catalyst (Figure 1.3b) was discovered in the laboratories of K. Ziegler and G. Natta at almost the same time as the Phillips catalyst [15]. This catalyst is often referred as the most flexible polymerization catalyst used in the polymerization industry. However, this flexibility makes it difficult to define the structure of a Ziegler-Natta catalyst. It consists of a transition metal salt ranging from group 4 to 8 of the periodic table in association with a metal alkyl from group 1, 2 or 13 (which functions as the cocatalyst) [8]. This cocatalyst is required to form the active species by alkylation and possibly reduction of the transition metal center. The most common example of Ziegler-Natta catalysts is titanium tetrachloride ($TiCl_4$), activated by triethylaluminum ($AlEt_3$) and supported on $MgCl_2$.

Late Transition Metals Catalysts

This type of polymerization catalyst was discovered in the early 1990s by researchers at DuPont. Unique about this type of catalyst is that they are much less sensitive to polar compounds, when compared to Ziegler-Natta, Phillips or metallocene catalysts. This allows the copolymerization of olefins and polar comonomers, such as vinyl acetate and methyl methacrylate [16]. One example of this is the Ni-diimine catalyst, which successfully copolymerized ethylene with acrylate comonomers. However, these type of copolymers were only produced academically and are not (yet) industrially available.

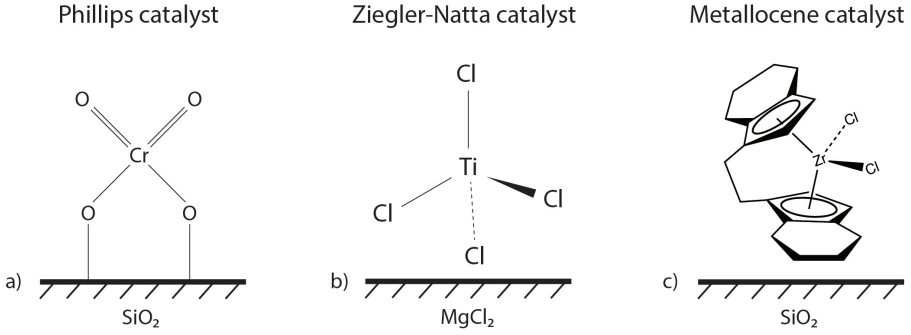

Figure 1.3: Overview of the main three types of polymerization catalysts.

Metallocene catalysts

A metallocene is an organometallic structure which consists of two organic (π-carbocyclic) ligands and a metal center. These organic ligands essentially 'sandwich' the metal, leading to a constrained metal center that is sterically hindered. First reported in 1951, by both Kealy *et al.* and Miller *et al.*, was the metallocene ferrocene [17, 18]. This metallocene consists of two cyclopentadienyl rings with a central iron atom. It was later discovered by Wilkonson *et al.* that all the carbon atoms of the cyclopentadienyl contribute equally to the bonding with the central iron atom, a breakthrough that earned him a shared Nobel Prize with Ernst Fischer in 1973 [19]. With regard to olefin polymerization, that metal center needs to be a metal from group 4 of the periodic table (e.g. Ti, Zr and Hf). Another aspect of the metallocene for olefin polymerization that differs from ferrocene is the bridge between the two organic ligands, which makes it a so called *ansa*-metallocene. This bridge can be used to selectively tune the tacticity of the polymer, a topic that was discussed on page 12 [20]. In the scope of this thesis, the metallocene catalyst that is used is built up from two bridged organic indenyl ligands and a zirconium metal center. The structure of this metallocene is shown in Figure 1.4.

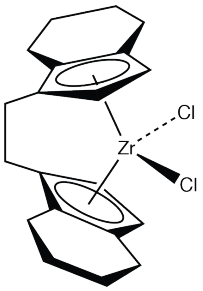

Figure 1.4: Structure of the used metallocene, dichloro [rac-ethylenebis (4,5,6,7-tetrahydro-1-indenyl)] zirconium(IV).

Metallocenes were in the early days used as homogeneous catalysts, however due to the lack of control over polymer morphology and reactor fouling, the catalysts are nowadays used on a support [4]. In comparison to the Ziegler-Natta catalysts, the metallocene catalysts are referred to as single-site catalysts, due to the equality of the active sites [21]. As can be seen from the work of Olabisi *et al.*, the difference between Ziegler-Natta and metallocene catalysts is more extensive. Metallocenes lead to a narrow molecular weight distribution, uniform chain length, low solubility and electron donors are not needed in the catalyst [21]. Already in 1957, Natta and Breslow used metallocene catalysts for mechanistic studies of ethylene polymerization [22]. However, a breakthrough occured in 1980 when Kaminsky *et al.* found that when water and trimethylaluminum were added in a 1:1-ratio (which forms MAO) during the polymerization, the catalytic activity improved [23, 24]. The combination of MAO and the metallocene led to the breakthrough in the development of these catalysts for olefin polymerization, since the activity was sufficiently high to be industrially viable. As mentioned in the general introduction, the activity is still lower than the homogeneous metallocene catalysts, but the advantages are worth the effort and compensate this lowered activity. The mechanism for the formation of the polymers will be explained on the next page.

Polymerization mechanism

The polymerization of lower olefins is achieved via the chain-growth polymerization mechanism. In this mechanism, carbon molecules with double (or triple) bonds are linked together and form a repeating chain of the starting units. This mechanism is in literature also referred to as the Cossee-Arlman mechanism. As a model system for the explanation of this mechanism, the monomer 1-hexene is used in this case. The reaction mechanism is divided into several steps. First of all, the metallocene is activated by MAO, as will be explained on the next page. Afterwards the reaction is initiated by insertion of the first monomer of 1-hexene. By the continuous addition of monomers, a longer chain is formed (the propagation). This propagation can occurs via the 1,2-insertion or the 2,1-insertion (misinsertion). If that misinsertion occurs, two things can happen: either recovery to a 'normal' chain or the formation of a dormant site, an inactive catalyst site that lowers the rate of polymerization. The reaction is finished when β-hydride elimination occurs, which results in the formation of either a vinylidene (1,2-insertion) or vinylene (2,1-insertion) product [25,26]. As can be found in literature, the polymerization reaction with metallocenes mainly proceeds via the 1,2-insertion mechanism [27, 28]. For the polymerization testing that will be explained on page 27, the terms vinylidene and vinylene are of importance for the understanding of the results.

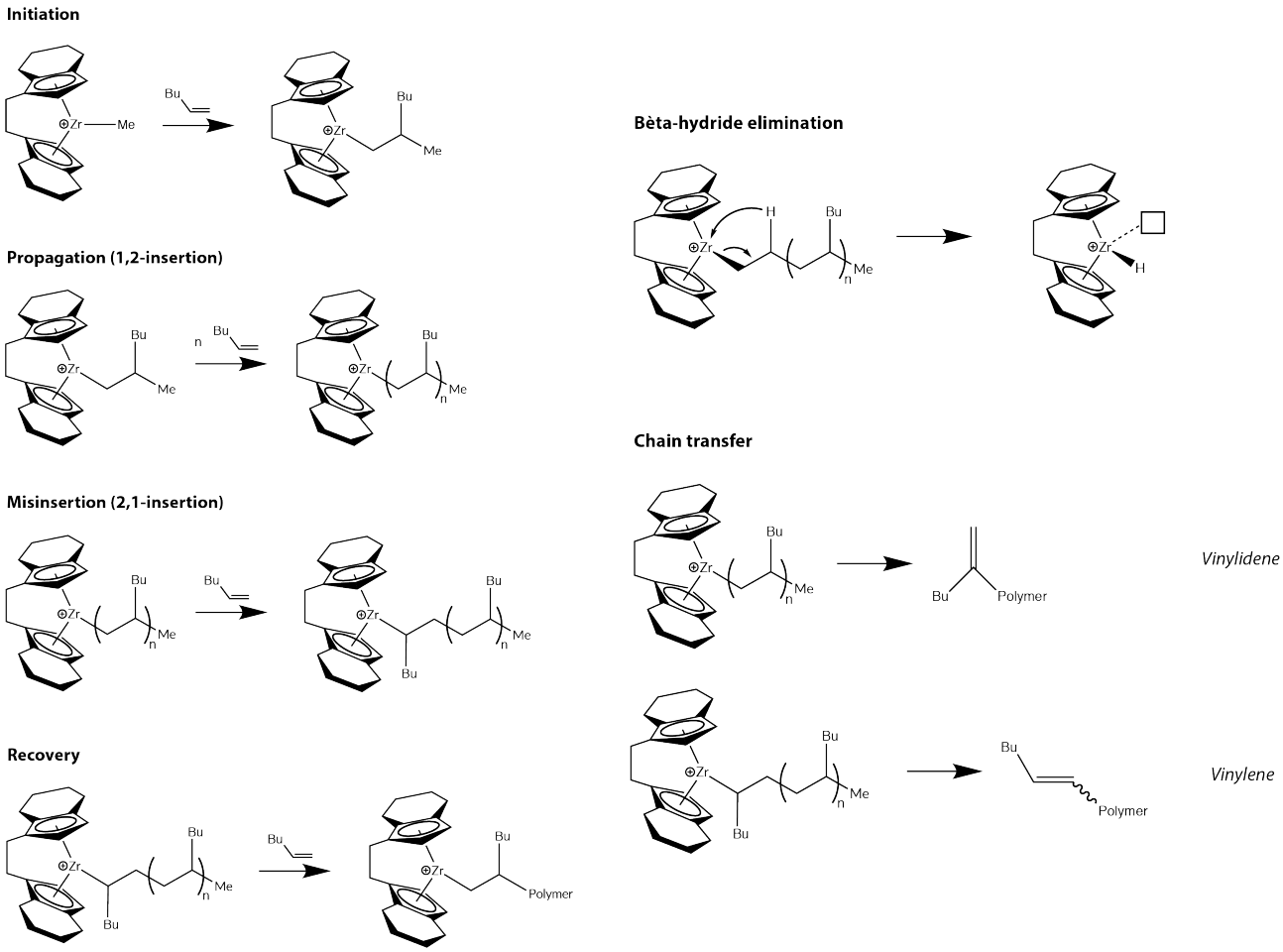

Figure 1.5: Elementary reaction steps of the polymerization reaction for the catalyst studied in this thesis.

Methylaluminoxane

The role of methylaluminoxane as co-catalyst for the polymerization reaction boosted the use of heterogeneous metallocene catalysts for olefin polymerization. However, the structure of MAO is still unknown. Various structural models for MAO have been proposed since the initial discovery, however none of these models is generally accepted. The difficulty in clarifying the structure of MAO lies in the multiple equilibria that are formed during the hydrolysis of trimethylaluminum (TMA), next to the interaction between MAO and TMA [29]. Since the exact structure is not known, MAO is generally referred to as $(AlOMe)_n$, which is schematically shown in Figure 1.6. Each aluminum atom in the structure binds as a central atom to either a methylgroup or an oxygen atom.

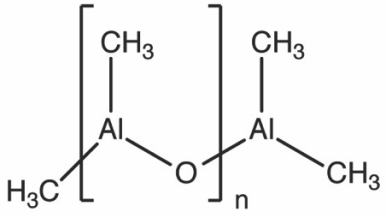

Figure 1.6: Schematic overview of the general structure of methylaluminoxane.

The MAO/TMA mixture serves as co-catalyst for the metallocene, and it is generally accepted that this activates the metallocene, creating a positively charged metal center and a vacant site for olefin insertion, as shown in Figure 1.7. MAO acts as a strong Lewis acid in this process [30]. A more elaborate activation mechanism was proposed by researchers from our group [31]. Reported in this paper is that the initial metallocene is activated by charged aluminummethyl ($AlMe_2^+$) species. However, in this first step it is also possible that the metallocene deactivates (by reacting with the silanol groups of the support) or that it adopts a resting state polymeric form (in equilibrium with the initial metallocene). If the metallocene reacts with the charged aluminummethyl species, it can form the final form as shown in Figure 1.7. However, the researchers found that the monomeric cation is not stable on the metallocene surface, so it is instead present as a metallocene polymer. In addition to its role of metallocene activation, MAO is also used as a scavenger for the surface hydroxyl groups of the support, preventing metallocene deactivation. The third and final role of MAO is to prevent leaching of the metallocene from the surface of the support [32]. As can be concluded from the past two paragraphs, both the metallocenes and the MAO have been studied extensively. However, another important parameter for the activity of the catalyst is the support, which will explained on the next page.

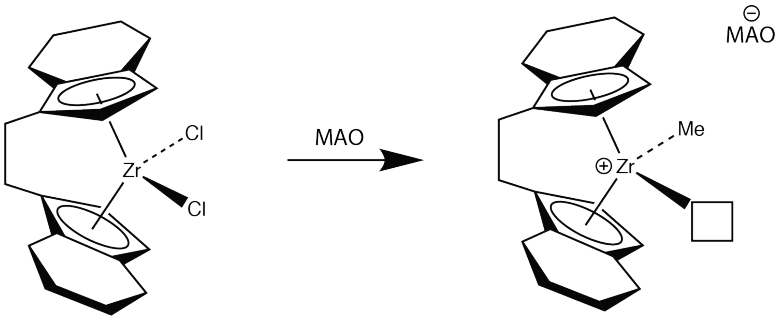

Figure 1.7: Schematic overview of the activation of the metallocene by using methylaluminoxane (MAO), creating a positively charged metal center and a vacant site for olefin insertion.

Support of the metallocene catalyst

Both the prevention of reactor fouling and a regular morphology of the polymers are the reasons why it is favorable to support the metallocenes instead of performing olefin polymerization catalyzed by a homogeneous catalyst. The most commonly used support for metallocene catalysts consists of porous silica, mainly known for its thermal stability and low cost. The support plays a key role in the rate of fragmentation: it should be friable enough to fragment, but strong enough to withstand the reactor conditions and transport [33]. The following section (page 18) will focus on why fragmentation is an important and necessary phenomenon in heterogeneous polymerization catalysis. Metallocenes can be immobilized on solid supports in different ways, but in this thesis, the MAO acts as anchor between the silica and the metallocene. The catalyst is built up by adding first the MAO and afterwards the metallocene. A schematic overview of the complete structure is shown in Figure 1.8.

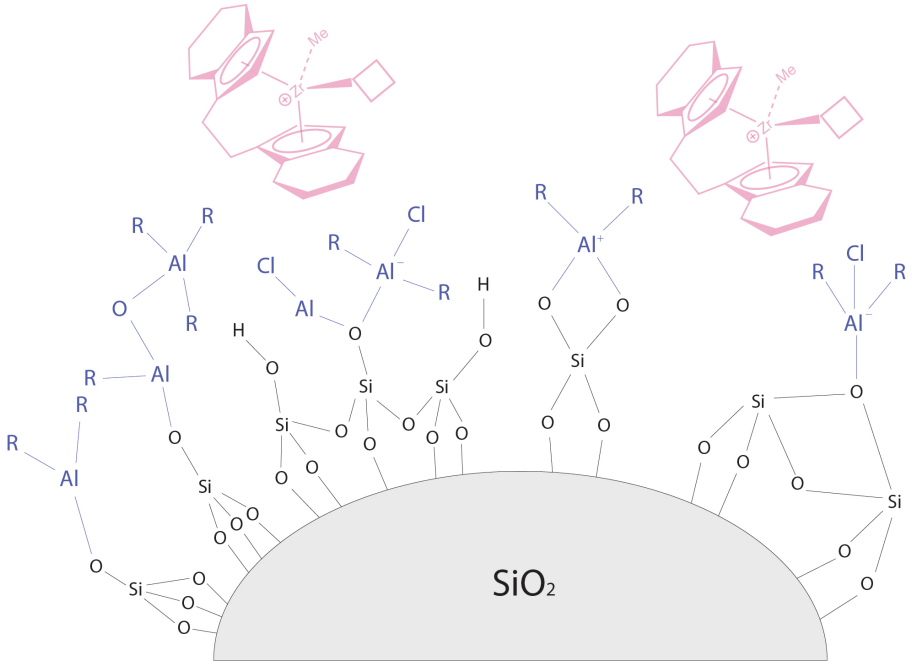

Figure 1.8: Schematic overview of the catalyst structure, which consists of silica (black), MAO (blue) and metallocene (pink). Only the surface groups are shown for clarity.

As mentioned in the introduction, the addition of a few weight percent titanium incorporated into the silica support results in activity enhancements of up to 40%, as reported in a patent from Total [6]. Several attempts have already been made to titanate the supports used for metallocene catalysts [4,34]. It was found by Jongsomjit *et al.* that when 20 wt% titania was added to the support, creating a silica/titania support, the activity increased by 25-30%. They proposed that the titania acts as a spacer to anchor the MAO to the silica support, which should lead to less steric hinderance and interactions on the support surface [35]. The downside of the created mixed supports is that little morphological control can be obtained and that these supports are difficult to use in industry, since the porous volume and particle size did not match for the silica and titania. Next to this, they also found that when larger amounts of titania were added, the activity decreased. They reasoned that this was due to the strong support interactions between titania and MAO [36]. These downsides of the early-stage titanations of a silica support resulted in the approach of Total, since they synthesized a support that overcomes these drawbacks, thereby further increasing the activity of the metallocene catalyst for olefin polymerization.

Fragmentation of the metallocene catalyst

The term fragmentation has already been mentioned a few times, which is common practice in the case of polymerization catalysts. However, when looking to a broader scope of inorganic catalysts in general, fragmentation is a less used term. Where fragmentation normally results in loss of the catalyst morphology and thereby a lowered activation, it is crucial in the case of polymerization catalysts to form polymers. This is because the reaction involves the conversion of a gas feed (monomer) into solid materials (polymers). Therefore it is of huge interest in both academics and industry that the support of the polymerization catalyst is optimized to achieve the best fragmentation possible. Named as one of the reasons for the significant increase in polymerization activity after the addition of a few weight percent of titanium, it is evident that the fragmentation (both time and method of fragmentation) needs to be studied during this thesis. In the work from Alizadeh *et al.*, it is shown that the fragmentation process can be divided in several steps, as shown in Figure 1.9. First of all, the initial porous support structure of the metallocene is shown. After the initial addition of monomer, the polymer agglomerates at the active sites (metallocenes) of the catalyst. Due to the local stress build-up of the inorganic support when polymer starts forming, the particle breaks at the weaker points of the support into smaller fragments. This process of expansion and fragmentation continues until the catalyst particles are removed from the reactor or when they are completely deactivated. Due to this fragmentation, the particle size of a catalyst particle increases significantly from roughly 50-60 μm to a polymer-covered particle with sizes up to 1-2 mm [33].

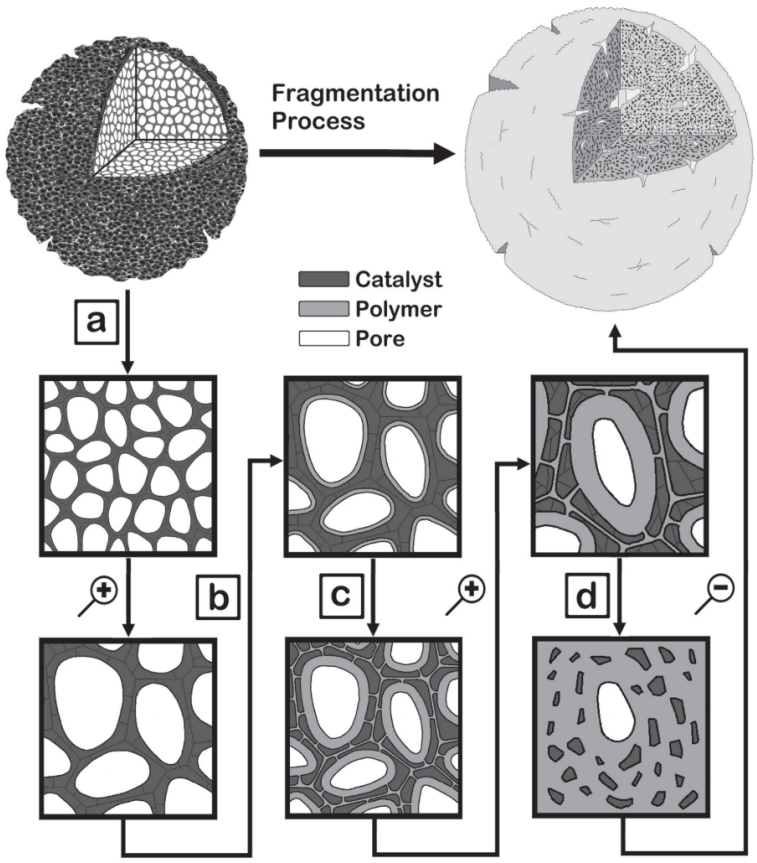

Figure 1.9: Schematic presentation of fragmentation process with a) initial porous structure of the catalyst particle, b) polymer agglomeration at the active sites of the catalyst support, c) start of the catalyst fragmentation, d) breaking of the catalyst support into the smallest fragments possible. Figure obtained from the paper of Alizadeh *et al.* [33].

Two main mechanisms for fragmentation during the polymerization reaction were simulated and shown in the work of Alizadeh *et al.*, namely the layer-by-layer and the sectioning fragmentation mechanism. Both these mechanisms are shown in Figure 1.10. The first mechanism (shown on top in the figure), is generally assumed in the case of spatially homogeneous catalysts, *i.e.* no preferential path for the diffusion of the monomer. In that case, the monomer first polymerizes at the surface of the catalyst particles. This layer fragments and by doing so it enables diffusion into the second layer, where the same process occurs. This continues all the way into the center of the catalyst particles. The second mechanism of particle fragmentation during the polymerization reaction is the sectioning mechanism. In this mechanism, there should be a distribution in the pore sizes of the particles. In Figure 1.10, there are larger pores that penetrate all the way into the center of the particle. If that is the case, then the active sites that are located in such a large pore will polymerize first and thus fragment first, creating smaller domains of fragmented catalyst [33]. When translating to the catalyst system reported in this thesis, it is believed that the 'sectioning' fragmentation mechanism can be applied best. This is due to the pore system that is present in the catalyst particles that are studied in this thesis.

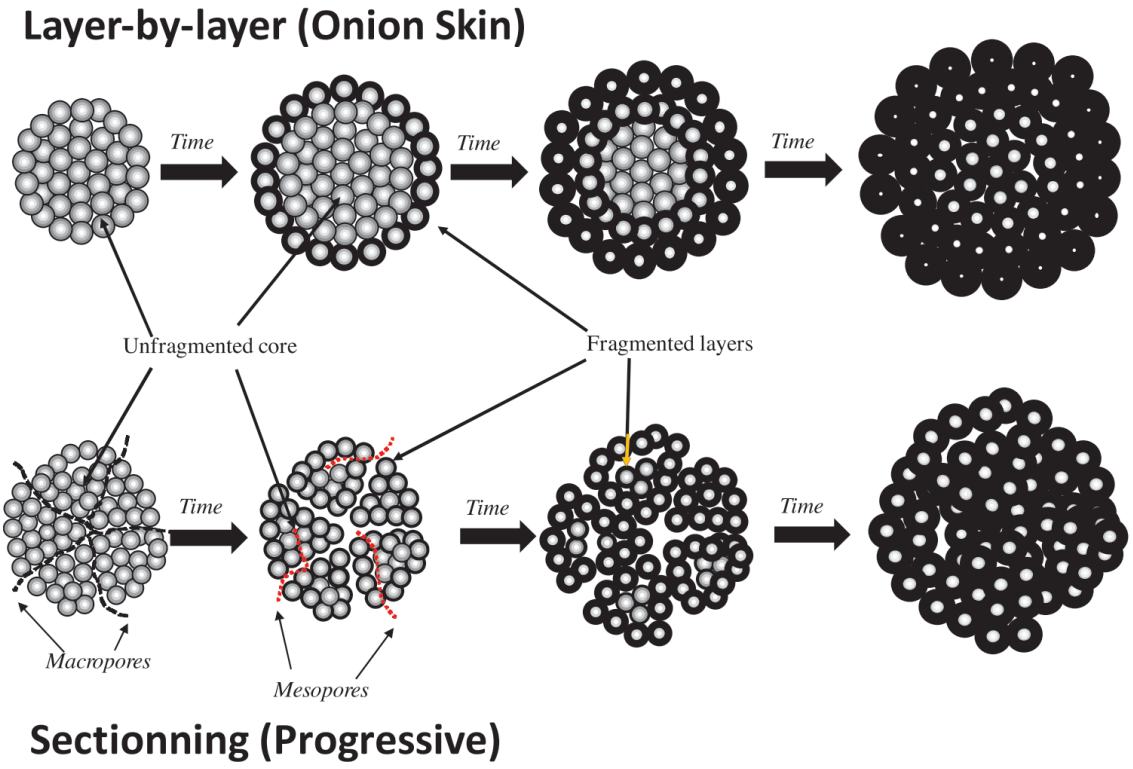

Figure 1.10: Main mechanism for fragmentation during catalyzed polymerization reactions. The top mechanism shows the layer-by-layer representation of fragmentation. This mechanism states that fragmentation begins at the outer layer and progresses toward the center of the particle. The mechanism on the bottom is called sectioning, where the fragmentation occurs first on the largest pores and subsequently on the smaller pores. Figure obtained from the paper of Alizadeh *et al.* [33].

Research goal

As mentioned in the introduction, the addition of titanium to the silica-supported metallocenes leads to a significant increase in olefin polymerization activity. Since the theoretical foundation for this promotor effect is still unknown, the aim of this research is to study the reason(s) for the increase in polymerization activity. The acidity, activity and fragmentation of the metallocene catalysts are studied to clarify the role of titanium, which could be threefold: either an increase in acidity, number of active sites and/or an easier fragmentation after addition of titanium. To investigate these parameters, multiple characterization techniques are used during this thesis. Fourier Transform Infrared Spectroscopy (FTIR) with pyridine as probe molecule is used to study the Lewis acidity of the catalyst samples. A polymerization reaction is performed with an internal standard and the method of standard addition, to study the number of active sites. Finally, the fragmentation of the catalyst particles is studied with both Diffuse Reflectance Infrared Fourier Transform Spectroscopy (DRIFTS) and Confocal Fluorescence Microscopy (CFM). DRIFTS is used to perform a kinetic study on the catalyst samples during ethylene polymerization. Next to that, CFM is used to visualize the fragmentation after polymerization. For the use of this technique, the catalysts must be fluorescent. However, since the catalyst samples are not autofluorescent, they are first stained with an 'inert' dye (*i.e.* not active for polymerization and not deactivating towards the catalyst). Ultimately, the goal is to gain a better understanding of the role of titanium as activity booster in the polymerization process of polyethylene with supported metallocenes.

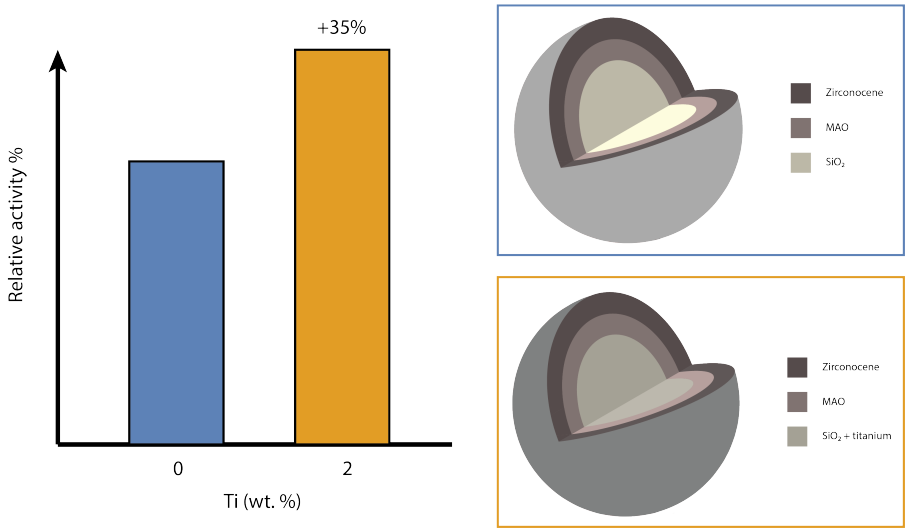

Figure 2.11: Schematic overview of the influence of the addition of titanium on the polymerization activity, when added to the silica support of a metallocene catalyst.

Methodology

Fourier Transform Infrared Spectroscopy

Theoretical background

Being the most common form of vibrational spectroscopy, infrared spectroscopy handles the infrared region of the electromagnetic spectrum. This region, ranging from 0.7 μm (14000 cm^{-1}) to 1000 μm (10 cm^{-1}) can be divided into three regions of interest. The near-IR region, which is in the range of 14000-4000 cm^{-1} can be used to excite harmonic vibrations. Next to that, the far-IR region, ranging from 400-10 cm^{-1} can be used for rotational spectroscopy. Finally, the region that is of interest for this thesis is the mid-IR region (4000-400 cm^{-1}), which can be used to study fundamental vibrations.

Different techniques (*e.g.* transmission, diffuse reflectance) originate from the principle of infrared spectroscopy, which makes use of the fact that the molecules of interest can absorb electromagnetic radiation of an energy that matches the transition energy of the bond or group that vibrates. These energies are determined by various properties of the molecules, such as the mass of the individual atoms and the strength of the bonds.

Molecules can vibrate in different ways, referred to as the vibrational modes. The number of different vibrational modes a molecule can exhibit are based on the following principle: a molecule consisting of N atoms has $3N$ degrees of freedom. These degrees of freedoms are consisting of three translational degrees of freedom and three rotations of the molecule along the three principal axes of inertia. Linear molecules have only two rotational degrees of freedom, as no energy change is involved in the rotation along the main axis. This results in a number of fundamental vibrations that is $3N$-6 for a non-linear and $3N$-5 for a linear molecule [37]. Figure 3.12 shows the different vibrations of both linear and non-linear molecules. These vibrations can be divided into four different types of vibration:

- Stretching vibrations (ν): vibrations that are changing the length of the bond
- Bending vibrations in one plane (δ): vibrations that are changing the bond angle, but not the bond length
- Bending vibrations out-of-plane (γ): vibrations that are observed when one atom oscillates through a plane. This plane has to consist of at least three neighboring atoms.
- Torsion vibrations (τ): vibrations that change the angle between two planes that go through atoms.

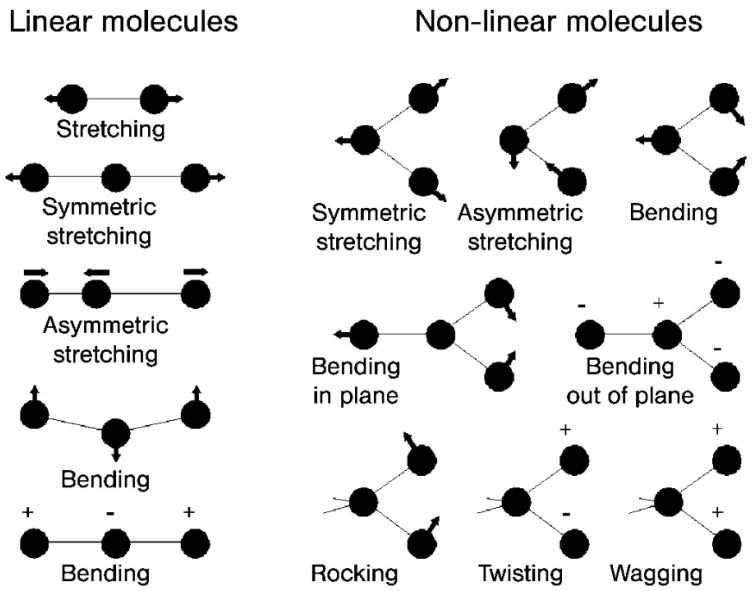

Figure 3.12: Fundamental vibrations of several molecules. Figure obtained from the book of J. Niemantsverdriet. [37]

Important to note is that the absorption of an infrared photon only occurs when the dipole moment changes sufficiently during the vibration, which results in the exclusion of certain vibrations. The intensity of the infrared band observed in the spectrum is proportional to the change in dipole moment.

In transmission IR (used in for example pyridine FTIR spectroscopy), the infrared signal is detected after it has transmitted through the sample. The sample is pressed into a self-supporting pellet of approx. 0.38 cm^2 and with roughly a millimeter in thickness. When the infrared radiation is transmitted through the pellet a molecular fingerprint is made, which provides information about the composition of the material, *i.e.* what kind of bonds are present in the material.

FTIR with pyridine

To study the acidity of the metallocene catalyst on the support, FTIR spectroscopy with pyridine as probe molecule is used. With this technique, it is possible to probe both Lewis and Brønsted acid sites, due to the lone pair on the nitrogen of the pyridine. Pyridine is able to determine the nature, strength and number of acid sites [38]. The lone pair coordinates on the Lewis acid site, while it forms a neutral complex (weak acidity) or an ionic complex (strong acidity) with a Brønsted acid site. In the case of the SiO_2-supports, the surface exhibits isolated silanols. Pyridine will form an hydrogen bond with these silanol groups, but since peaks at 1540 and 1640 cm^{-1} are absent, Brønsted acid sites are not present [39]. The main source of acidity is originating from the MAO, which results in a change of the surface from silanols to charged alumina species. The pyridine can coordinate to these alumina species, indicating Lewis acidity. This acidity is a measure of the activation efficiency of MAO. The coordination and complex formation of pyridine with acid sites is shown in Figure 3.13.

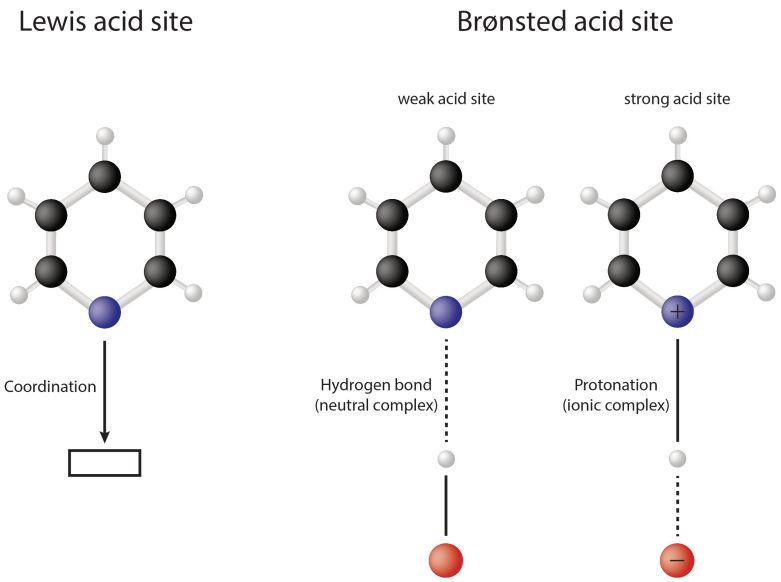

Figure 3.13: Schematic overview of the different types of acidity a pyridine molecule can probe.

The ring vibration bands of pyridine, in the region of 1400-1650 cm^{-1}, are the main vibrations sensitive to the adsorption. The different ring vibrations that indicate Lewis acidity are shown in Figure 3.14. Each vibration has a specific wavenumber at which it is visible in the FTIR spectrum. When the pyridine is adsorbed onto for example a silica support, this wavenumber changes. Table 3.1 shows the vibrations of pure pyridine, compared to when interacting with the two surface species that are expected to be found on SiO_2-supported metallocene catalysts.

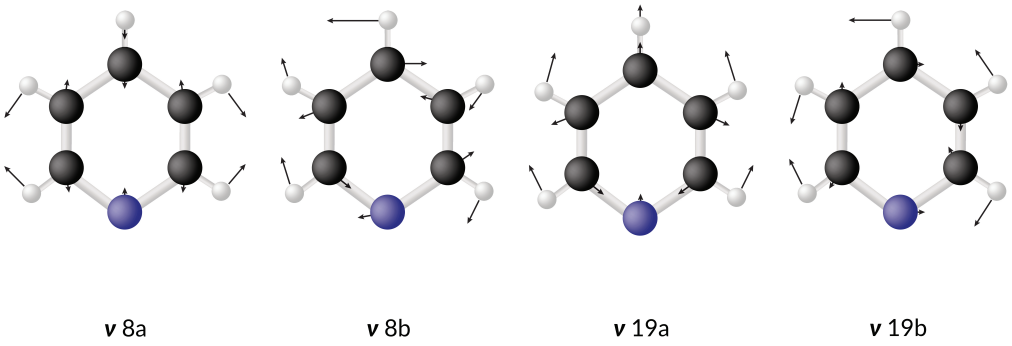

Figure 3.14: Schematic overview of the ring vibrations of the pyridine molecule.

Table 3.1: Overview of the ring vibrations of pyridine, where the attribution refers to the vibrations shown in Figure 3.14. The vibrations highlighted in red are the most useful to determine the character of the acid sites.

Vibration	Pyridine (cm^{-1})	H-bond on silica (cm^{-1})	Coordinated on alumina (cm^{-1})
ν 8a	1579	1595 (+16)	1600-1626 (+21-47)
ν 8b	1572	1577 (+5)	1577 (+5)
ν 19a	1478	1487 (+9)	1493 (+15)
ν 19b	1439	1445 (+6)	1445-1455 (+6-16)

A FTIR spectrum of SiO_2 is shown in Figure 3.15, where the different vibrations are visualized at each wavenumber. As can be seen, the vibrations 8a and 19b are most intense and can therefore be used to determine the acid strength of the material. Vibration 8a (1595 cm^{-1}) can be used to distinct between the different coordination sites, while vibration 19b (1445 cm^{-1}) can be used to quantify the amount of acid sites. As proposed by Panchenko *et al.* [40], equation 3.1 can be used to determine the concentration of Lewis acid sites.

$$C_{LAS} = \frac{A * 10^3}{A_0 * \rho} \tag{3.1}$$

The concentration of Lewis acid sites (C_{LAS}) can be calculated by using the apparent integral adsorption under the curve delimited by dδ (cm^{-1}), which is represented by A (cm^{-1}). The area is determined for the spectrum at 200°C, to ensure removal of physisorbed pyridine. The apparent integral adsorption coefficient, A_0 (cm μmol^{-1}), is given as 2.22 for pyridine at 1453 cm^{-1}. The mass of the wafer (mg) per cm^2 through which the beam is sent is represented by ρ.

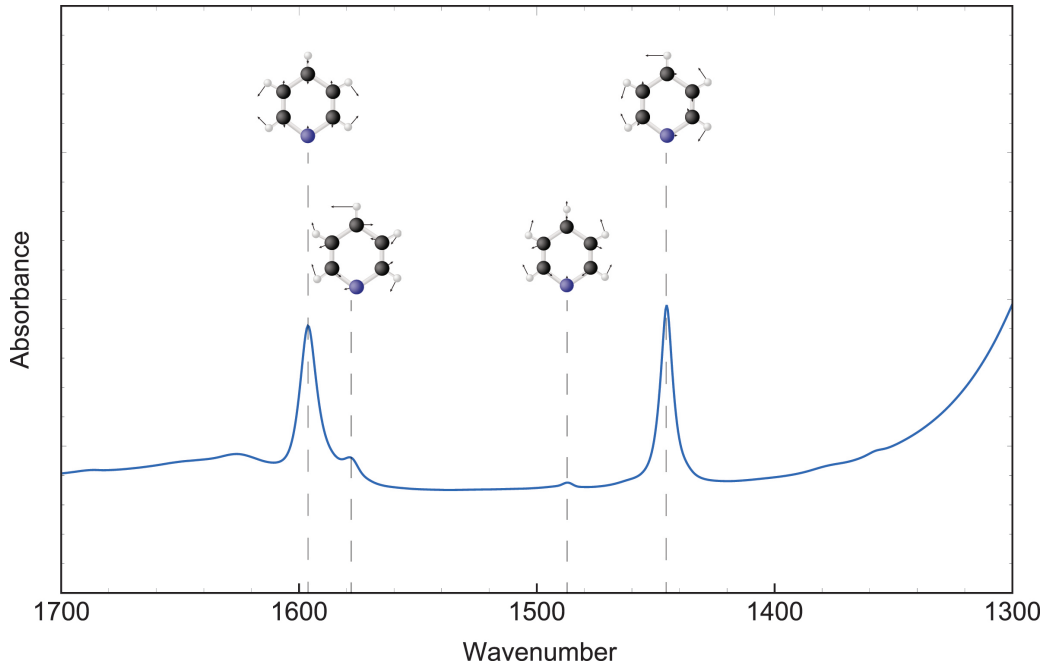

Figure 3.15: FTIR spectrum of SiO_2 with pyridine as probe molecule. The pyridine was allowed to adsorb on the surface for 30 minutes. The vibrations are visualized for each peak.

Diffuse Reflectance Infrared FT Spectroscopy

Diffuse Reflectance Infrared Fourier Transform Spectroscopy (DRIFTS) is a spectroscopic technique that is used to study powder samples. In this technique, the incident infrared light is reflected in different amounts and with different angles, depending on the bulk properties of the material. Therefore characteristics of the material can be studied [41]. As can be seen in Figure 3.16, there are different kinds of reflections from the incident infrared beam. Specular reflection is obtained when the infrared beam reflects directly from the surface of the sample. Next to that, there is also reflection between the particles, where the beam isn't penetrating the particles themselves. This type of reflection can have any angle relative to the incident beam, but since it does not penetrate the particles, it does not contain any information about the sample itself. This type of reflection is called diffuse specular reflection. True diffusion reflection is the type of reflection that contains information about the sample, since the incident beam penetrates one or multiple particles [42]. This reflection can also have any angle relative to the incident beam, but since this beam has traveled through the particles, it gives information about the absorption properties of the material. These properties give diffuse radiation similar information when compared to transmission radiation.

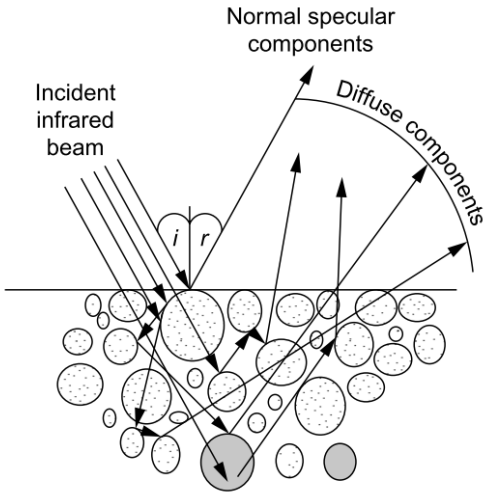

Figure 3.16: Schematic overview of the mechanism of reflection in a powder sample. Figure obtained from Armaroli *et al.* [42].

However, these different types of reflections can't be optically separated and therefore it is important that the specular diffuse reflection component (no penetration into the particle) is weak. In that case, the spectra are relatively similar to transmission spectra. Several parameters are important for the quality of the spectra, such as the refractive index of the sample, the packing density, homogeneity, absorption coefficients and concentration.

The main advantages in using this technique are the easy sample preparation and the ability to measure non-transparent samples, which is not possible when using FTIR spectroscopy. Next to that, the reaction can be monitored *in situ*, which enables the study of the sample behaviour during for example a polymerization reaction. It is possible to use a pellet in this technique as well, if the reaction would be from gas phase to gas phase. Since polymerization is a reaction from gas phase to solid phase, this would compromise the pelllet. The DRIFTS setup with a praying mantis reaction chamber used for these experiments can withstand elevated temperatures, so the reaction conditions can be tuned to do a multi-parameter study (both temperature and flow of ethylene) on the catalyst samples.

In the scope of this thesis, DRIFTS is used to study the catalyst during the polymerization of ethylene gas. Based on the aforementioned characterics that can be obtained from this method, a kinetic study on the catalyst samples can be performed. Figure 3.17 shows the result of a polymerization reaction versus time. The formation of poly-ethylene is indicated by the appearance of sharp and intense peaks at 2926 cm^{-1} and 2855 cm^{-1}, which can be assigned to the asymmetric and symmetric CH_2 stretching vibration, respectively. The peaks at 1366 cm^{-1} and 1351 cm^{-1} can be assigned to bending deformation and at 731-720 cm^{-1} from rocking deformation. The results from the DRIFTS can be used to visualize the three stages of polymerization. In the initial stage (the red spectra), the ethylene diffuses through the catalyst pores. The externally exposed active sites of the catalyst become covered by a thin layer of polyethylene. In the second stage, the initially formed thin layer of polymer grows in thickness, which causes an increase of the particle size (green spectra). In the final stage of the polymerization (blue spectra), the polymer grows inside the pores of the catalyst, causing fragmentation of the catalyst particle. In this final stage, the catalyst bed also increases in height, causing an upward shift in the baseline and eventually saturation of the detector. To study the fragmentation of the catalyst samples, the band at 2855 cm^{-1} (marked with the * in Figure 3.17) is followed over time.

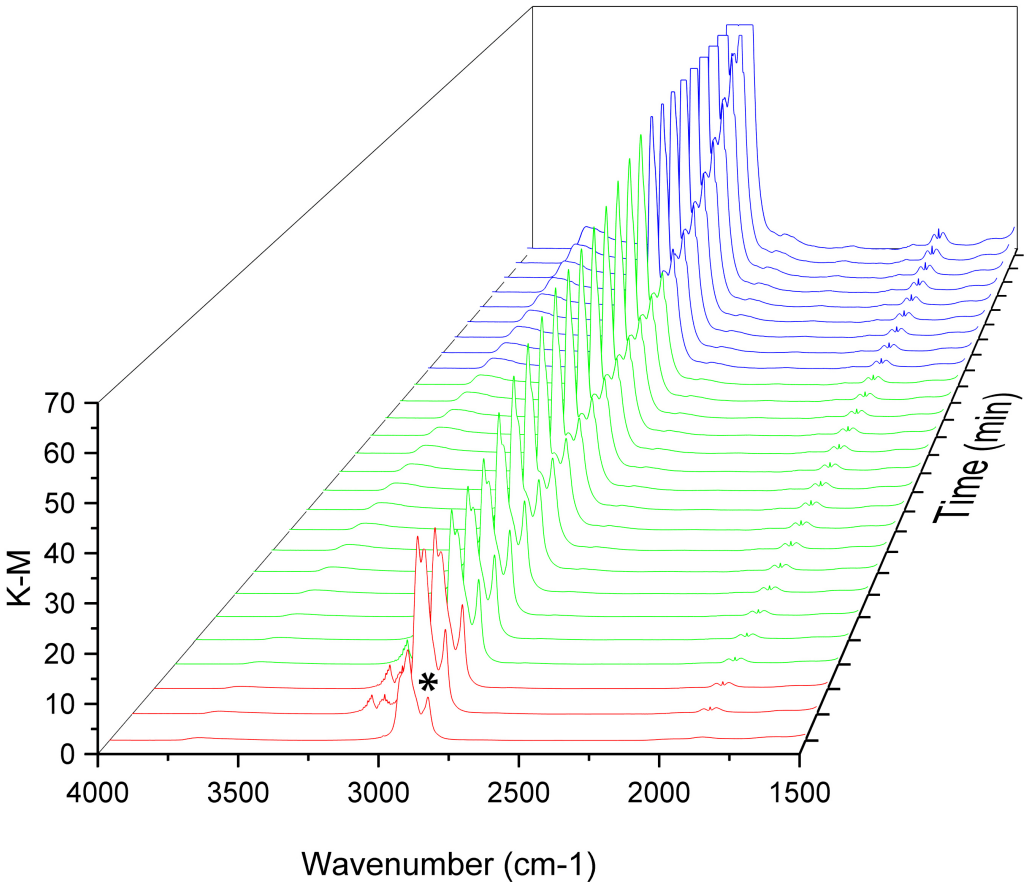

Figure 3.17: Evolution of the DRIFTS spectra over time while flowing ethylene over the catalyst bed. The asymmetric CH_2 stretching vibration appears at 2926 cm^{-1} and the symmetric CH_2 stretching vibration at 2855 cm^{-1}, indicated with the *.

Polymerization testing

To study the number of active sites in the samples, polymerization testing with deuterium labeling is used. For this test, 1-hexene is polymerized by the catalyst of choice using toluene as solvent, an internal standard (diphenylmethane) and an impurity scavenger (triisobutylaluminum, TiBAl). Using only 1-hexene as monomer, the reaction will mainly lead to the formation of dimers and trimers, as shown in the work of Harvey *et al* [43]. By quenching the reaction with deutared methanol, this will lead to an oligomer with a deuterium atom instead of a proton at its first carbon atom. The scheme for this quenching reaction is shown in Figure 3.18.

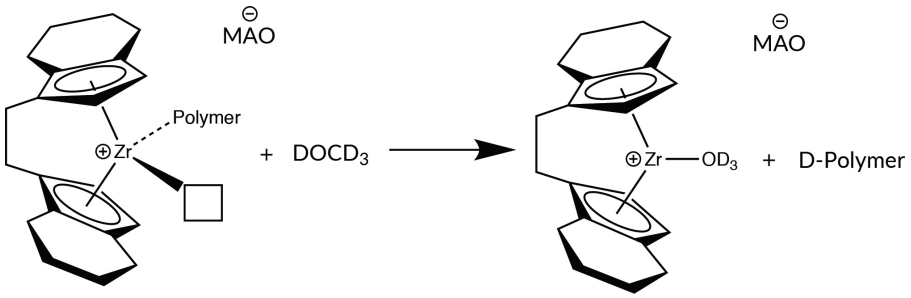

Figure 3.18: Reaction scheme for the quenching of the polymerization process with methanol-*d*.

By using NMR, both ^{1}H-NMR and ^{2}H-NMR, one can study the decrease in amount of the monomer (^{1}H-NMR) and count the number of active sites that have polymerized the 1-hexene during the reaction (^{2}H-NMR). As shown in a paper from Gunasekara, the ^{1}H-NMR can also be used to study the amount of vinylenes and vinyledenes formed [44]. This can be seen in Figure 3.19, where the various peaks are visualized with the ^{1}H nuclei they are assigned to.

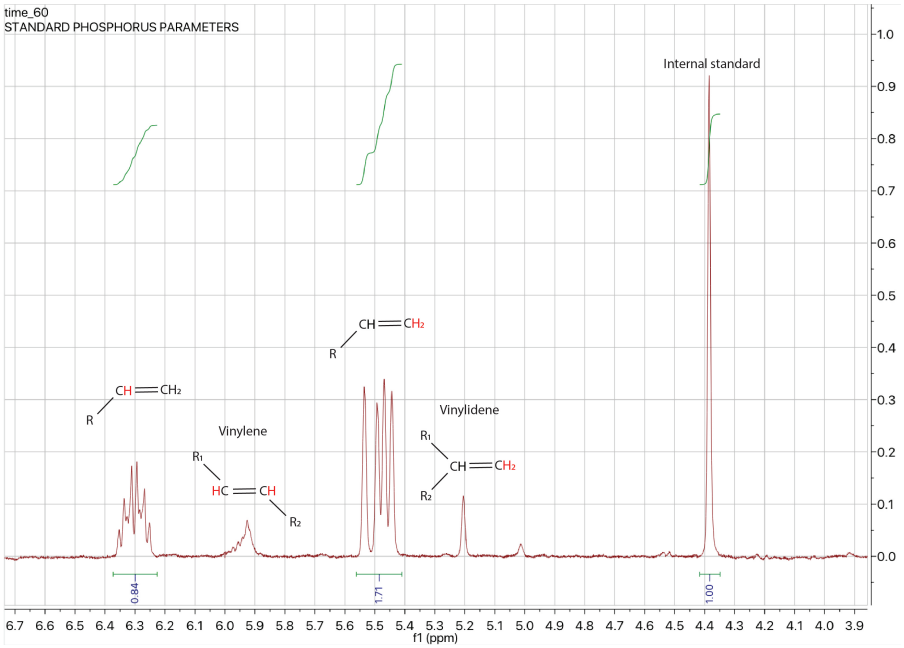

Figure 3.19: ^{1}H-NMR spectrum for the polymerization testing reaction with 1-hexene (55% conversion). This spectrum is the result of 1 hour at 85°C with 1-hexene as monomer and shows the various peaks of importance.

As can be seen from the reaction mechanism in Figure 1.5 on page 15, the vinylidene (5.2 ppm) product is the desired product, while the vinylene (6.0 ppm) product is obtained via misinsertion (2,1-insertion). The peaks at 5.5 and 6.3 ppm correspond to the 1-hexene monomer, while the peak at 4.4 ppm corresponds to the internal standard diphenylmethane. By studying the decrease of the 1-hexene peaks relative to the internal standard, the conversion for the reaction can be determined.

As mentioned before, ^{2}H-NMR is used to study the number of active sites. This was done by the method of standard additions. To perform these calculations, the ^{2}H-NMR peaks first need to be assigned, as shown in Figure 3.20. Toluene was present as solvent (the toluene peak in the ^{2}H-NMR spectrum is due to the natural abundance of deuterium in proteo-toluene) for the deuterated polymers, dichloromethane was added as internal standard.

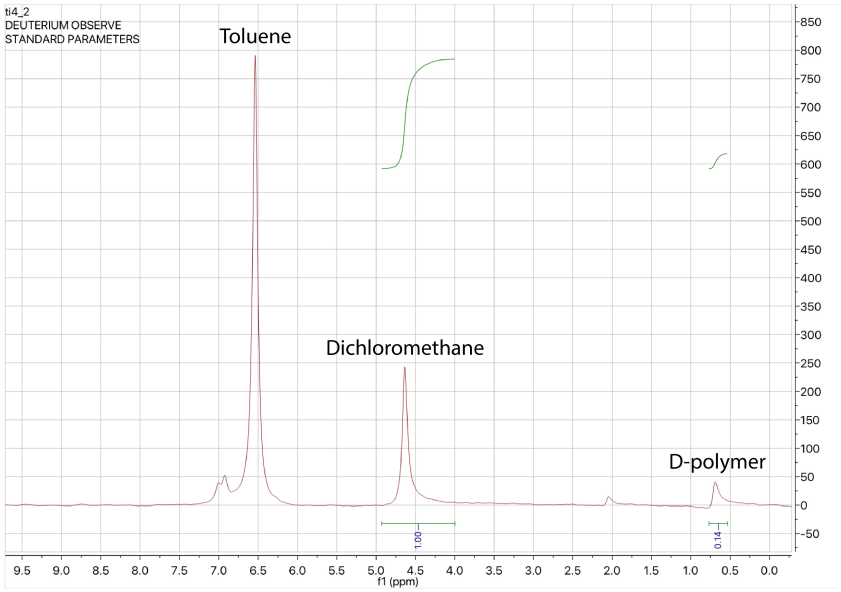

Figure 3.20: ^{2}H-NMR spectrum for the polymerization testing reaction after two additions of deuterated dichloromethane, with the peaks assigned to the several components of the mixture that was studied.

By using the formulas described in the book of D. Harvey, the analyte concentration can be determined [45]. With the method of standard additions, the complication of matching the matrix of the standards and the matrix of the sample can be avoided. The idea is that a spike of the external standard is added directly to the sample, without any further adjust in the volume (as can be seen in Figure 3.21).

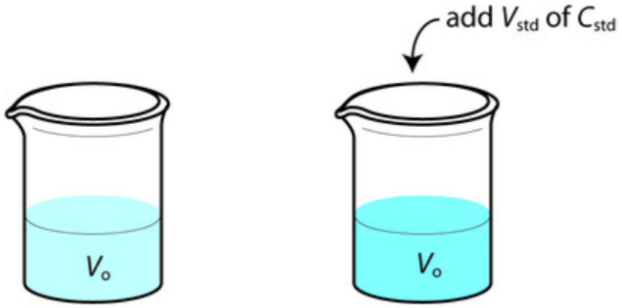

Figure 3.21: Schematic illustration showing the method of standard additions. In this case a spike of the external standard is added directly to the sample without any further adjust in the volume. Figure obtained from the book of D. Harvey. [45]

To standardize an analytical method, equation 3.2 can be applied. S_{samp} is the signal before the addition of an external standard (in this case proteo-dichloromethane), which equals to the multiplication of sensitivity (k_A) and the concentration of the analyte (C_A).

$$S_{samp} = k_A * C_A \tag{3.2}$$

Two different methods can be used to calculate this C_A (the concentration of deuterium in DCM) based on the amount of data points that are present. First of all, it can be calculated by adding a known volume of external standard (deuterated dichloromethane), which results in equation 3.3. This method uses only two data points and is therefore less reliable.

$$S_{spike} = k_A(C_A * \frac{V_0}{V_0 + V_{std}} + C_{std} * \frac{V_{std}}{V_0 + V_{std}}) \tag{3.3}$$

Equation 3.3 shows several variables, with S_{spike} as the signal after addition of the known volume of the external standard (V_{std} of C_{std}). This external standard, deuterated dichloromethane, makes it able to resolve the amount of deuterium present in proteo-dichloromethane. By combining equations 3.2 and 3.3, equation 3.4 forms.

$$\frac{S_{samp}}{C_A} = \frac{S_{spike}}{C_A * \frac{V_0}{V_0+V_{std}} + C_{std} * \frac{V_{std}}{V_0+V_{std}}} \tag{3.4}$$

The final step is to rewrite equation 3.4 into the form $C_A = ...$, since that is the parameter of interest. This operation is shown in equation 3.5, which is used to calculate the concentration of deuterium in dichloromethane.

$$C_A = \frac{S_{samp} * \frac{V_{std}}{V_0+V_{std}} * C_{std}}{S_{spike} - (S_{samp} * \frac{V_0}{V_0+V_{std}})} \tag{3.5}$$

By calculating the concentration of deuterium in proteo-dichloromethane (peak at 5.3 ppm in the V_0 spectra), the concentration of deuterium containing polymers can be calculated. Knowing the amount of deuterium containing polymers gives an indication of the amount of active sites, since each active site should result in the formation of a deuterated polymer. Figure 3.22 shows the method used to calculate C_A in a different way. Since this method takes multiple data points into account versus the two in the case of using the previously mentioned equations, this method is favored and used to calculate the amount of active sites in the catalyst samples.

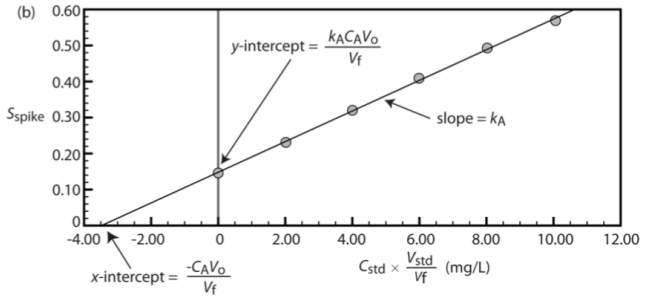

Figure 3.22: Graph of the standard additions calibrations curve, used to calculate the concentration of deuterium containing polymers. Figure obtained from the book of D. Harvey. [45]

Confocal Fluorescence Microscopy

To visualize the fragmentation of the catalyst during a polymerization reaction, Confocal Fluorescence Microscopy (CFM) can be used. In this method, the catalyst is stained with a dye to make the catalyst fluorescent. By combining laser excitation, confocal microscopy and photo-diode detection, CFM enables the study of single particles [46]. The technique uses a spatial pinhole that blocks out-of-focus light when forming an image [47]. When comparing to a conventional microscope, where the light travels as far into the sample as it can penetrate, CFM focuses a smaller beam of light at one narrow depth level at a time, resulting in enhanced resolution. By combining two-dimensional images at different depth levels, a three-dimensional reconstruction of the sample can be made. Figure 3.23 shows a schematic overview of such a CFM, with the different elements of the microscope highlighted. First of all, the laser, which is used to excite the sample to an energetically higher state (explained on the next page). The laser choice is based on the absorption spectrum of the dye that is used to stain the sample. As a rule of thumb, fluorescence appears at around 20-30 nm higher in wavelength than absorption. The beam splitter is used to filter the excitation from the emitted light in the fluorescence beam path of the microscope. The scanner makes sure that the laser beam can be guided across the sample in the xy-plane. The objective lens is the most important piece of the microscope, because it (mainly) determines the optical image formation and resolution of the system. Next to that, the Z Control is used to control the depth level of the studied sample and enables three-dimensional reconstruction. The pinhole blocks, as mentioned before, the out-of-focus light, thereby providing optical sectioning capacity. It defines the optical slice thickness, making sure that the resolution of the acquired image is optimal. The pinhole can be set via computer software and is ideally around 1 Airy unit (due to the diffraction pattern of light). Finally, the photomultiplier tube is used to convert the light signal (photons) into an electrical signal (electrons), based on the photoelectric effect. This electrical signal is processed by the computer and results in an image.

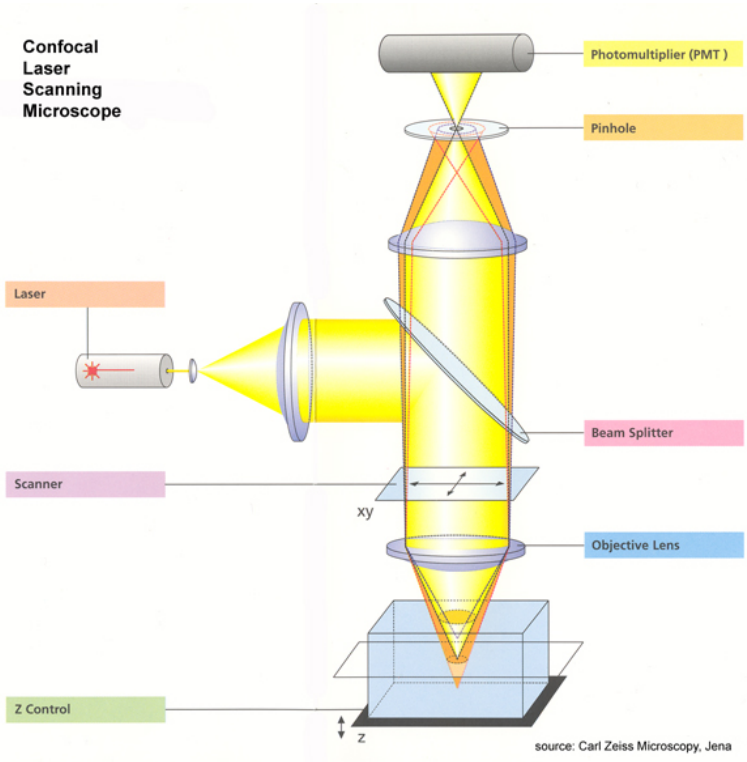

Figure 3.23: Schematic overview of a Confocal Laser Scanning Microscope. Figure obtained from Carl Zeiss Microscopy company in Jena, Germany.

The principle of fluorescence

Luminescence is defined as the emission of light, occuring from electronically excited states. This luminescence is divided into two categories, namely phosphorescence and fluorescence. Phosphorescence is the phenomena that occurs with for example "glow-in-the-dark" toys, where the sample is first illuminated (which excites the material) and due to the slow emission rates, it has lifetimes in the order or milliseconds to seconds. Fluorescence, which has much shorter lifetimes, is typically present in the case of polycyclic, aromatic molecules. Figure 3.24 (left) shows a typical Jablonski diagram of such an aromatic molecule. To observe fluorescence, a molecule first needs to be excited from the ground state to an energetically higher state (blue arrow). Via non-radiative pathways (shown with the red arrows) the system relaxes back to the lowest level of the excited state, since that is thermodynamically most favorable. The relaxation back to the ground state typically occurs to a higher excited vibrational ground state level (green arrow). Since the energy of the light needed for the absorption is larger than the energy of light observed due to this relaxation, a Stokes shift is present. This reveals that the fluorescence occurs at longer wavelengths than absorption, typically around 30 cm^{-1} longer [48].

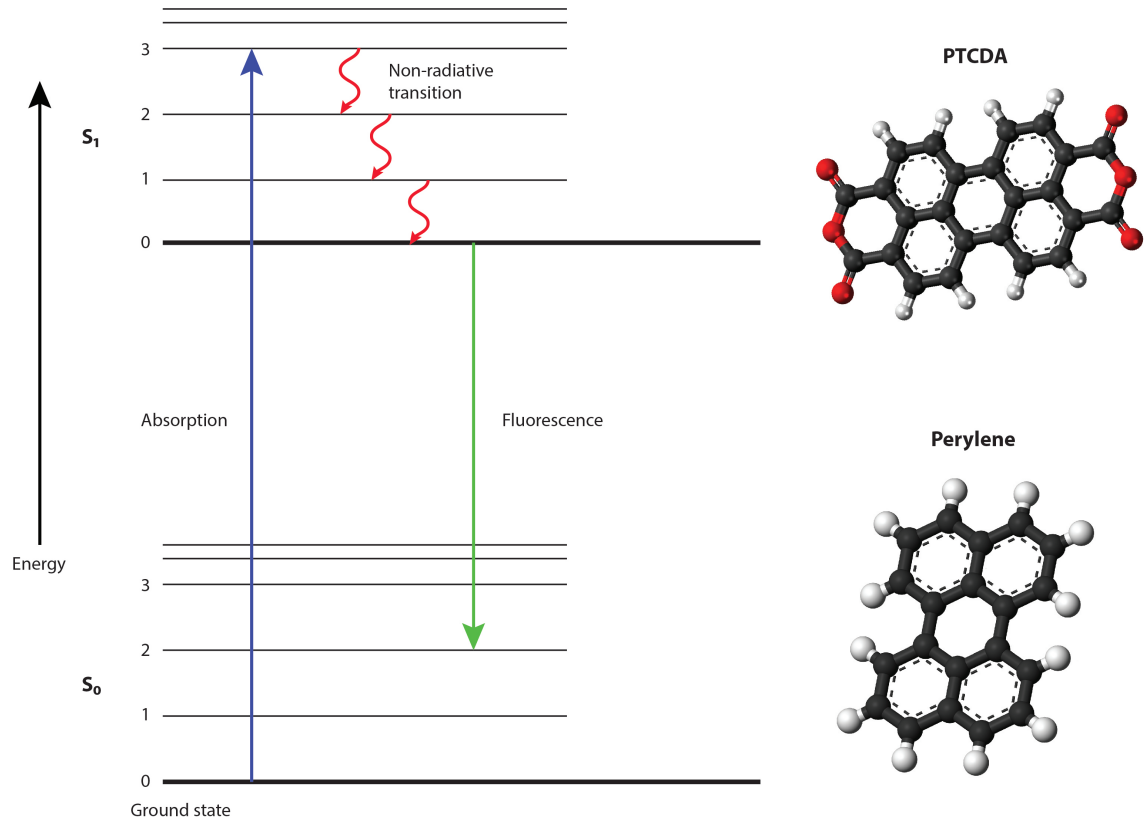

Figure 3.24: Illustration used to explain fluorescence, left shows a typical Jablonski diagram, while right shows the two aromatic molecules used to make the catalyst fluorescent.

The right side of Figure 3.24 shows the two dyes used to stain the catalyst samples. These dyes were selected since they are not active towards polymerization, which is the case when using for example a styrene-based dye. PTCDA, or perylene-3,4,9,10-tetracarboxylic dianhydride, is a red solid with absorption maxima at 480 nm and 552 nm [49]. PTCDA is excited with the 561 nm laser and shows red fluorescence. On the other hand, perylene is a yellow solid with absorption maxima at 409 and 435 nm, and is therefore excited with the 405 nm laser, which results in blue fluorescence. Both dyes consist of the perylene base structure, but PTCDA has multiple oxygen groups to enhance the coordination towards the catalyst, which should result in a more efficient staining.

Experimental

Chemicals

The following chemicals were used: pyridine, diphenylmethane, 1-hexene, triisobutylaluminum (1.0M in hexanes, TiBAl), dichloro[rac-ethylenebis (4,5,6,7-tetrahydro-1-indenyl)]zirconium(IV), dichloromethane (both in the proteo and deuterated form), and perylene-3,4,9,10-tetracarboxylic dianhydride (PTCDA) were obtained from Sigma Aldrich. Toluene, n-pentane, methanol-*d* and perylene were obtained from Fisher Chemicals. Silica and methylaluminoxane (30 wt% in toluene, MAO) were obtained from Total. The solvents used during this thesis were degassed, dried with molecular sieves and stored in the glovebox.

Synthesis of the catalyst

All the syntheses were performed in Schlenk-type flasks or in a N_2 glovebox. All supports, MAO impregnated supports and catalyst materials were synthesized at Total.

SiO_2/MAO/Zr: The silica was first dried at 120°C for 1 h, and afterwards dehydroxylated at 450°C for 4h (under N_2). The dehydroxylated silica was mixed with a solution of MAO in toluene for 4h under reflux and inert atmosphere, with the target loading of 14.5 wt% Al. The catalysts were synthesized by mixing the support/MAO samples in a metallocene solution in toluene for 2h at room temperature, to reach the desired loading of 2 wt% metallocene. After impregnation, the catalyst was filtered and rinsed with dry toluene and pentane and dried (under vacuum) afterwards to remove solvent traces.

Ti-SiO_2/MAO/Zr: The Ti-doped silica support with a target Ti loading of 2 wt% was performed by impregnating a solution of titanium isopropoxide to the dry silica at room temperature or 270°C (page 33 will explain the difference). The doped supports were then dehydroxylated at 450°C for 4h (under N_2). The MAO anchoring and metallocene impregnation procedures were the same as for the SiO_2/MAO/Zr samples.

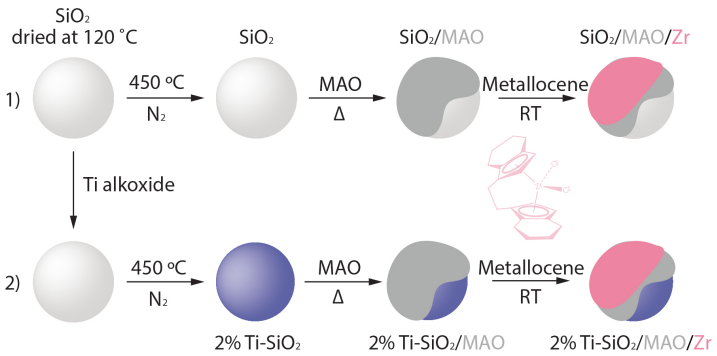

Figure 4.25: Schematic overview of the synthesis route used to obtain the samples used for the characterization.

Sample labeling

The samples that were received from Total were labeled in different ways: either '*NT 2%Ti on* SiO_2' or '*x%Ti -* SiO_2' (with x being 0, 2, 4, 6 and 8). In the case of the NT samples (where NT stands for New Technology), the Ti-content is distributed homogeneously throughout the catalyst particle. In the case of the samples that are labeled in the '*x%Ti-*SiO_2' style, the Ti-content was more present at the edges of the catalyst particles than on the inside, as can be seen in Figure 4.26. There should be no difference in polymerization activity between the two methods of synthesizing the catalysts.

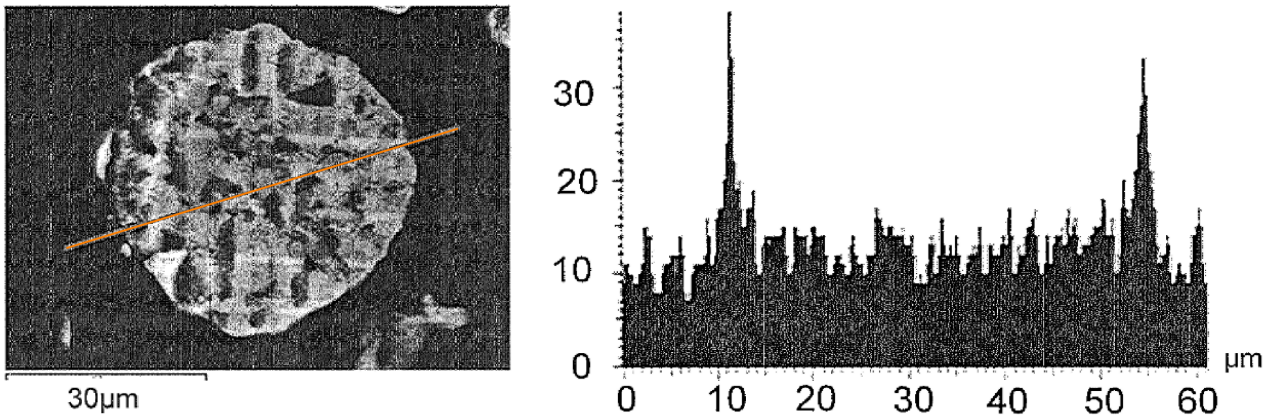

(a) **(b)**

Figure 4.26: Titanium content of a catalyst particle according to the patent published by Total [6]. Image (a) shows the catalyst particle with a diagonal line that is used to indicate where the titanium content was measured. The results from this measurement can be seen in graph (b), which indicates a higher Ti-content at the edges than on the inside of the particle.

Synthesis differences

Different synthesis were performed to obtain the difference in titanium distribution as mentioned on top of this page. As mentioned on page 32, two different temperature points were used to add the titanium isopropoxide. These different temperatures of titanium isopropoxide addition (marked with the red cross) result in either the homogeneous titanium distribution (Figure 4.27a), while the b) part of that figure shows the calcination ramp used to synthesize a higher loading of titanium at the surface.

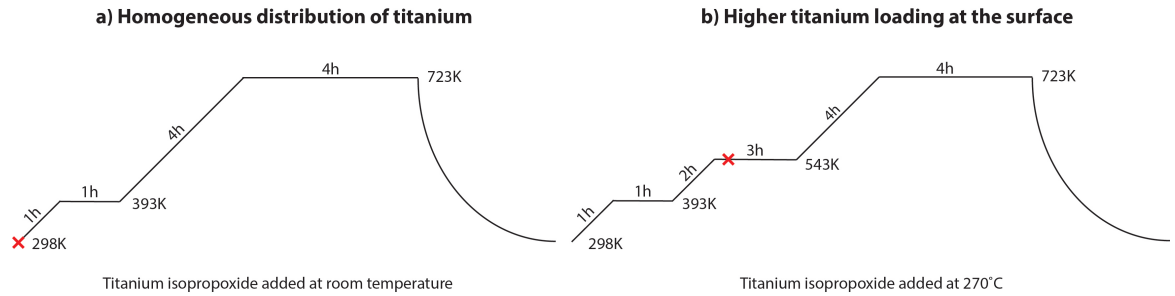

Figure 4.27: Calcination settings used to obtain either a homogeneous distribution of titanium versus a localized (at the surface) distribution of titanium, where the red cross shows the temperature of titanium isopropoxide addition.

FTIR spectroscopy with pyridine as probe molecule

FTIR spectroscopy was used to study the influence of titanium on the acidity of the samples. The spectra were recorded in transmission mode on a Thermo Scientific iS5 instrument with a DTGS detector using 32 scans per spectrum and a resolution of 4 cm^{-1}. The self-supported wafer was placed in a well-sealed cell that allowed switching between vacuum and the probe molecule. All the wafers were prepared in a N_2 glovebox with a hand-press (PIKE Technologies). These wafers (6.5-10.5 mg/7 mm diameter) were held in position by a stainless steel collar. No treatment to remove water/CO_2 was required, since the samples were prepared and stored in an inert atmosphere. For the pyridine FTIR measurements, pyridine adsorption was allowed for 30 minutes (until equilibrium), with spectra taken every 5 minutes. Vacuum desorption (for 45 minutes) and temperature programmed desorption (TPD) under vacuum (5°C/min ramp to 550°C) were performed afterwards, taking spectra every 25°C. The acidity was quantified with the spectra at 200°C to ensure the removal of physisorbed pyridine.

Polymerization testing

General procedures

All experiments were performed under air- and moisture-free conditions using a circulating nitrogen-filled glovebox operating at <1.5 ppm oxygen or under argon using standard Schlenk line techniques. ^{1}H NMR characterization experiments were performed on a MRF400 spectrometer. ^{2}H NMR (400 MHz) spectra were recorded on a VNMRS400 spectrometer and referenced to the chemical shift of dichloromethane (5.3 ppm). All chemicals needed for the polymerization (1-hexene, TiBAl, diphenylmethane, toluene and the catalyst samples) were stored inside the glovebox. Methanol-D (CH_3OD) was obtained from Acros Organics and used as received.

Analysis by NMR measurements

^{1}H NMR spectra of poly-1-hexene were obtained in $CDCl_3$ solution at room temperature on a MRF400. The spectra were recorded at 400 MHz using 16 scans.

Synthesis of ^{2}H-labeled poly-1-hexene

For a typical oligomerization, in a glovebox, a solution of catalyst (0.050 gram, $2.56*10^{-6}$ mol metallocene) and TiBA (2.4 ml, 0.0024 mol) were added into a 10 mL volumetric flask and diluted to the mark with toluene. The flask was rinsed with 10 mL toluene to ensure quantitative transfer of the catalyst. Diphenylmethane (0.2156 gram, 0.0005 mol, [monomer]/[internal standard] = 5) and 1-hexene (0.5393 gram, 0.0026 mol, [monomer]/[catalyst] = 1000) were added into a 5 mL volumetric flask and diluted to the mark with toluene. A 2 mL portion was transferred to a syringe and sealed with a screw-cap septum. The syringe and septum were placed in a resealable plastic bag. The remaining internal standard/monomer solution was used to determine the initial concentration of the monomer relative to the internal standard. The reaction was started by injecting the 2 ml of internal standard/monomer solution. The temperature was held constant at 85°C with a silicone oil bath. The reaction was quenched after 1 hour by the injection of 2 ml CH_3OD. The solution was checked for monomer consumption and end-group ratio by ^{1}H NMR.

Active site concentration analysis

The reaction mixtures were filtered through a silica column to remove the quenched catalyst. The reaction sample was dried to remove some of the excess solvent and diluted in a 2 mL volumetric flask with toluene. Complete drying was not attempted as it leads to loss to some of the dimer (C_{12}). ^{2}H NMR samples were prepared by adding 0.5 ml of the isolated ^{2}H-labeled poly-1-hexene with 0.5 ml of proteo-dichloromethane. As reference, a NMR tube with 1 ml of deuterated dichloromethane was prepared. The method of standard addition was used in quantification of active sites by ^{2}H NMR.

Diffuse Reflectance Infrared FT Spectroscopy

The catalyst was loaded on a cell in a nitrogen glovebox. Prior to the polymerization, all lines were flushed with N_2. The catalysts were exposed to ethylene flows up to 10 ml/min at 1 bar and 95°C. The FTIR spectrometer used was a Brukor Tensor 37 instrument, equipped with a MCT detector cooled with liquid N_2. The spectra were collected in the range of 800-4000 cm^{-1}, with a 4 cm^{-1} resolution, each averaged on 32 scans. A schematic overview of the setup is shown in Figure 4.28.

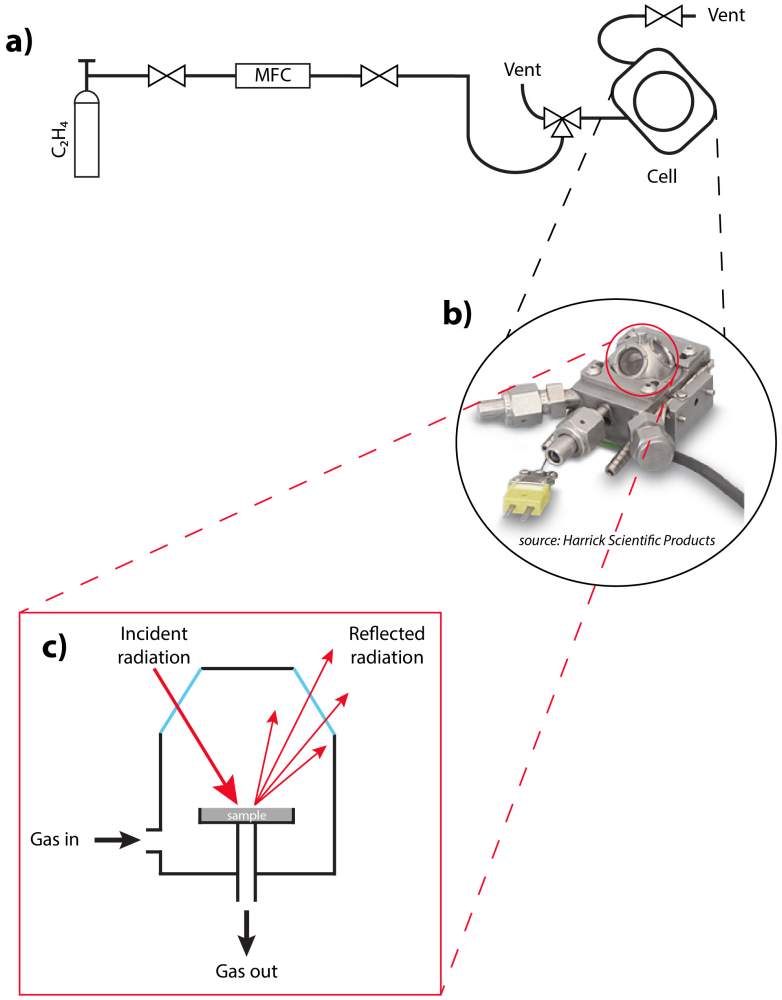

Figure 4.28: Schematic representation of the setup (a), which includes a DRIFTS cell (b). Part (c) shows the radiations and gas in-/outlet. Figure of the DRIFTS cell obtained from Harrick Scientific Products.

Optical Microscopy

Optical Microscopy was used complementary to SEM and CFM to visualize the catalyst particles. The microscope used was a Olympus BX41M with Olympus UMPlanFI 10x/0.3 and Olympus UMPlanFI 5x/0.15 objectives.

Scanning Electron Microscopy

Scanning Electron Microscopy (SEM) with Energy Dispersive X-ray (EDX) Spectroscopy was performed on a FEI Helios nanolab 600 DualBeam with an Oxford instruments Silicon Drift Detector X-Max nergy dispersive spectroscope. EDX mapping was performed with an electron beam of 5 kV and 0.2 nA. All SEM imaging was done using secondary electrons at 5 kV and 0.2 nA.

Staining of the catalyst samples

Staining process: general

The staining process was performed inside the glovebox or by using standard Schlenk techniques. The dyes used to stain the catalysts were PTCDA and perylene. Both dyes were dried under vacuum and stored inside the glovebox. Two different approaches of staining were used: direct staining and the bottom-up approach. In direct staining the full catalyst is stained, based on the work of Stork *et al.* [50]. Next to that, in the bottom-up approach the silica support is stained and the catalyst is built on top afterwards, which is shown in Figure 4.29 and based on the work of Jang *et al.* [51].

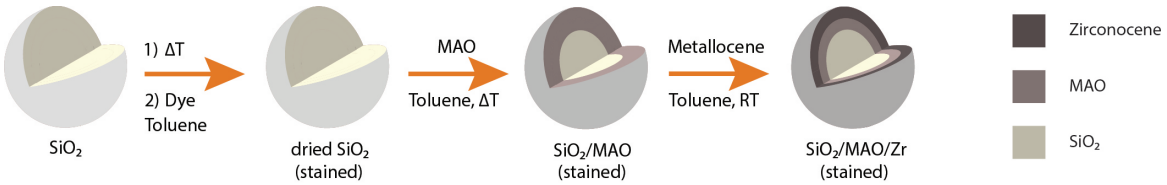

Figure 4.29: Synthesis pathway for the bottom-up approach of staining.

Direct staining: magnetic stirring in the glovebox

The various catalyst samples (0.050 gram) were added to a vial with a few grains of PTCDA (0.0001 gram) in pentane (2 ml). After stirring for 2 hours at room temperature, the (stained) catalyst was precipitated and the supernatant pentane solution was removed. In the case of perylene as dye, the various catalyst samples (0.010 gram) were mixed with perylene (0.002 gram) in pentane (2 ml). The purification was performed similarly to the PTCDA-stained samples.

Direct staining: mixing by hand at Schlenk line

The various catalyst samples (0.010 gram) were mixed in a flask with perylene (0.002 gram) in toluene (3 ml). Toluene was used as solvent since perylene has a higher solubility in toluene than in pentane. The solution was mixed by gentle shaking of the vial for 5 minutes. Afterwards, the samples were dried under vacuum.

Direct staining: mixing by hand in glovebox

Since both previously mentioned methods resulted in unwanted staining, the staining method was changed. Perylene (5 mM) was mixed with 50 mg of catalyst and 5 ml of toluene, wheras PTCDA (1 mM) was mixed with 50 mg of catalyst and 5 ml toluene. Both methods included mixing by gentle shaking of the vial for 5 minutes and were filtrated afterwards. The resulting stained catalysts were washed twice with toluene and dried with pentane (2 ml).

Bottom-up approach of staining

The silica obtained from Total was first dried to reduce the amount of surface hydroxyl groups. As can be read in the synthesis part of this experimental section on page 32, the silica is first dried at 120°C for 1 hour and afterwards dehydroxylated at 450°C for 4 hours. However, this results in the amount of silanols needed for the MAO impregnation. Since our silica first needs to be stained, the goal is to leave more silanols present, since our working theory is that the staining agent is coordinating to these silanols. Therefore the silica was dried at 375°C instead of 450°C. The silica was stained afterwards with both perylene (5 mM) and PTCDA (0.5 mM). The supports were characterized with both CFM and FTIR spectroscopy.

After confirming that the staining was successful, the stained silica was impregnated with methylaluminoxane. Standard Schlenk line techniques were used to perform a toluene reflux. PTCDA-stained silica (0.3332 g) was mixed with 3 ml of toluene and 0.8 ml of MAO (30 wt% in toluene). The reflux was initiated by mild stirring and heating, which was continued for 2 hours.

After confirming that the MAO impregnation was successful, the MAO-impregnation silica was impregnated with the zirconocene. The zirconocene (0.002 mg) was dissolved in 0.5 ml of toluene, after which SiO_2/PTCDA/MAO (0.1 g) was added. The mixture was stirred slowly (120 rpm) at room temperature for 2 hours.

Confocal Fluorescence Microscopy

In situ polymerization

The polymerization of the catalyst was performed by using a custom-made setup. This setup is shown in Figure 4.30. The cell was filled with stained catalyst inside the glovebox to prevent deactivation of the catalyst. The lines were flushed with N_2 for 10 minutes, to make sure water and oxygen were removed. An ethylene flow of 5 ml/min was used for the polymerization, which was performed at room temperature.

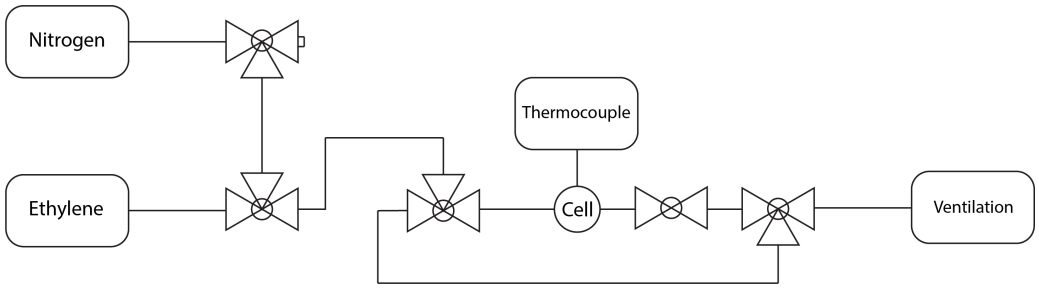

Figure 4.30: Schematic overview of the setup used for the CFM. On the left side, the inlet gases are shown, which flow through several three-way valves to arrive at the cell. A bypass is installed to flush the lines pre-polymerization.

Ex situ autoclave polymerization

Next to the *in situ* polymerization, the catalysts were tested in an autoclave setup at elevated pressures (18-30 bar) and room temperature. Since multiple reactions were performed, the corresponding pressures and reaction times are shown at the relevant result in the results section. The autoclave was loaded with 2 mg of stained catalyst and 3 ml of pentane. Next to that, the samples were tested inside a glass polymerization reactor with ethylene pressures of 1.6 bar, performed in the glovebox. This method was used since it is a relatively easy way to confirm the activity of the stained catalysts.

Characterization with CFM

The stained catalyst particles were studied with confocal fluorescence microscopy at room temperature on a Nikon Eclipse 90i microscope equipped with a Nikon LU Plan Fluor 10x, a Nikon LU Fluor 50x and a Nikon CF Plan 100x objective, while using standard settings for the measurements: slice distance - 10 μm, stack size - 256 x 256 μm. For excitation of the PTCDA dye, the 561 nm line of an argon laser was used. For excitation of the perylene dye, the 405 nm line of an argon laser was used.

N_2 Physisorption

The N_2 physisorption measurements were performed on a Micrometrics TriStar 3000. Both the nitrogen adsorption and desorption isotherms are determined by static volumetric measurements, *i.e.* measuring the adsorption equilibrium pressure after adding (or removing) stepwise amounts of nitrogen. The adsorption isotherm is used to calculate the specific surface area, using the Brunauer-Emmet-Teller (BET) model. The pore size distribution is calculated from the desorption isotherm using the Barrett-Joyner-Halenda (BJH) model. The total pore volume was defined as the single-point pore volume at $p/p_0 = 0.95$.

Results and discussion

Structural characterization

Before the influence of titanium in the polymerization process can be described, the structural characteristics of the catalyst need to be investigated first. This was done by using FTIR spectroscopy, SEM-EDX and N_2 physisorption. FTIR was used to study the vibrational changes in the spectra for each element of the catalyst (support, support + MAO and full catalyst). The different vibrations were assigned to determine the structural elements that were present in the samples. Figure 5.31 shows the different samples that were studied with FTIR. Graph (a) shows the spectra of the samples with a SiO_2 support, while graph (b) shows the spectra of the samples after addition of 2 wt% Ti (in a homogeneous distribution) to that support. In the blue lines of both graphs, the bare supports are shown. Evident in these blue spectra is the sharp peak at 3740 cm^{-1}, which originates from the isolated silanol groups that were present at the surface of these supports. In the 2080−1550 cm^{-1} region, vibrations from the silica support network can be found. In the blue line of graph (b), a minor group of ν-CH (stretching) vibrations is found (around 3050−2750 cm^{-1}), which originates from residual alkoxide that was used for the synthesis of this support. After MAO impregnation (yellow lines), the sharp peak from the isolated silanol groups shifted to a broader band around 3650 cm^{-1}, which indicates that these isolated silanol groups (that cause metallocene deactivation) are condensed upon MAO impregnation [32, 52, 53]. Another indication of the MAO impregnation can be found in the 3050−2750 cm^{-1} region and around 1430 cm^{-1}, assigned to ν-CH (stretching) and δ-CH bands (bending), respectively. Upon zirconocene impregnation, the main vibrational changes can be found in the δ-CH region, since the change in ν-CH vibrations is overshadowed by the MAO. The ligands of the zirconocene, however, can be identified with δ-CH modes at 1458, 1436 and 1377 cm^{-1}.

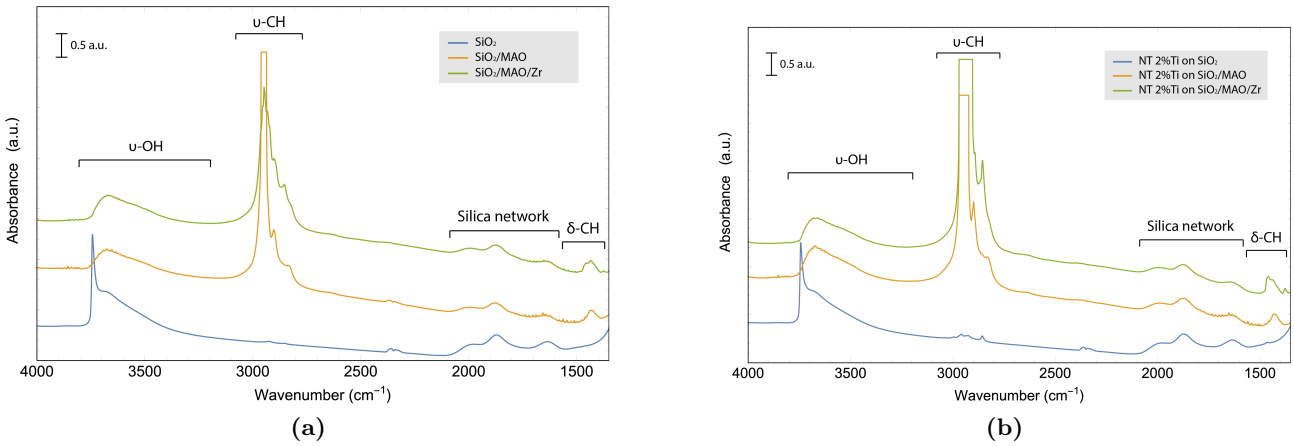

Figure 5.31: FTIR spectra of the SiO_2 supported samples (a) and the NT 2%Ti on SiO_2 samples (b).

Complementary to the vibrational study performed with FTIR, SEM was used to visualize the structure of the catalyst and EDX was used to perform elemental analysis on these catalyst particles. The catalyst particles were studied before and after polymerization on the DRIFTS setup, to study structural changes after polymerization. When comparing the SiO_2/MAO/Zr particles before (Figure 5.32a) and after (Figure 5.32b) polymerization, morphology changes aren't clearly visible. Some particles presented a popcorn-like structure, with the fragmentation of the particles occuring in an inhomogeneous way. This could be due to the packing of the DRIFTS cell, where the top layer of catalyst particles received an higher amount of ethylene.

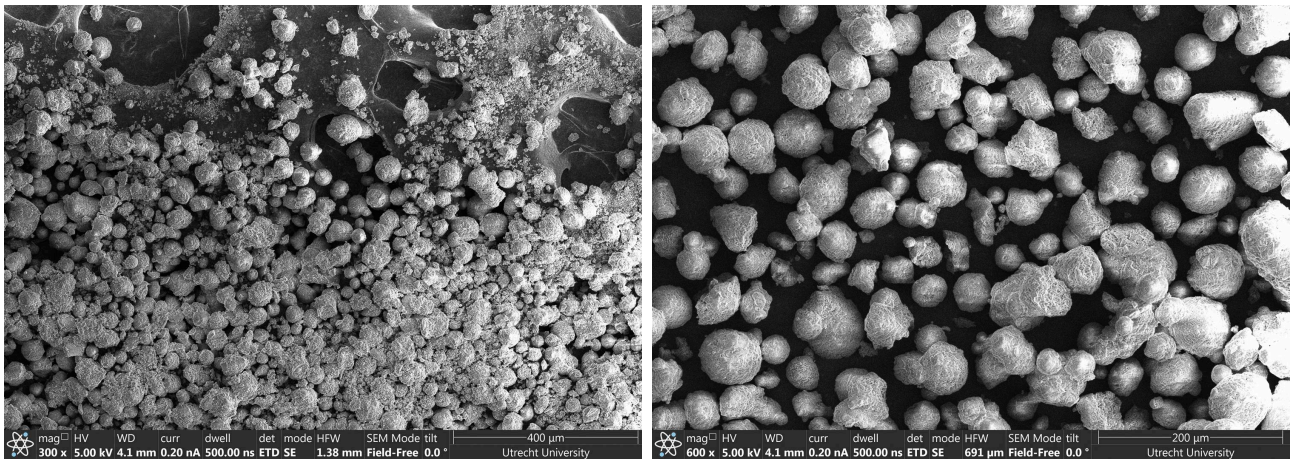

(a) **(b)**

Figure 5.32: SEM images of the SiO_2/MAO/Zr samples before (a) and after (b) polymerization.

However, when the NT 2%Ti on SiO_2/MAO/Zr particles are studied before (Figure 5.33a) and after (Figure 5.33b) polymerization, structural changes are evident. More catalyst particles seem to have fragmented, which indicates that the polymerization activity is indeed higher in the case of the 2%Ti sample. The particle sizes (before polymerization) were determined to be 32.6 ± 7.1 μm and 41.5 ± 9.1 μm for the SiO_2 and 2%Ti-supported catalysts, respectively. These numbers were achieved by the counting of 100 particles for each SEM scan using ImageJ.

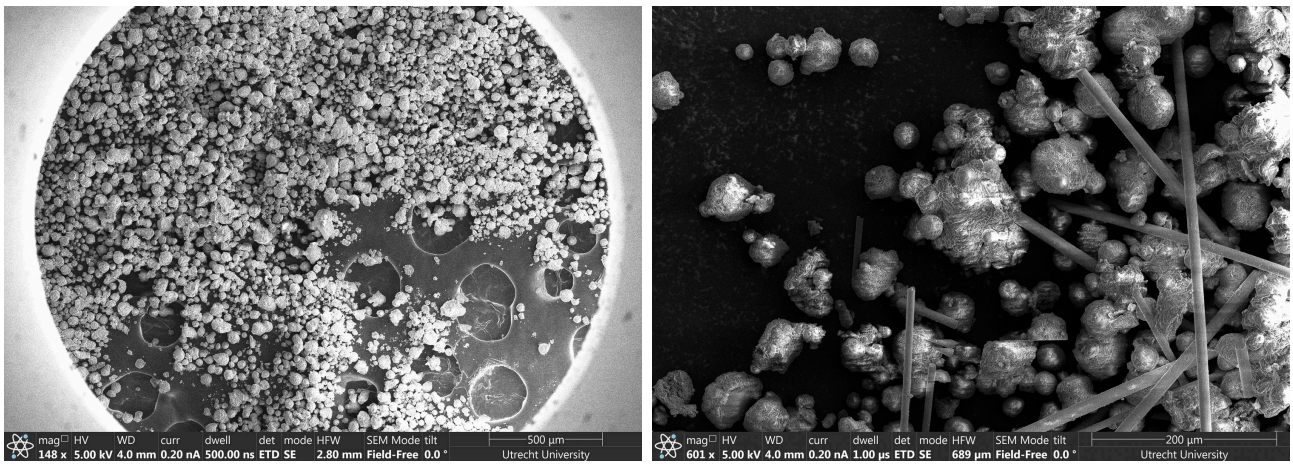

(a) **(b)**

Figure 5.33: SEM images of the NT 2%Ti on SiO_2/MAO/Zr before (a) and after (b) polymerization. The needle-like structures in (b) are quartz wool fibers.

The distribution of oxygen, silicon, carbon, aluminum, zirconium and titanium were studied in both the SiO_2/MAO/Zr and NT 2%Ti on SiO_2/MAO/Zr catalysts, by using SEM-EDX. The particle studied was an 'accidental' cross section, enabling imaging of the inner-structure of the catalyst particle. Figure 5.34 shows the distribution of these elements throughout the silica-supported catalyst particles. Evident from these EDX results is the amount of oxygen, silicon, carbon and aluminum that is present in this catalyst sample. Aluminum and part of the oxygen are originating from the MAO that is used as co-catalyst (see structural formula in Figure 1.6 on page 16). Silicon and oxygen are the building atoms for the silica that is used as support for this catalyst. Next to that, the carbon is originating from both the MAO and the ligands of the metallocene. However, since the sample is attached to a pin stub covered with carbon tape, the background signal of the carbon is oversatured. The zirconium is originating from the metallocene, in which zirconium is present as metal center. These EDX results show a homogeneous distribution of both the MAO and zirconocene.

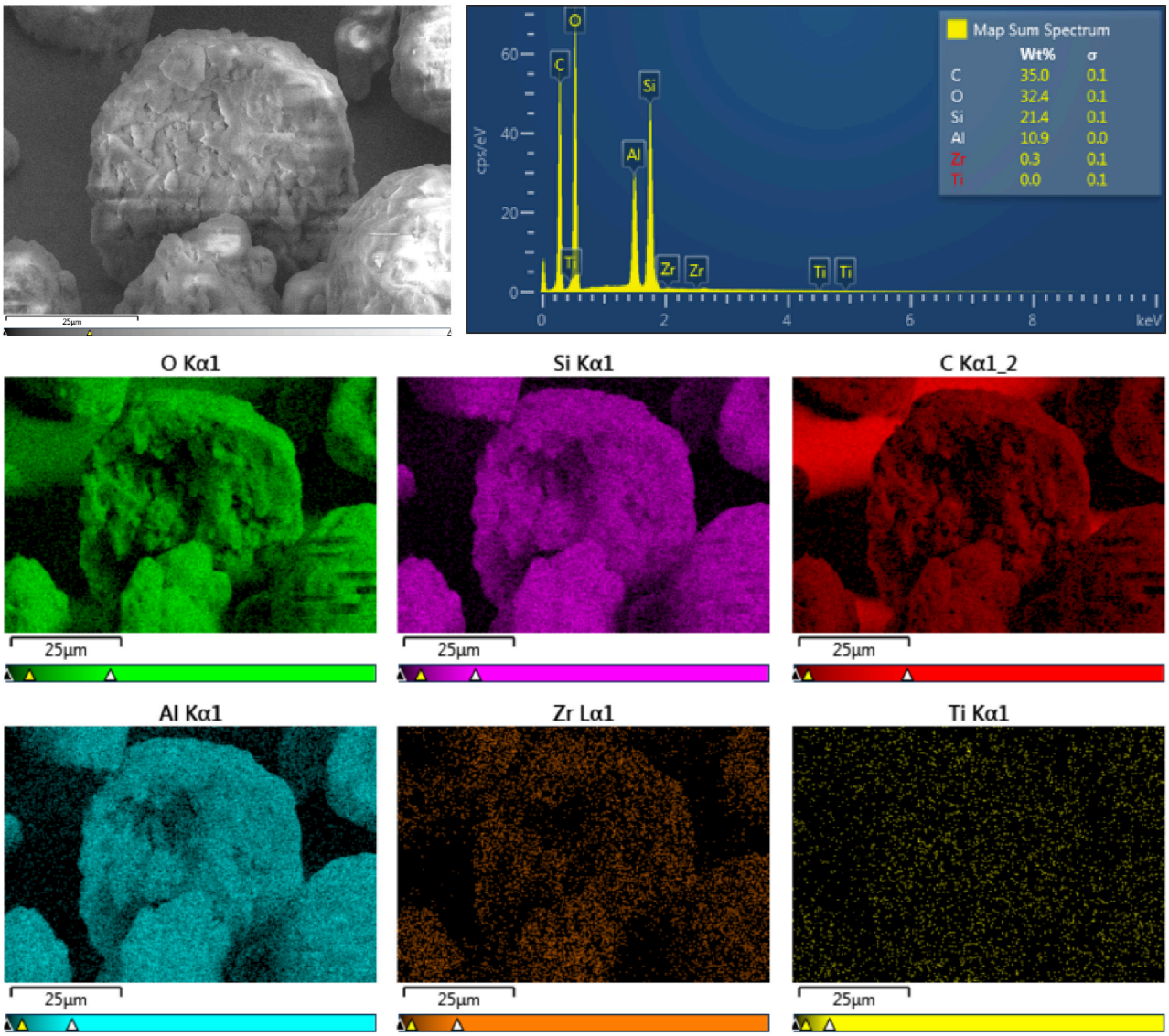

Figure 5.34: SEM-EDX results of the SiO_2/MAO/Zr samples. Indicated are the loadings of oxygen, silicon, carbon, aluminum, zirconium and titanium.

The results from the elemental analysis of the catalyst with the titanium-doped support are reported in Figure 5.35. The origin from the oxygen, silicon, aluminum, carbon was already explained on the previous page. As expected, the main difference between these two samples is the difference in titanium content. The loading of titanium in the support can not be determined from the EDX results, since the oxygen loading is originating from both the support and the MAO. However, the distribution of titanium is an important result obtained from this EDX analysis. This sample was synthesized to obtain an homogeneous distribution of titanium throughout the particle, which is confirmed by the cross-section of the catalyst particle, showing that titanium is homogeneously distributed throughout the particle.

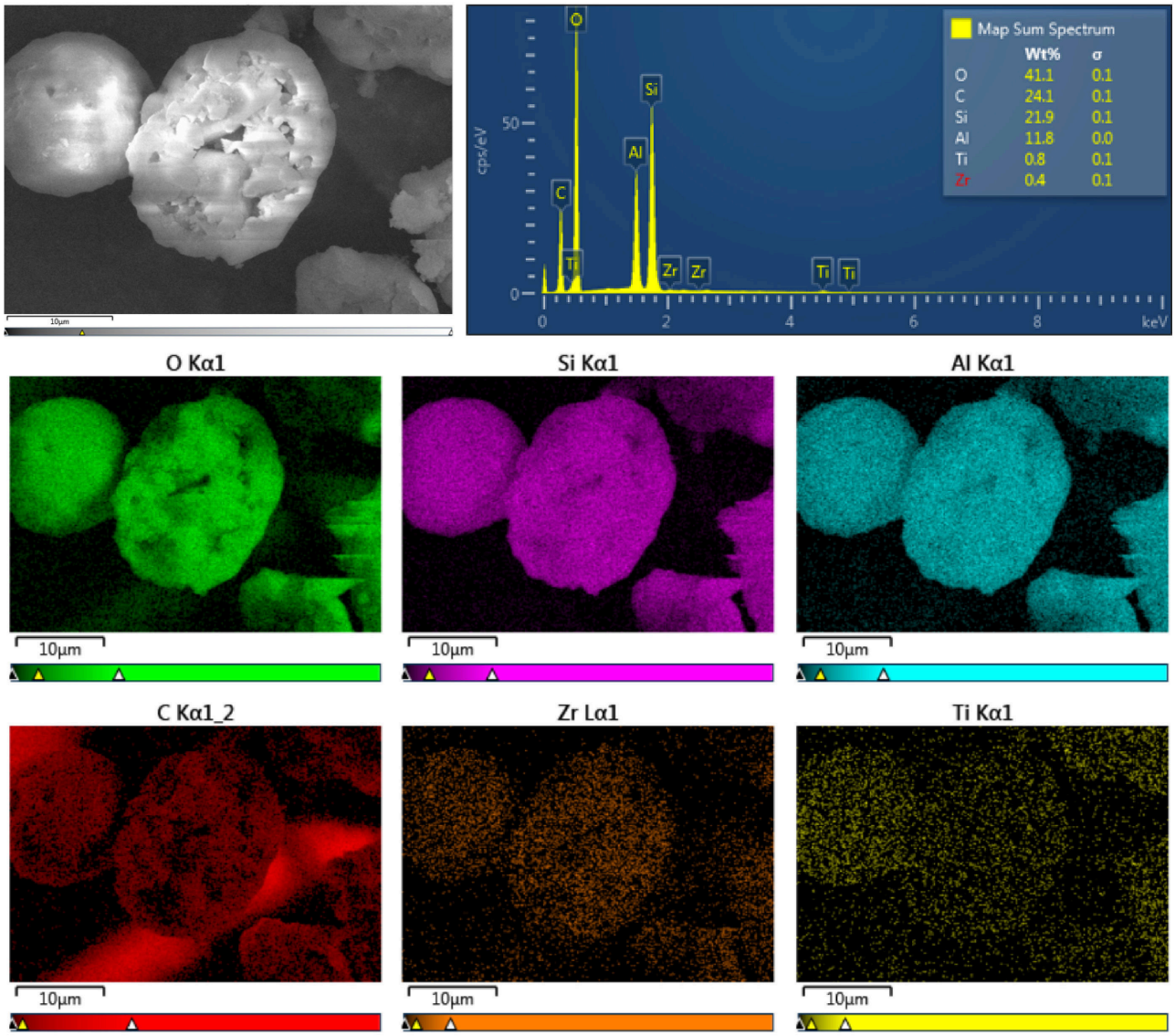

Figure 5.35: SEM-EDX results of the NT 2%Ti on SiO_2/MAO/Zr samples. Indicated are the loadings of oxygen, silicon, carbon, aluminum, zirconium and titanium.

Complementary to the both the FTIR vibrational data and SEM-EDX structural characterization data, the influence of titanium on the BET surface area and pore volume was determined with nitrogen physisorption. The results from these physisorption measurements are shown in Table 5.2.

Table 5.2: N_2 Physisorption data including the BET surface area and total pore volume (determined as the single-point pore volume at $p/p_0 = 0.95$). The samples used had homogeneous distribution of titanium.

Sample	**BET surface area (m^2/g)**	**Total pore volume (cm^3/g)**
SiO_2	239	1.33
Ti-SiO_2	258	1.40
SiO_2/MAO	325	0.60
Ti-SiO_2/MAO	325	0.68
SiO_2/MAO/Zr	284	0.54
Ti-SiO_2/MAO/Zr	238	0.52

As can be seen from the results is that both the BET surface area and total pore volume didn't change significantly upon titanium addition. The data is also shown in the graphs of Figure 5.36. Evident from the data of Figure 5.36a is the increase in surface area upon MAO impregnation, which has also been described in literature [54]. This increase in surface area is due to the anchoring reaction of the MAO with the siloxanes present in the support, resulting in an increase of the surface roughness and particle diameter. Next to that, the MAO impregnation and subsequently the metallocene impregnation resulted in a significant decrease in total pore volume (Figure 5.36b), since the pores became partially filled with the co-catalyst and catalyst. Since the MAO impregnation has the same effect on both the SiO_2 and Ti-SiO_2 support, it is expected that olefin monomer diffusion is comparable in both the SiO_2 and Ti-SiO_2 supported catalysts, excluding that as possible reason for the enhanced activity of the Ti-SiO_2 supported catalysts.

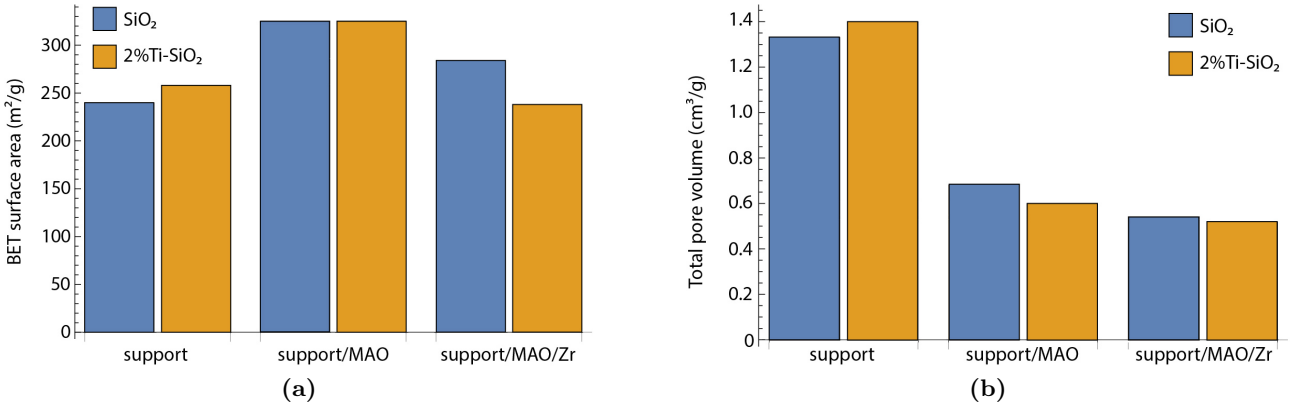

Figure 5.36: Graphs of the results from the N_2 physisorption, indicating both the BET surface area (a) and the total pore volume (b) of the SiO_2 and 2%Ti-SiO_2 supported samples.

Based on the data from the FTIR and N_2 physisorption measurements, it is clear that the influence of titanium is not significant in the change of structural vibrations, surface area or pore volume. However, faster fragmentation was observed by SEM, but due to the inhomogeneous packing of the DRIFTS cell, these results aren't conclusive enough.

Acidity

FTIR spectroscopy with pyridine as probe molecule was used to study the acidity of the samples. Two regions are of importance for an acidity study, namely the O-H stretching region (3800−3200 cm^{-1}) and the pyridine ring (C-H) bending region (1700−1350 cm^{-1}). In the presence of isolated silanol groups (3741 cm^{-1}), pyridine adsorbs on these groups, causing a downward shift to 3674 cm^{-1}. This downward shift can be observed in the two left graphs of Figure 5.37. It only occurs when there are isolated silanols present, *i.e* in the supports. The C-H bending region is important due to the ring vibrations of pyridine, which can be found on page 23. As mentioned before, the pyridine was allowed to adsorb onto the samples for 30 minutes at ambient temperature and low pressures (10-20 mbar). Afterwards the pyridine was desorbed by first vacuum desorption and afterwards temperature programmed desorption.

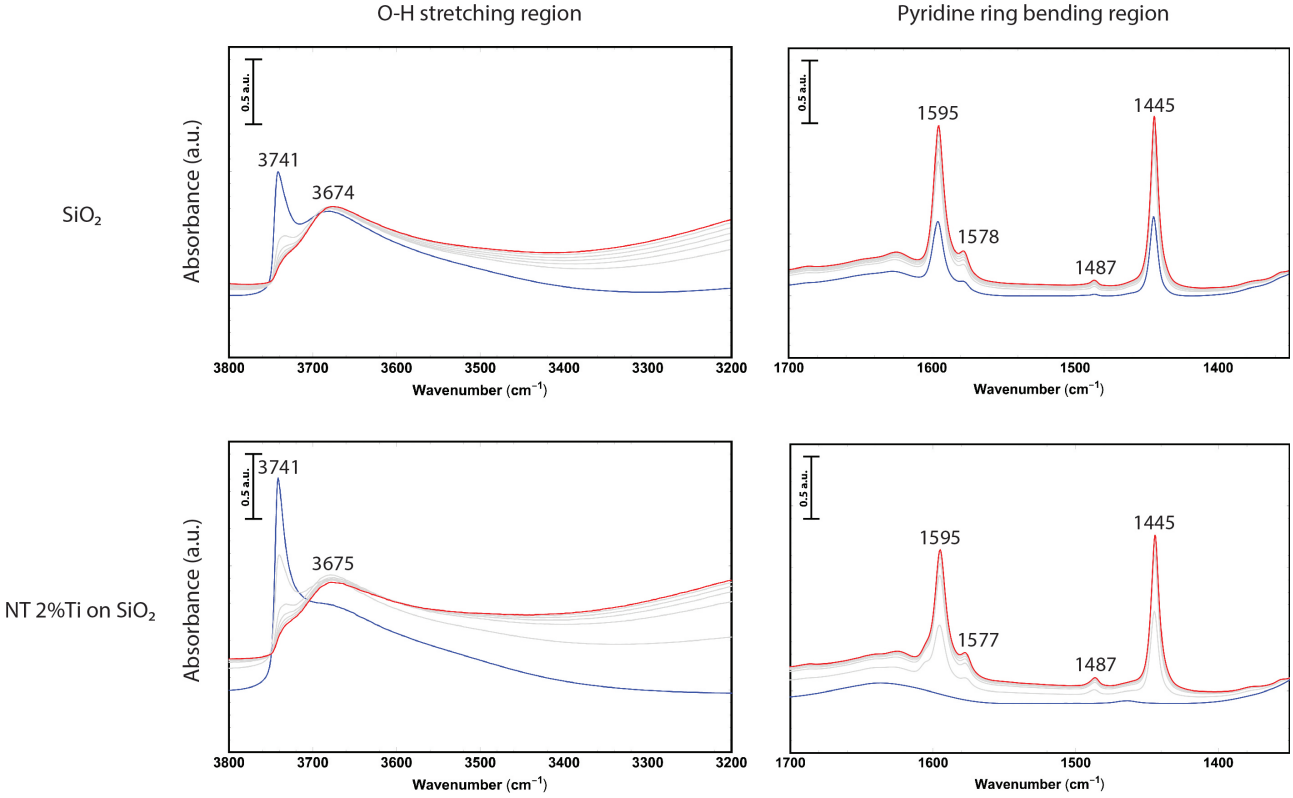

Figure 5.37: Pyridine FTIR spectra of the SiO_2 and the NT 2%Ti on SiO_2 supports, with spectra taken every 5 minutes. The spectra after 1 min (blue) and after 30 min (red) are highlighted.

Since the supports were known to have no (Lewis) acidity, the pyridine that adsorbed onto the surface of the supports was physisorbed pyridine. This was confirmed during the temperature programmed desorption, since all of the pyridine was removed at a temperature close to the boiling point of pyridine (boiling point = 115°C, was desorbed at 125°C). Since the peaks at 1540 and 1640 cm^{-1} were absent, no Brønsted acid sites were present as well. The pyridine ring vibration region was important however, since it confirmed the surface species of the studied sample. As can be seen when comparing Figure 5.37 with Figure 5.38 on the next page, the wavenumbers of the ring vibrations ν 8a (1595 to 1617 cm^{-1}), ν 19a (1487 to 1494 cm^{-1}) and ν 19b (1445 to 1452 cm^{-1}) are perturbed after MAO impregnation. This is completely in agreement with what is expected from the wavenumbers as mentioned in Table 3.1 on page 24, since the environment on which the pyridine could coordinate changed from silica (surface silanols) to alumina-like species (originating from the MAO).

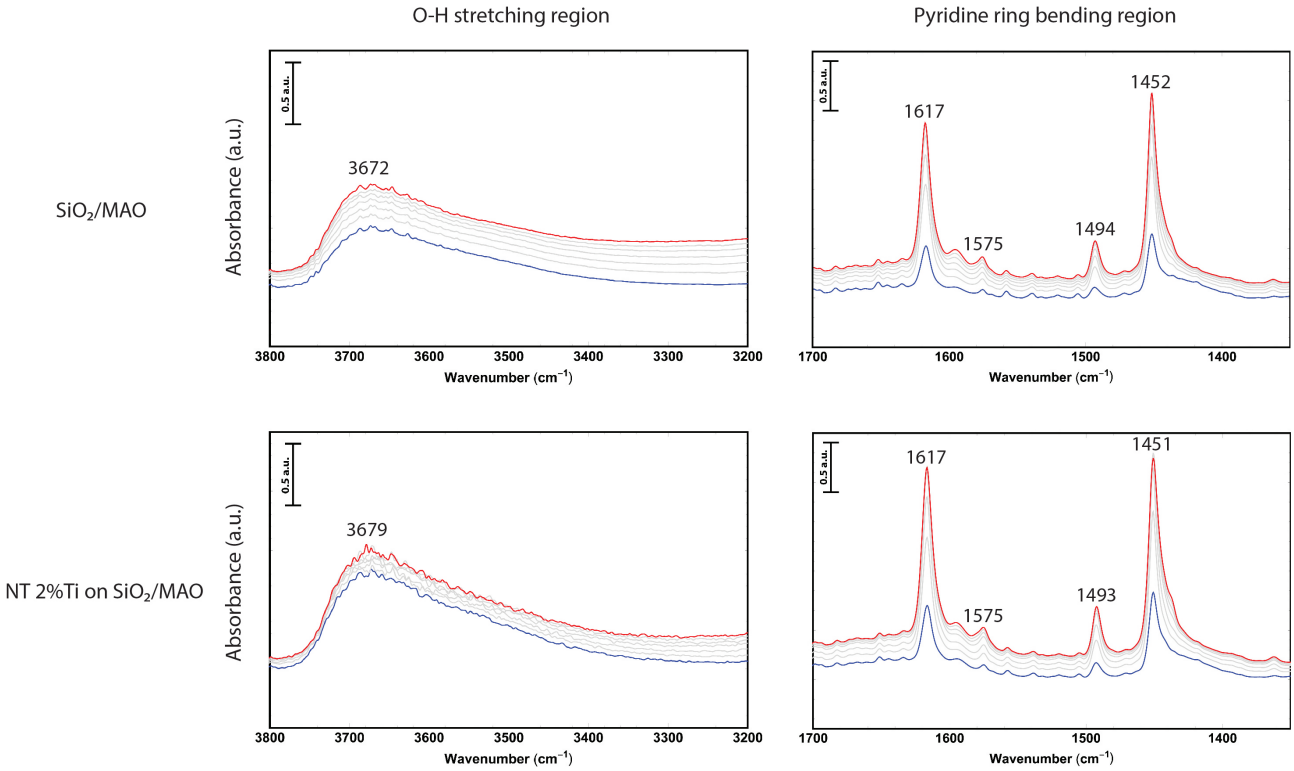

Figure 5.38: Pyridine FTIR spectra of the SiO_2 and the NT 2%Ti on SiO_2 supports after MAO impregnation, with spectra taken every 5 minutes. The spectra after 1 min (blue) and after 30 min (red) are highlighted.

As can also be seen from Figure 5.38 is the absence of the sharp 3741 cm^{-1} peak in the O-H stretching region, which indicates that the isolated silanols were already covered with MAO before pyridine adsorption. Based on the results from both the pure supports and the supports after MAO impregnation, it can be stated that these samples do not contain Brønsted acid sites, due to the absence of the 1638 cm^{-1} peak. This absence of Brønsted acidity has also been found in literature [55]. However, the MAO impregnated supports showed to have Lewis acidity. This was concluded from the higher temperature required to complete desorb the pyridine, indicating chemisorbed pyridine onto the samples. Next to the MAO covered samples, pyridine FTIR measurements have been performed on the full catalyst samples. The results from these measurements are shown in Figure 5.39, with similar wavenumbers when comparing to the MAO impregnated supports. This indicates that the nature of the acid sites that were present in the SiO_2/MAO samples did not change upon impregnation of the zirconocene. Next to that, it can also be deduced from these spectra that the Lewis acid sites have not reacted with the metallocene precursor, or have been recovered after the metallocene activation. Furthermore, we are not able to find proof of pyridine coordination to the metallocene based on Figure 5.39. In literature such an interaction has been described, but has not been analyzed in the C-H bending region with IR [56]. However, it could also be due to the low concentration of metallocenes in the full catalyst samples that the (possible) interaction between pyridine and the metallocene is not visible in the infrared spectrum.

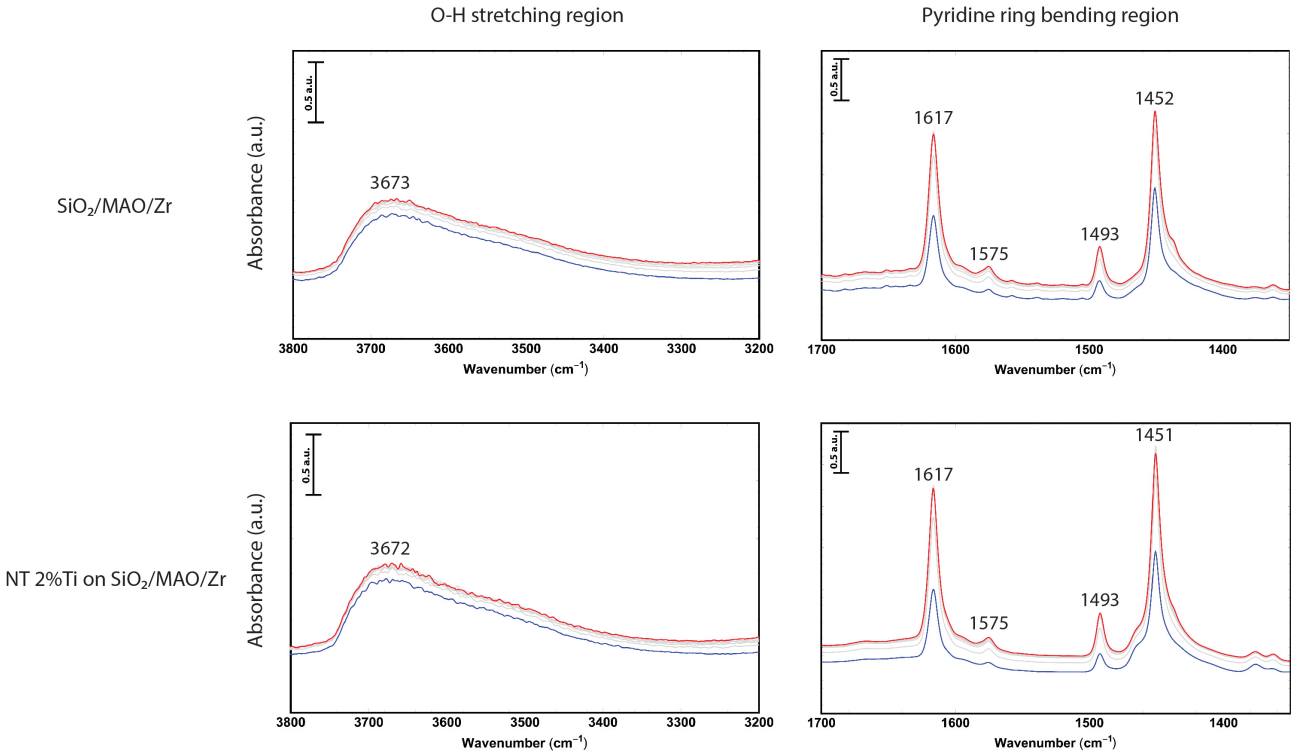

Figure 5.39: Pyridine FTIR spectra of the SiO_2 and the NT 2%Ti on SiO_2 supports after MAO and Zirconocene impregnation, with spectra taken every 5 minutes. The spectra after 1 min (blue) and after 30 min (red) are highlighted.

By using the equation 3.1 proposed on page 24, the concentration of the Lewis acid sites found in the MAO impregnated supports was determined. The acidity was quantified with the MAO samples, since the acidity didn't change upon zirconocene impregnation and lower effort was required to prepare the pellet used for the measurements. Using the area of the 1451 cm^{-1} peak, the concentration of acid sites was calculated and used to compare the silica-supported samples with the titanated samples. The samples that had a homogeneous distribution of titanium were characterized with a pellet weight of 6.5 mg and the samples with a higher titanium distribution on the surface had a pellet weight of 10.5 mg. The equation mentioned before accounts for this mass difference (by the ρ), however the assumption is that the thickness of the pellet is not taken (completely) into account in the equation. Since the measurements were performed in transmission mode, the thickness of the pellet is important for the amount of light that passes through the pellet. Next to that, the higher loadings of titanium in the samples resulted in a darker color of the material, which is also an important factor in transmission mode infrared spectroscopy. The acidity calculations resulted in the graph shown in Figure 5.40. Evident from this graph is the difference in acidity between the batch of homogeneously titanium distributed samples versus the samples with a higher amount of titanium at the surface. This is (probably) due to a combination of the larger thickness of the pellets and the darker color of the samples. This difference can not be contributed to the different distributions of titanium, because otherwise the acidities of both silica supports should be the same. Therefore the acidity of the samples is only compared relatively to each other within one batch. Based on these preliminary results, it can be determined that the acidity difference is not significantly increasing with an increasing amount of titanium, although further analysis might be necessary. However, since the activity increase of the titanium-doped silica support versus a pure silica support is 35%, it can be deduced that the acidity is not the main factor contributing towards the significant activity increase.

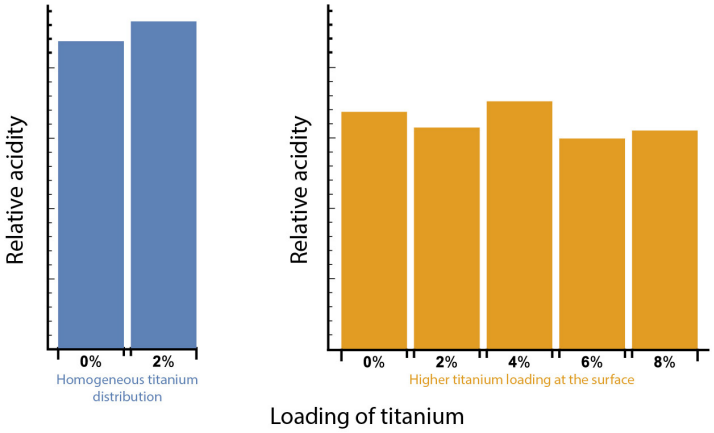

Figure 5.40: Acidity calculated based on pyridine FTIR results on both the samples with a homogeneous titanium distribution (in blue) and the samples with a higher titanium loading on the surface of the particles (in yellow).

To further investigate the strength of the acid sites, the TPD data of SiO_2 versus NT 2%Ti was compared. Specifically, the area of the 1451 cm^{-1} peak was plotted versus the temperature of pyridine desorption. The slope of the curve gives insight into the strength by which pyridine is chemisorbed, *i.e.* acid strength. The results from these measurements on the homogeneously distributed titanium samples are shown in Figure 5.41, where Mathematica (see script on page 73) was used to calculate the area of the corresponding peak. As can be seen from the left graph in Figure 5.41, the area of the NT 2%Ti on SiO_2/MAO sample (yellow dots) is higher at lower temperatures, which indicates that more pyridine is present at the surface of the sample. However, when the temperature is increasing, it is evident that the area of the SiO_2/MAO (blue dots) is decreasing relatively slower. This could indicate that the acid sites in the SiO_2/MAO sample are stronger in comparison to the NT 2%Ti on SiO_2/MAO sample. However, no other measurements did confirm or deny this observation. Next to that, it is also worth mentioning that the peak of the 19b ring vibration of pyridine (used to determine the acidity) was shifted 1 cm^{-1} more in the case of the SiO_2/MAO sample in comparison to pure pyridine (1452 versus 1451 cm^{-1}). This isn't a significant difference, but could indicate a higher acid strength.

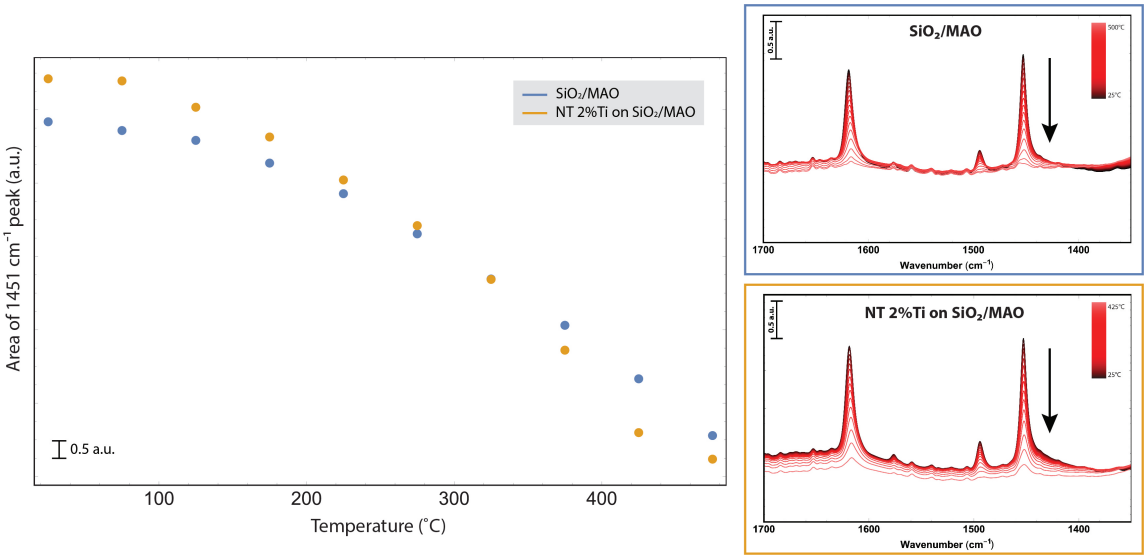

Figure 5.41: Temperature programmed desorption results that were performed after pyridine IR. The left graph shows the area of the 1541 cm^{-1} versus the temperature, while the right two graphs show the decrease in area with increasing temperature.

Counting of active sites

As mentioned in the theory, polymerization testing was used to study the activity and the amount of active sites of the catalyst samples. The following results are based on both ^{1}H and ^{2}H-NMR, where ^{1}H-NMR was used to determine the polymerization activity. ^{2}H-NMR on the other hand was used to study the amount of active sites, following the method of standard additions (as described on page 28). The sample choice was made, based on the DRIFTS results and amount of catalyst sample left (there was a limited amount of 2%Ti left), to pick the 0%Ti (least active) and 4%Ti (most active) as samples to study.

^{1}H-NMR results

The ^{1}H-NMR results show the amount of 1-hexene that is consumed during the reaction. The assumption has been made that all the consumed 1-hexene resulted in the formation of polyhexene. To quantify the amount of 1-hexene that was consumed, an internal standard (diphenylmethane) was added to the reaction solution. Figure 3.19 on page 27 shows the assignment of the ^{1}H nuclei of the molecules to the several peaks present in the spectrum. Based on the integrals of the different peaks, the conversion and activity of the catalysts was calculated. These integrals are determined by normalizing the internal standard to 1, as can be seen in the ^{1}H-NMR spectra (Figure I.51 and I.52) on page 70. The calculated conversion percentages and activities are shown in Table 5.3. The 1-hexene integral is the average of the integrals corresponding to the peaks assigned to 1-hexene. At first sight it seems that the 0%Ti was more active, since it has both a slightly higher conversion percentage (based on the relative decrease of 1-hexene) and a higher activity, but it formed less of the wanted vinylidene product. This vinylidene product is formed by the 1,2-insertion, as explained on page 15. An explanation for this lower amount of vinylidene could be a higher rate of the 2,1-insertion when comparing the 0%Ti to the 4%Ti catalyst. This would result in a higher concentration of vinylene. However, due to the overlap of the vinylene peak with a peak present in the initial spectrum (before polymerization, at around 6.0 ppm), it was not possible to quantify this peak. The activities were calculated based on the amount of converted 1-hexene, normalized per gram of catalyst used. The loading of metallocene on the catalyst was determined by Total to be around 2 wt%, and 25.6 wt% of this metallocene consists of zirconium. Based on these numbers the activity was calculated, defined as the amount of polyhexene formed (in grams) per mole of zirconium per hour. When comparing these numbers to for example the activity of polypropylene polymerization, a 10000 fold difference is observed in literature, reporting numbers of up to 10^5 gram polypropene per mol Zr per hour [57]. This could be due to the difference in polymerization conditions (10^5 gram PP/mol Zr/h was achieved at higher temperature and pressure), type of polymer formed (polyhexene versus polypropene) and composition of the catalyst (*e.g.* different metallocene, higher surface area or higher concentration of co-catalyst).

Table 5.3: ^{1}H-NMR results from the polymerization testing with the 0%Ti and the 4%Ti catalyst samples from the batch with the higher concentration of titanium at the surface.

	1-hexene integral	**int. std. integral**	**conversion**	**vinylidene**	**mg catalyst**	**activity (g/mol Zr/h)**
0%Ti before	3.945	1	-	-	49.8	-
0%Ti after	1.605	1	59.5%	0.115	-	35.8
4%Ti before	3.925	1	-	-	48.8	-
4%Ti after	1.635	1	58.5%	0.155	-	31.8

^{2}H-NMR results

Subsequently, the samples were purified and studied by ^{2}H-NMR, as described in the experimental section on page 34. Based on the ^{2}H-NMR data (Figure I.53 and I.54, starting from page 71), the amount of active sites was calculated. First of all, the absolute values for the dichloromethane (DCM), toluene and deuterated polymers peaks were calculated for each NMR spectra. Based on the absolute values of the dichloromethane peaks, the amount of deuterium corresponding to that peak was calculated by the method described on page 29. There was already a DCM peak present in the initial sample (sample V_0, contained only proteo-DCM and no deuterated DCM), due to the natural abundance of deuterium in proteo-DCM. Next to that, V_0, V_{1eq} and V_{2eq} are shown. These are the volumes of the starting solution (1 ml) and the volumes that were added after one (5 μl) and two (10 μl) additions, respectively. The area of the dichloromethane peak was plotted versus the multiplication of the known concentration of deuterated dichloromethane (which was added as external standard) and the volume of that deuterated dichloromethane (V_{std} * C_{std}). Based on the slope of that line, the value of K_A was calculated, which was subsequently used to calculate the concentration of deuterium (C_A) present in dichloromethane (by using the y-intercept). Since deuterated dichloromethane contains two deuterium atoms, this C_A value was halved (shown in the Tables 5.4 and 5.5 as 'concentration of deuterium (M)'). Finally, that concentration of deuterium was multiplied with the ratio of the polymer peak versus the DCM peak to obtain the concentration of deuterated polymers. Since it was assumed that each polymer was originating from an active site, this is also the number of active sites present in the catalyst sample. Table 5.4 shows the results corresponding to the 0 wt% titanium sample. The polymer concentration reported was 0.0021 M (sample V_0), since the most accurate determination of the active sites concentration can be performed in the initial sample. Next to that, Table 5.5 shows the results corresponding to the 4 wt% titanium sample. In this case, the polymer concentrations deviate significantly in each sample. This is since the ratio of polymer/DCM is increasing after the first addition of deuterated dichloromethane, where it should be decreasing (no polymer is added, only DCM). To overcome this aberration, the concentration of sample V_0 is used to compare numbers, with the concentration being 0.0022 M. It is therefore safe to say that the amount of active sites in both samples are within the margin of error of each other.

Table 5.4: ^{2}H-NMR results from the polymerization testing with the 0 wt% Ti catalyst sample from the batch with the higher concentration of titanium at the surface.

Sample	**Area DCM peak**	**V_{std} * C_{std}**	**Ratio polymer/DCM peaks**	**Concentration of deuterium (M)**	**Polymer concentration (M)**
V_0	539.78	0	1.640298	0.001254	0.002057473
V_{1eq}	1018.02	0.00470263	0.781036	0.003606	0.002816138
V_{2eq}	2153.07	0.00940527	0.316116	0.005957	0.001883092

Table 5.5: ^{2}H-NMR results from the polymerization testing with the 4 wt% Ti catalyst sample from the batch with the higher concentration of titanium at the surface.

Sample	**Area DCM peak**	**V_{std} * C_{std}**	**Ratio polymer/DCM peaks**	**Concentration of deuterium (M)**	**Polymer concentration (M)**
V_0	5061.57	0	0.062763	0.035746	0.002243552
V_{1eq}	4777.99	0.00470263	0.177164	0.038098	0.006749549
V_{2eq}	5701	0.00940527	0.137206	0.040499	0.005549831

Next to that, the amount of theoretically possible active sites was calculated based on the loading of metallocene and the amount of catalyst, being 0.0013 M. As can be seen from both tables, the number of active sites present in both samples is higher than theoretically possible. Although such a difference in active sites is difficult to justify, showing the limitations of this method, this indicates that there were certain erroneous assumptions causing a higher value than theoretically possible. Some assumptions made were the loading of the metallocene being exactly 2 wt%, the fact that all experimental work occurred in an identical way and that the polymers were filtrated out completely in the purification step. Combining the ^{2}H-NMR results with the results from ^{1}H-NMR, it can be seen that the 0 wt% Ti has a higher conversion of 1-hexene, but that it has a similar concentration of active sites. This could mean that there is a larger number of polymers formed per active site, *i.e.* a higher turnover frequency. However, it could also mean that the polymerization of the 0 wt% Ti sample occurs more frequently via the 2,1-insertion, creating dormant sites that are inactive for polymerization, but are contributing towards the amount of 1-hexene that is consumed. Since the amount of active sites after polymerization is similar in the 0 wt% Ti sample compared to the 4 wt% Ti, it could mean that the deuterium-labeled metallocene (shown in Figure 3.18 on page 27) was formed in smaller amounts.

Fragmentation

So far the results on the acidity and counting of the active sites have been obtained. Since it was shown that the acidity is (probably) not the contributing factor in the significant increase of polymerization activity upon titanium doping, fragmentation is the next aspect to investigate. The first step towards this fragmentation study is DRIFTS, which enables the characterization of the growth of the catalyst particles during the formation of polyethylene. During this *in situ* DRIFTS study, the growth of the polyethylene was monitored over time, allowing for a kinetic study on the polymerizing catalyst particles. Figure 5.42 shows the different stages of the polymerization process, as also explained on page 25. The stages are highlighted with different rate constants, which will be used to compare the different catalyst samples. DRIFTS measurements were performed on the batch with the heterogeneous titanium distribution, as this batch included samples ranging from 0 wt% to 8 wt% titanium, offering the possibility to investigate the influence of titanium loading in the fragmentation of the catalyst.

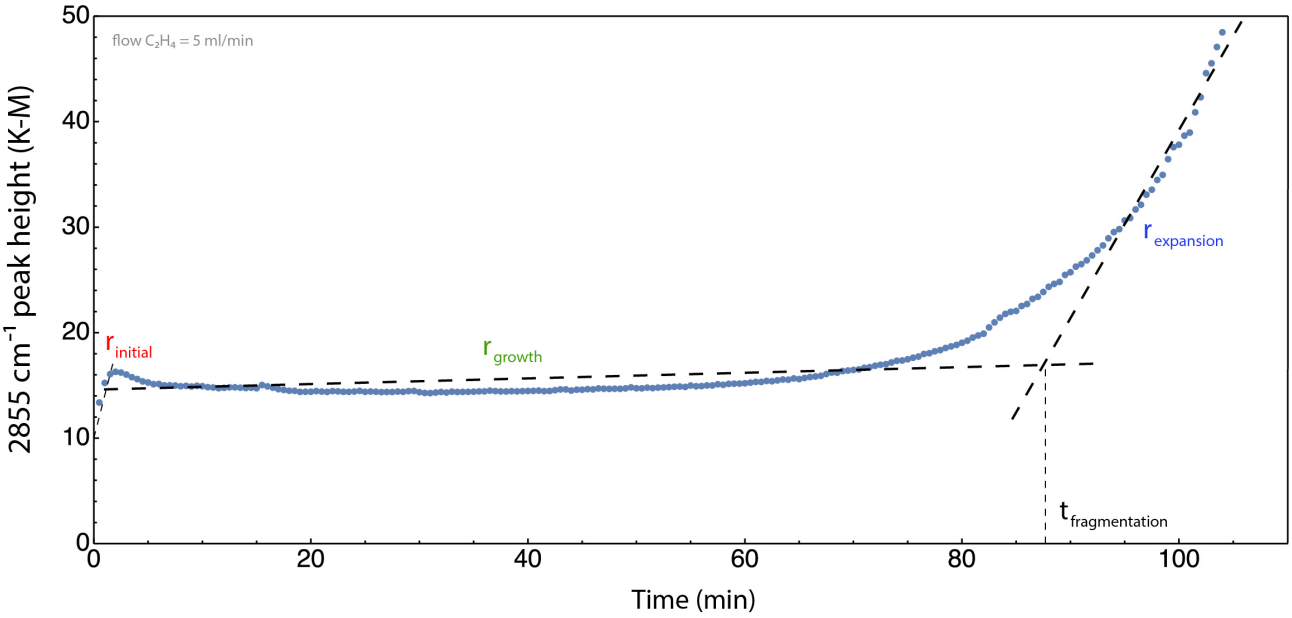

Figure 5.42: DRIFTS results from the SiO_2/MAO/Zr sample to visualize the different stages of polymerization, with included the initial stage, the growth of the particle and the expansion of the particle leading to fragmentation.

The initial stage is referring to the stage in which the ethylene diffuses first through the catalyst bed, then through the catalyst pores and starts forming small amounts of polyethylene. In the growth stage, these initial amounts of polyethylene are growing, without really fragmenting the particle. When the local build-up of stress is large enough for the particle to fragment, the particle grows in size more significantly. This is indicated in DRIFTS spectra with a sudden increase of the peak height. The intersection of the trend line of the growth stage and the trend line of the expansion stage is empirically assumed as the time of fragmentation.

The results from the kinetic study on the different stages of polymerization are shown in Figure 5.43. This graph shows the peak height of the 2855 cm^{-1}, which is assigned to symmetric CH_2 stretching vibration (originating from the formation of polyethylene) versus time. Evident from the data is the sharp increase in the initial stage of the 2%Ti-SiO_2/MAO/Zr (yellow line), which is caused by the removal of left over solvent that was used to synthesize and store the catalyst sample. This sharp increase could not be attributed to the formation of polyethylene, since it is not likely that polyethylene

formed initially and then leaves the catalyst sample again. Furthermore, it seems that both the 4%Ti (green line) and 6%Ti (red line) have a slight increase around 20 minutes and then remain constant with respect to the peak height for another 40 minutes, after which a sudden increase of peak height is observed. This second plateau that is formed could be due to the fragmentation of the outer surface, which results in a higher amount of ethylene that is able to enter the pores of the catalyst particle. However, this is based on pure speculation and couldn't yet be not confirmed.

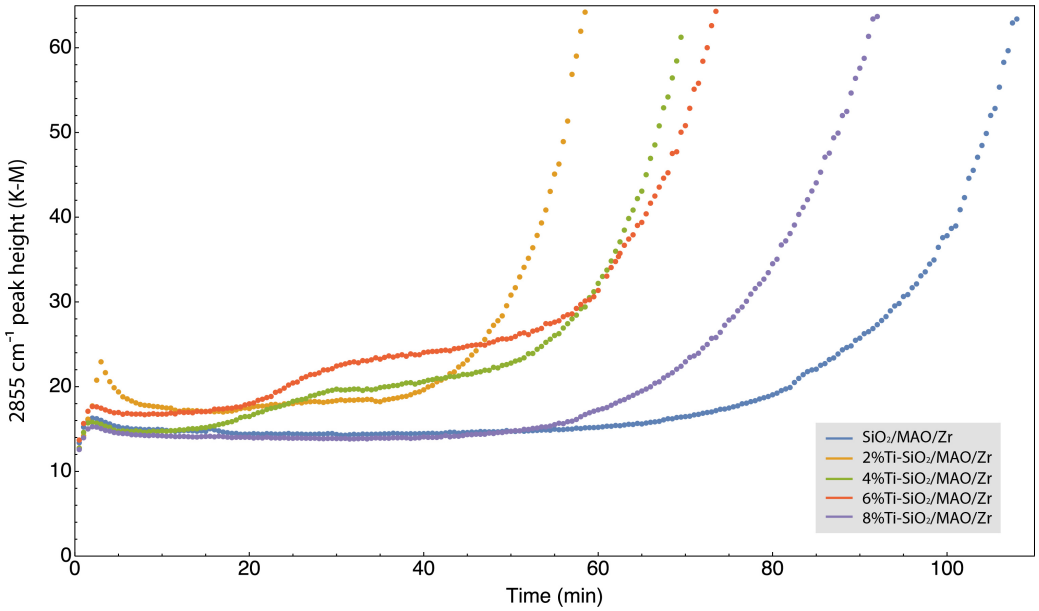

Figure 5.43: DRIFTS results from the samples with a higher concentration of titanium on the surface, with loadings of titanium ranging from 0 wt% to 8 wt%. The spectra is plotted as a function of the 2855 cm^{-1} peak height versus time.

The rate constants for the different stages of polymerization for each sample were calculated by taking the slope of the lines shown in Figure 5.42. The results from these calculations are shown in Table 5.6. Based on that data it can be concluded that the 2%Ti fragmented first, followed by both the 4% and 6%Ti samples. This confirms that the addition of titanium is beneficial towards the faster fragmentation of the catalyst, which could be a reason for the increase in activity. However, when a higher loading of titanium is present in the catalyst sample, the particle fragments relatively slower. It therefore appears that there is an optimum in fragmentation time when using the 2% or 4%Ti samples. The slowest fragmenting sample is, as was predicted based on the activity differences, the pure silica supported catalyst sample. However, it appears that the initial and expansion rate constants are higher for the pure silica supported catalyst in comparison to the 8%Ti catalyst. On the contrary, the moment of particle expansion is roughly 20 minutes earlier in the case of the 8%Ti catalyst.

Table 5.6: DRIFTS results from the kinetic study, with the initial, growth and expansion stage calculated as rate constants. The fragmentation time is based on the intersection of the growth trend line and the expansion trend line, as shown in Figure 5.42.

	Initial (cm^{-1}/min)	**Growth (cm^{-1}/min)**	**Expansion (cm^{-1}/min)**	**Fragmentation time (min)**
SiO_2/MAO/Zr	1.85	0.01	3.73	95
2%Ti-SiO_2/MAO/Zr	3.60	0.08	4.73	49
4%Ti-SiO_2/MAO/Zr	2.73	0.22	4.13	57
6%Ti-SiO_2/MAO/Zr	2.37	0.20	3.83	60
8%Ti-SiO_2/MAO/Zr	1.57	0.05	2.64	73

Next to using DRIFTS for studying the fragmentation of the catalyst samples, CFM was used as complementary technique. The visualization of the catalyst particles with CFM included a broad range of stained samples. As can be read in the experimental section (page 36), the direct staining method was modified multiple times, in the attempt to obtain useful results. Among the problems encountered were particle clustering, disintegration or loss of the catalytic activity. Finally, the bottom-up approach of staining, *i.e* the staining of the support and building the catalyst on top, was performed to avoid the aforementioned issues. In the following section, the failed attempts are reports first, followed by the bottom-up approach.

Direct staining: magnetic stirring in the glovebox

Initially the catalyst particles were stained by dissolving them in pentane and subsequently by stirring them with a magnetic stirring bar, which unfortunately resulted in particle disintegration (confirmed by SEM, as depicted in Figure I.55). However, this method proved that it was possible to stain the catalyst particles with both the perylene and the PTCDA dye. Since the spherical structure of the catalyst was disintegrated, the catalyst was deactivated after stirring. Figure 5.44A shows larger clusters of what appear to be spherical particles, however the particle diameter is tripled when compared to unstained particle diameters. Figure 5.44B shows larger domains of stained material, which corresponds to the SEM image mentioned before.

Direct staining: mixing by hand at Schlenk line

As the previous method showed to cause catalyst particle disintegration, the staining procedure has to be changed. The first parameter change was the solvent, namely from pentane to toluene. Next to that, the staining was performed at the Schlenk line, to keep the catalyst under inert atmosphere and to allow for toluene evaporation under vacuum. However, the CFM results show that the particles are clustered together. Figure 5.44C shows the SiO_2/MAO stained sample, which visualizes a cluster of blue spherical particles on a yellow compound. Based on the previous CFM results, it is assumed that the blue particles is the SiO_2/MAO, while the yellow is the (excess of) perylene dye. Figure 5.44D shows the full catalyst sample and evident from this image is the intense blue color of the catalyst particles. This arises the possibility of an interaction between the indenyl ligands of the zirconocene and the perylene dye. Due to this interaction, the conjugated system of the dye could have been altered/enlarged, which resulted in the more intense blue color. However, it could also simply mean that too much dye was used.

Direct staining: mixing by hand in glovebox

Since the staining at the Schlenk line resulted in an excess of the dye present (resulting in clustering of the particles), rinsing after the staining became necessary. The rinsing was performed with pentane instead of toluene (toluene was kept as solvent) to ensure an easier evaporation that can be achieved inside the glovebox. By performing this staining method, the particles remained spherical and didn't cluster. As can be seen in Figure 5.44E and F, the particles remained their vibrant blue fluorescence, which proves that this method could be potentially helpful in the fragmentation study. Next to that, the Figure 5.44F shows an important aspect of the use of confocal microscopy. The ability to probe the top (surface) of a particle gives structural details, while the bottom left image shows 'only' fluorescence, in some particles even a darker center and no structural details. This structural information is important for the fragmentation study that was the intentional goal of using CFM.

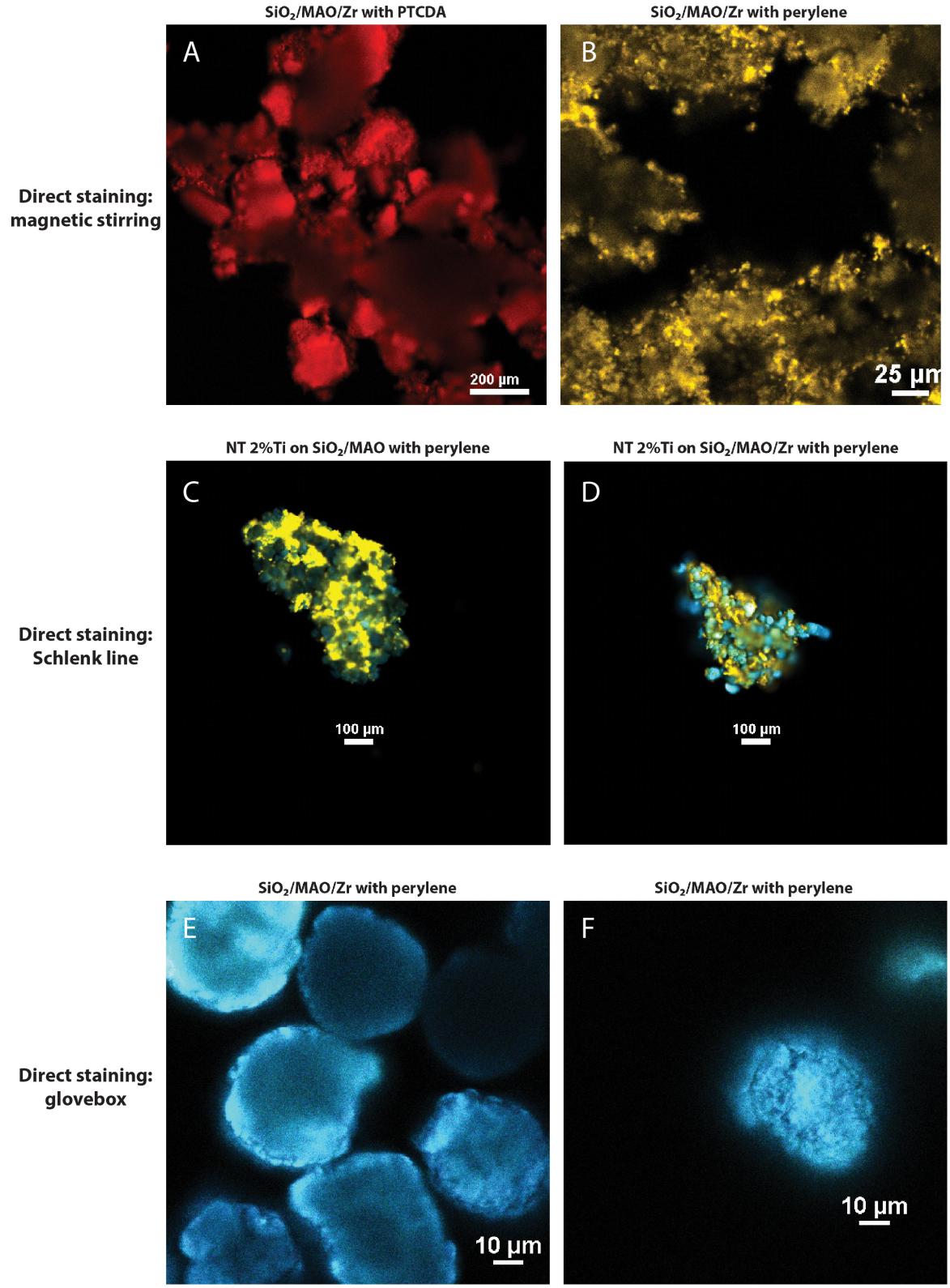

Figure 5.44: CFM results of the PTCDA and perylene stained samples, prepared via different methods of direct staining. Images A and B show particles disintegration, observed after the staining method that involved magnetic stirring. Images C and D show the particle clustering that is observed after staining at the Schlenk line. Finally, images E and F show spherical particles, obtained by direct staining in the glovebox.

Direct staining: autoclave polymerization

The samples stained with the last staining method were used for *in situ* polymerization in the setup shown Figure 4.30 on page 37. However, the fragmentation was too slow to be observable by using the *in situ* cell with CFM and the perylene-stained particles were barely visible. This could indicate that the catalyst particles were deactivated during the staining process (a possible reason could be pore blocking). To increase the fluorescencent signal and lower the amount of dye, the catalyst sample was stained with PTCDA. Lower concentrations of this dye are needed to obtain highly fluorescent samples, due to higher extinction coefficient of PTCDA compared to perylene [58]. The polymerization activity was tested in an autoclave reactor, by using 18.2 bar of ethylene pressure and a reaction time of 15 minutes. The results before and after autoclave polymerization show no clear fragmentation based on the CFM results (Figure 5.45), while ATR-IR on the other hand confirmed that polyethylene was formed (Figure I.57 on page 75). The peaks present (2916 cm^{-1} and 2849 cm^{-1}) are in agreement with the vibrations of polyethylene, found in literature [59]. Evident however are the larger clusters of fluorescent molecules in both CFM images, which could indicate that the concentration of the dye is too high. Optical Microscopy was used as complementary technique to study the samples and the results of these scans are shown in I.56 on page 74. The images from this microscope confirm that the dye diffused out of the particles during polymerization, explaining the intense red spots that are mainly visible after polymerization, since the PTCDA is the origin of the fluorescence.

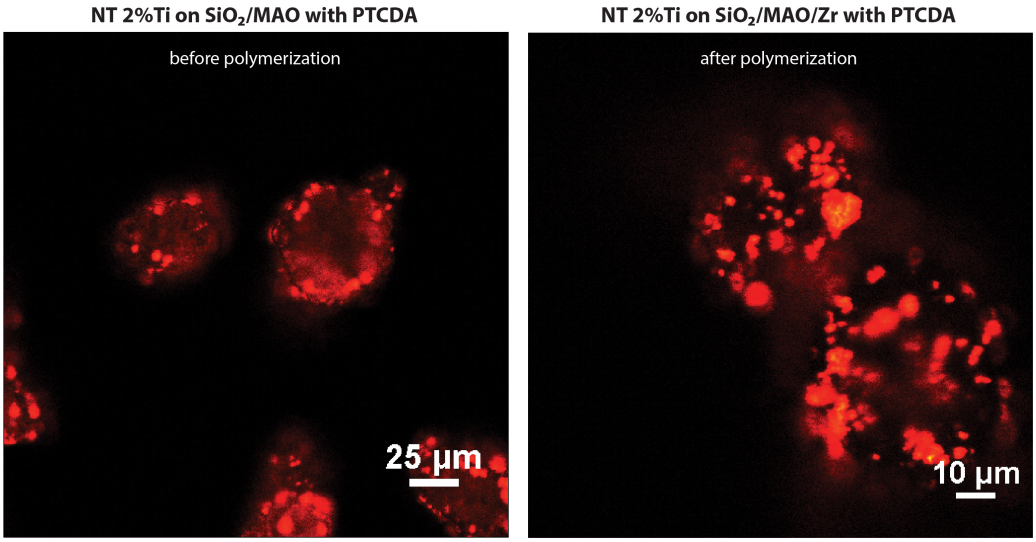

Figure 5.45: CFM results of the NT 2%Ti on SiO_2/MAO/Zr stained samples, before (left) and after 15 minutes of polymerization (right) at 18 bar of ethylene pressure. Prior to the polymerization, the catalyst was stained with the PTCDA dye.

Some polymer was formed as confirmed by ATR, although it was much less than expected out of those conditions (18 bar of ethylene pressure), indicating partial deactivation. Next to that, there were fluorescent "hot-spots" present, as confirmed by CFM and indicated by optical microscopy. This showed that the dye diffused out of the particles during polymerization. To observe fragmentation, it is crucial that the dye is distributed homogeneously throughout the catalyst particles, since otherwise it is not possible to study the fragmentation with CFM. This pointed towards a different method of staining, the so-called bottom-up approach.

Bottom-up approach of staining: silica drying and staining

The goal of the silica drying and staining was to obtain a stained SiO_2 with comparable amounts of silanols when compared to the 450°C dried SiO_2, to ensure anchoring of MAO and minimalize metallocene deactivation. The choice was therefore made to dry the SiO_2 at a lower temperature (375°C) and stain it afterwards with PTCDA. The results from the FTIR measurements performed to check the amount of silanols are shown in Figure I.59 on page 76. CFM scans were taken to study the supports after staining. The results from this measurement are shown in Figure 5.47A and B, which indicated that the staining was successful. In contrast to the staining method used before, this staining method resulted in homogeneously distributed fluorescent particles throughout the SiO_2 support.

Bottom-up approach of staining: MAO impregnation

The PTCDA-stained SiO_2 support dried at 375°C was used to impregnate with MAO. This MAO impregnation resulted in particles that still exhibit fluorescence, while being heated to 110°C (toluene reflux). This proved that the staining was sufficiently stable at elevated temperatures. The results from the CFM after MAO impregnation are shown in Figure 5.47C and D. Next to the maintaining of the fluorescence, it also seems that the particle morphology has changed upon MAO impregnation. The surface roughness of the particles has increased, when comparing the SiO_2 support versus the MAO impregnated sample. This increase in surface roughness was also the reasoning behind the increased surface area upon MAO impregnation, as studied with N_2 physisorption on page 43.

Bottom-up approach of staining: metallocene impregnation

The final step of the catalyst synthesis starting from a stained support was the metallocene impregnation. The results from the CFM are shown in Figure 5.47 (bottom row), which indicates that fluorescence is maintained throughout the synthesis of the full catalyst. Next to that, it seems that surface roughness has increased even further. To confirm whether the metallocene impregnation was successful, autoclave polymerization was performed on this stained catalyst sample. This autoclave polymerization was performed at 30 bar of ethylene pressure and the reaction was continued for 40 minutes, to ensure that both the catalyst is active and fragmentation is observable by CFM. During the autoclave reaction, the overall pressure was monitored and converted into an ethylene consumption. This ethylene consumption is studied in time (Figure 5.46), indicating that the catalyst is active and forming polyethylene. The slope of the graph is slowly decreasing, indicating that a plateau of ethylene consumption is forming. However, the amount of ethylene that was consumed is lower than expected with these conditions, indicating partial deactivation of the catalyst upon staining.

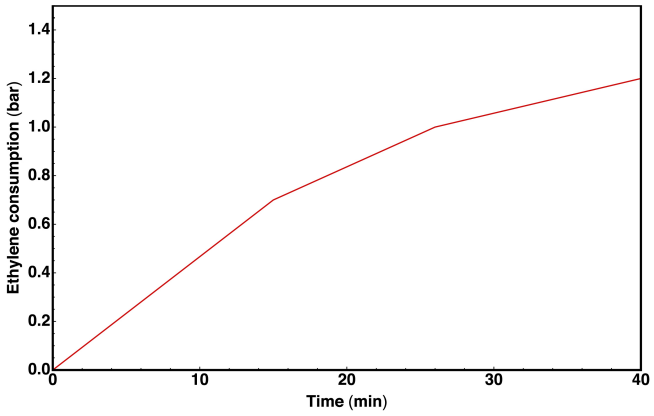

Figure 5.46: Graph showing the ethylene consumption of the catalyst during the autoclave polymerization at 30 bar of ethylene pressure.

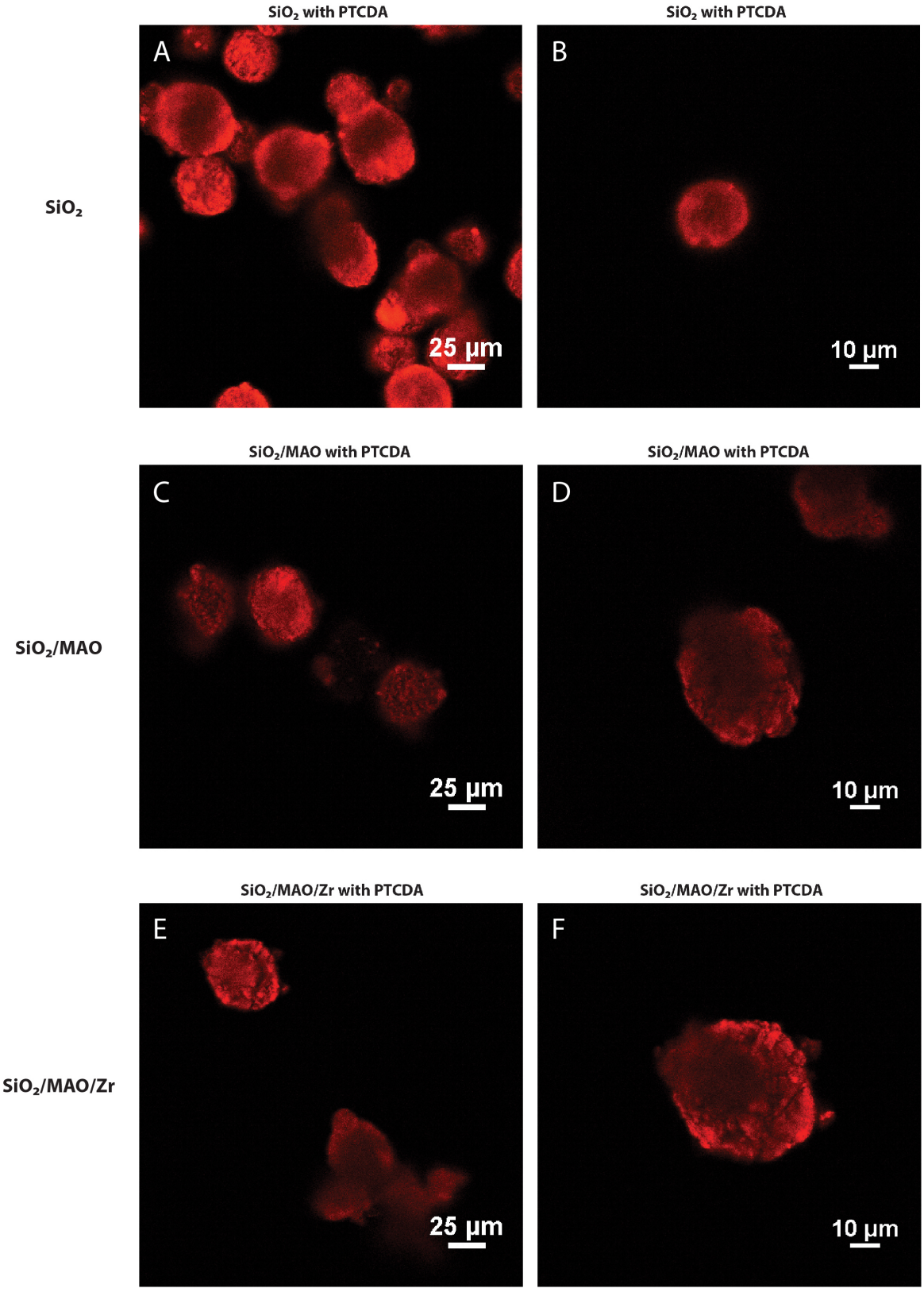

Figure 5.47: CFM results of the PTCDA stained samples, prepared via the bottom-up staining method. Images A and B show the stained SiO_2 support. Images C and D show the stained particles after MAO impregnation. Finally, images E and F show the full catalyst particles, obtained via metallocene impregnation.

The catalyst particles were studied with CFM after the autoclave polymerization. A representative set of particles is depicted in Figure I.60, where each image represents an individual particle. By scanning the particles at different depth levels (after each scan, the Z Control moved the stage 1 μm downwards), a 3D reconstruction of these particles was made. The results from these 3D reconstructions for each of the six particles are shown in Figure 5.49. Evident from each of the individual particles is that cracks are visible on the outer surface of the particles. Due to the limited penetration depth of the CFM, the most accurate results were obtained by probing the surface of the particles. The aforementioned cracks are visible since these spaces were occupied by non-fluorescent materials (*i.e.* polyethylene). This also concludes that there was no significant interaction between the PTCDA dye and the formed polyethylene during the autoclave polymerization, since otherwise the homogeneity of the fluorescence throughout the particles would have been maintained. Next to that, these CFM observations of fragmentation have not yet been observed in literature, in the case of a stained silica-supported metallocene. It therefore presents a novel method to compare the relative fragmentation of supported metallocenes with each other. However, since single particles are studied with the CFM, the conclusions that are made following from the comparison between different samples can be challenging. There are some advantages to prefer this technique over for example SEM, since using CFM saves a lot of time when it comes to 3D analysis of the particles. To study the inside of a particle with SEM, a Focused Ion Beam is required to 'cut' away the other half of the particle. Doing this for a set of six particles takes already a few days, while this analysis with CFM was performed in a few hours. On the other hand, the data obtained from SEM is more conclusive about the structural details, where in the case of CFM it can also be a contrast difference (due to the limited penetration depth).

To visualize that limited penetration depth of the CFM, a grid of images at different depth levels is shown in Figure 5.48. The particle visualized here is particle F in Figure 5.49. As mentioned before, scans were taken every 1 μm. Based on these individual scans it is clearly visible that the penetration depth is limited to a few microns. In the second row of scans, only the surface (outer circle) is displayed to exhibit fluorescence, while the center of the particle remains darkened. This phenomena has also been described in literature [60]. It unfortunately exposes the downside of using CFM in comparison to X-ray microscopy techniques, since these X-ray based techniques are able to perform a full three dimensional reconstruction. On the other hand, with respect to time and/or cost of these X-ray microscopy techniques, using CFM has major advantages.

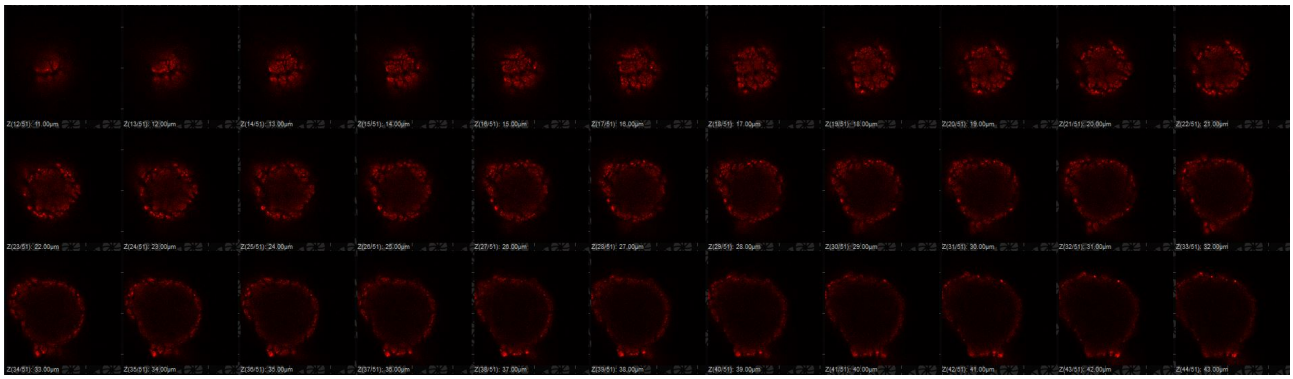

Figure 5.48: CFM results of the PTCDA stained catalyst samples, prepared via the bottom-up staining method. This image shows an grid of particle F in Figure 5.49 with scans taken every 1 μm.

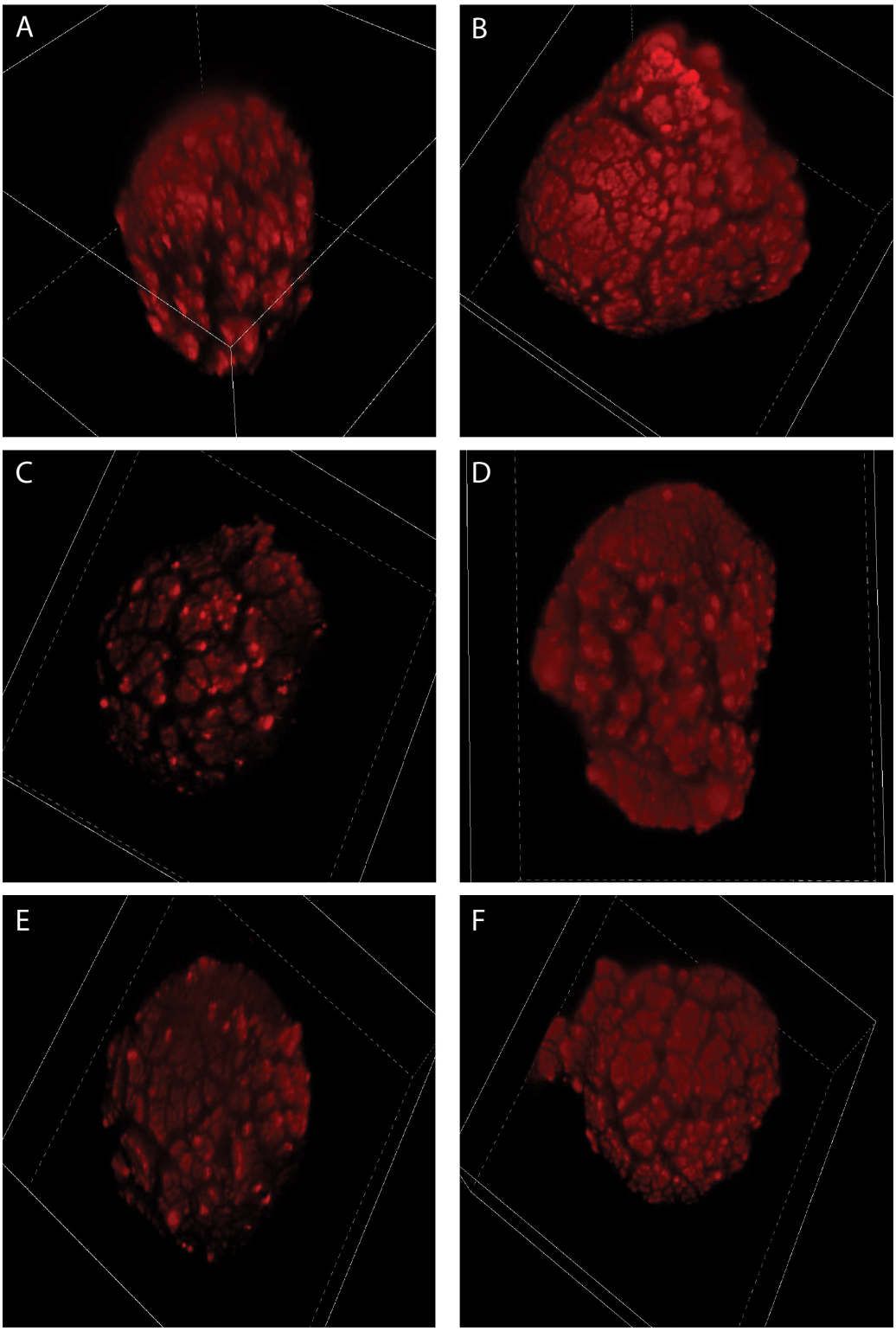

Figure 5.49: 3D reconstruction of the CFM results of the PTCDA stained catalyst samples, prepared via the bottom-up staining method. The catalyst samples were studied after autoclave polymerization at 30 bar of ethylene pressure. Each image represents an individual fragmented particle.

Conclusion

The work conducted during this master thesis was performed with the goal of clarifying the role of titanium when added to silica-supported metallocene catalysts. As mentioned in the introduction of this thesis, the addition of a few weight percent titanium to the silica support results in a significant increase of polymerization activity. The working hypothesis was that this activity increase was due to either the acidity, the number of active sites or the fragmentation of the catalyst. During this thesis, the influence of titanium on these aspects was studied with several characterization techniques.

FTIR spectroscopy with pyridine was used to probe the acidity of a wide variety of samples, ranging from supports to the full catalyst samples. The acidity was determined by using the area of the 1451 cm^{-1} peak (corresponding to a ring vibration from the pyridine) during the desorption after the pyridine was adsorbed onto the surface of the pellet. The relative acidity was compared between the silica-supported samples and after the addition of a range of wt% titanium to that support. After studying these samples, the acidity of the samples remained comparable when titanium was added (when compared within one batch), concluding that the main influence of the addition of titanium is not acidity related. Next to that, the amount of active sites was calculated via a method referred to as polymerization testing. In this method, the catalyst was studied after polymerization of 1-hexene. By using an internal standard, the amount of converted 1-hexene was calculated and the formed products were studied with ^{1}H-NMR. Based on these results, it was found that both the 0 wt% and 4 wt% titanium in the silica-supported catalyst reported similar activities, but the titanium-doped catalyst formed more of the desired (vinylidene) product. The amount of active sites was calculated using the method of standard additions, which was performed with dichloromethane during ^{2}H-NMR measurements. The results from these measurements reported that there was a comparable amount of active sites present in both samples, indicating that the both the amount of active sites and acidity are not the contributing factors towards the activity enhancement observed when titanium is added as promotor.

The catalyst particles were visualized with SEM-EDX and CFM, which resulted in structural information about the particles before and after polymerization. The results from the SEM-EDX indicated particle expansion and a change of the morphology of the particles after polymerization. It appeared that the titanium-doped catalyst samples fragmented more, indicating a higher activity. However, since these particles were polymerized in the reaction chamber from the DRIFTS setup, the fragmentation occured in an inhomogeneous way. It was therefore difficult to prove that the fragmentation was indeed further.

Next to that, the catalyst particles were studied with the CFM. Since the CFM required the samples to show fluorescence, the particles were first stained with a fluorescent dye. Multiple staining methods were performed and finally a method which started by staining the support and was followed by a MAO and metallocene impregnation afterwards, was shown to maintain the highest activity towards olefin polymerization. After polymerization inside an autoclave, fragmentation of the catalyst particles was observed and 3D reconstructions were made to visualize the particles. Since only the SiO_2-supported catalyst was studied this way, no comparison in terms of fragmentation behavior can be made based on this data.

The kinetics behind the fragmentation behavior of the catalyst were studied with DRIFTS. During these experiments, the peak height of the 2855 cm^{-1} peak was studied versus time, since that peak corresponds to symmetric CH_2 stretching vibration of the formed polyethylene. By studying a range of titanium weight loadings in the supports of the catalyst, a study of the different fragmentation times was undertaken. During these experiments, the different stages of polymerization were clearly distinguished, since the experiment starts with a sudden increase in formation of polymerization and continues with a steady growth of the polymer. After a period in time, the local build-up of stress inside the particles is too large and the particle fragments, causing a rapid increase of the 2855 cm^{-1} peak height. By comparing the fragmentation times and the rates of initiation, growth and expansion, an order of samples with respect to fragmentation time was formed. The catalyst with 2 wt% of titanium distributed in the supports reported the fastest fragmentation, followed by the 4 wt% and 6 wt%. Finally the 8 wt% and 0 wt% fragment the slowest. This indicates that there is an optimum in titanium loading when it relates to the fragmentation. In a patent by Total, an optimum in activity was also reported to be with the 2 wt% titanium sample [61].

The characterization study of the influence of titanium towards supported metallocene catalysts for olefin polymerization resulted in different observations. The approach was threefold; the acidity, activity and fragmentation of the catalysts were of interest. First of all, the acidity, based on the results from FTIR with pyridine as probe molecule, proved not to be the determining factor for the activity increase after addition of titanium. Next to that, the amount of active sites was determined in both the SiO_2-supported catalysts and after addition of titanium as promotor. These amounts of active sites were comparable to each other. Finally, a growth kinetics study was performed with DRIFTS on a range of titanium loadings, which resulted in a trend showing an optimum with the 2 wt% titanium catalyst, followed by the 4 and 6 wt% of titanium, respectively. Combining the comparable acidity, comparable number of active sites and faster growth of the samples containing titanium, it therefore appears that the titanium makes the support of the catalyst more brittle, which makes it easier to fragment. However, more work needs to be performed with either CFM, SEM or X-ray techniques to be conclusive about this.

Outlook

During this research that was conducted with the intented goal of finding the reason(s) behind the titanium influence in the silica-supported metallocene catalyst, several methods were used to obtain clarity about this phenomenon. However, there are still some methods or different aproaches that can be used for future research. In this chapter, the main areas of future research on this topic are explained.

CFM

As can be read in the results section, bottom-up staining of the silica-supported metallocenes was performed and the polymerization with these catalysts was conducted in an autoclave. However, to reach the intended goal of performing a fragmentation study with these catalysts, the titanium-doped supports also should be stained. The staining pathway is shown in Figure 7.50.

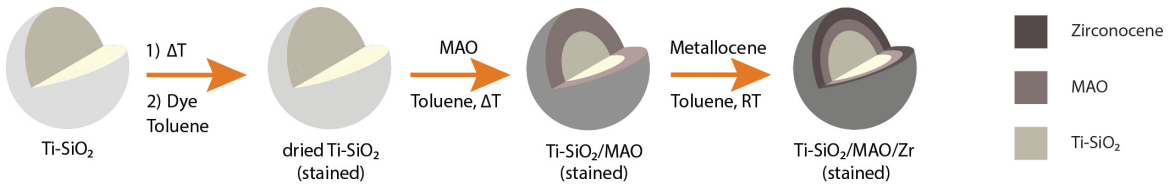

Figure 7.50: Synthesis pathway for the bottom-up approach of staining, starting with a titanium-doped support.

By performing the bottom-up approach with the titanium-doped supports, stained catalyst can be obtained and these catalysts can be used for the polymerization of ethylene. By using the same conditions for the autoclave as described in this thesis, fragmentation should be observed. The goal is to compare the stage of fragmentation and conclude whether the titanium-doped supported catalysts fragment in a different way. This could be done by for example a size comparison of the particles, a size comparison of the formed cracks in the particles and even the way of fragmentation (layer-by-layer versus sectioning).

Next to that, the method of polymerization could be varied. As described in the experimental section about CFM on page 37, polymerization could be achieved via either *in situ* or *ex situ* polymerization. Since *in situ* polymerization should in principle achieve more accurate results (since different stages of polymerization can be observed on the same particle), this method is worth researching. However, while investigating this technique during this thesis, the lower pressures of ethylene resulted in almost no fragmentation. A possible reason for that could be the longer time needed before the fragmentation is observable in the catalyst particle.

Autofluorescent metallocenes

To overcome the effort of staining the catalyst samples, one approach could be the use of an autofluorescent metallocene (*i.e.* a metallocene that exhibits fluorescence). One downside of this approach is the change of catalyst system, but it could be interesting as a proof of concept. In literature, several metallocene systems have been reported to show fluorescence. First of all, a mixed metallocene based on ferrocene was reported by E. Román *et al* [62]. Ferrocene has an iron metal center atom, so it is unactive for olefin polymerization. These ferrocenes have two different ligands, one cyclopentadienyl and one varying C_6-aromatic hydrocarbon ligand. When excited with 430 nm, the metallocene with the *p*-xylene ligand shows a fluorescence maxima at around 530 nm. It may be worth synthesizing a zirconocene with the same mixed ligands to study the effect on fluorescence. In the work of H. Sitzmann *et al.* it is shown that octaisopropylmetallocenes with lanthanide-based metal center (samarium, europium or ytterbium) exhibit fluorescene [63]. These three metallocenes were reported to show fluorescence by daylight or UV light (336 nm) irradiation. Both examples proof that it is possible to synthesize fluorescent metallocenes, but so far none have been reported with a zirconium metal center. Using an autofluorescent metallocene in combination with the adjustions to CFM that are reported on the previous page, it can be possible to perform a broader fragmentation study on the catalyst samples to study the influence of titanium in more detail.

FTIR with pyridine as probe molecule

As shown in the results about FTIR with pyridine, there were some unexpected results originating from the use of two different pellet weights for the different batches of titanium distribution. Since the two 0 wt% samples were significantly different in acidity, it showed that a more consistent data collection is required by using identical pellet weights. Next to that, multiple scans per sample should be taken and the data should be averaged to obtain the most accurate results for this acidity study.

UV-Vis spectroscopy

In the work of Mäkelä-Vaarne, who wrote a PhD dissertation about this topic for metallocenes in general, the underlying theory behind using UV-Vis spectroscopy for metallocenes is explained [64]. An UV-Vis study is possible since ligand-to-metal charge transfer (LMCT) transitions occur, due to the electron-rich ligands and the electron-poor metal center. Therefore the metal-to-ligand charge transfer (MLCT) and *d-d* transitions do not occur, simplifying the interpretation of the spectra. Two main areas of interest are present in the UV-Vis spectra, namely the 385 nm region (indenyl to zirconium charge transfer) and the 320 nm region (chloride to zirconium charge transfer). Next to that, it is possible to study the activation of the zirconocene by MAO [65]. In the aforementioned thesis, a different metallocene system was studied, but the results showed two different LMCT shifts. At [Al]/[Zr] < 30, the LMCT band shifts to higher energies (hypsochromic shift), while with [Al]/[Zr] of up to 7500, the LMCT band shifts to lower energies (bathochromic shift). The work from Mäkelä-Vaarne assigns these shifts to the methylation and the cationisation of the zirconocene, respectively. Since these studies were performed on different catalyst systems, it could be interesting to study the catalyst reported in this thesis with UV-Vis. Next to that, it was found that there is a correlation between the LMCT energy and the catalyst polymerization activity. Since the titanium-doping in the catalyst leads to an increase in polymerization activity, it could be interesting to study the spectral changes between a silica-supported catalyst and a catalyst that has a few weight percent of titanium mixed into the support.

Acknowledgements

This work was not possible without the help of many people, making it able to complete my thesis. First of all, I would like to thank my project supervisor, Bert Weckhuysen, for giving me the possibility to conduct my research at ICC. The fact that you gave me the opportunity to attend my first conference was a nice highlight of my past year of study. Next to that, the feedback that you provided throughout this thesis helped me to push myself even further. I would also like to thank Florian Meirer for being my second supervisor, especially for his feedback during my halfway presentation. Silvia (Zanoni), I would like to thank you as well for being my daily supervisor for the past year. It has been a year of research with a lot of ups and downs, especially the fire that took place right next to the glovebox, setting us back a few weeks. However, your motivation to work around this accident helped me to conduct more research in that 'down time' than I initially expected. Next to that, your way of providing assistance and feedback is something that I experienced as really helpful. The fact that I had the feeling that we were working together towards a common goal was something that put me at ease right from the start of my thesis. I would like to wish you all the best in the upcoming years of research!

There are also a lot of people who helped with the experimental part of this thesis. First of all, Max (Werny), I would like to thank you for all the time you invested in the CFM-part of this thesis. It was a tough time with a lot of issues that needed to be handled, but it resulted in a nice result in the end. Next to that, I would like to thank Paul Pletcher for his assistance with the polymerization testing, a part of research that you devised. Iris ten Have (SEM-EDX), Marjolein Velthoen (FTIR), Donglong Fu (CFM) and Anne-Eva Nieuwelink (CFM) are thanked for their assistance in the explanation of the mentioned characterization techniques. Koen Bossers is thanked for his assistance with glovebox-related experiments. Finally, Laura de Kort, thanks for your opinions on the FTIR data, it helped me to analyze the data more extensively! The whole group of ICC is thanked for their open attitude towards (master) students, especially during the social activities, which has made it a comforting stay.

The research was conducted in cooperation with Total Research and Technology in Feluy, Belgium. I would like to thank them for providing the funding and samples to conduct this research.

Last but not least, the non-scientific acknowledgements go to the other master students of ICC, with Jim de Ruiter, Jeroen Dubbeld, Oscar Brandt Corstius, Stefan van Vliet, Kristiaan Helfferich and Onno van der Heijden in particular. You guys made the several coffee and lunch breaks a real moment of relaxation and created a nice atmosphere! It sometimes feels like the past year went by in a brief moment of time. Finally, I would like to thank Rosalie for all her support and feedback on the presentations/poster, which was a nice opportunity to translate my research to a non-chemist!

Bibliography

[1] Freedonia Group, "World Polyethylene," 2014.

[2] W. Kaminsky, "Discovery of methylaluminoxane as cocatalyst for olefin polymerization," *Macromolecules*, vol. 45, no. 8, pp. 3289–3297, 2012.

[3] W. Kaminsky, M. Miri, H. Sinn, and R. Woldt, "Bis(cyclopentadienyl)zirkon-verbindungen und aluminoxan als Ziegler-Katalysatoren für die polymerisation und copolymerisation von olefinen," *Die Makromolekulare Chemie, Rapid Communications*, vol. 4, no. 6, pp. 417–421, 1983.

[4] B. Jongsomjit, S. Ngamposri, and P. Praserthdam, "Catalytic Activity During Copolymerization of Ethylene and 1-Hexene via Mixed TiO_2/SiO_2-Supported MAO with rac-Et$[Ind]_2ZrCl_2$ Metallocene Catalyst," *Molecules*, vol. 10, no. 6, pp. 672–678, 2005.

[5] J. C. W. Chien, "Supported metallocene polymerization catalysis," *Topics in Catalysis*, vol. 7, no. 1-4, pp. 23–36, 1999.

[6] C. Willocq, M. Slawinksi, and A. Vantomme, "US Pat. 9475893 B2 (Modified catalyst supports)," 2016.

[7] B. M. Weckhuysen and R. A. Schoonheydt, "Alkane dehydrogenation over supported chromium oxide catalysts," *Catalysis Today*, vol. 51, no. 2, pp. 223–232, 1999.

[8] A. Peacock, "Handbook of polyethylene: structures, properties, and applications," 2000.

[9] L. Wang, B. Yang, B. Yin, N. Sun, J. M. Feng, and M. B. Yang, "Thermorheology and crystallization behaviors of polyethylenes: Effect of molecular attributes," *Journal of Macromolecular Science, Part B: Physics*, vol. 52, no. 11, pp. 1479–1493, 2013.

[10] P. Cossee and E. J. Arlman, "Ziegler-Natta catalysis III. Stereospecific polymerization of propene with the catalyst system $TiCl_3$-$AlEt_3$," *Journal of Catalysis*, vol. 3, no. 1, pp. 99–104, 1964.

[11] H. Hagen, J. Boersma, and G. van Koten, "Homogeneous Vanadium-Based Catalysts for the Ziegler—Natta Polymerization of α-Olefins," *Chemical Society Reviews*, vol. 31, pp. 357–364, dec 2002.

[12] W. Kaminsky and W. H., "Influence of supported metallocene catalysts on polymer tacticity," *Topics in Catalysis*, vol. 7, pp. 61–67, 1999.

[13] J. Hogan and R. Banks, "US Pat. 2825721 (Polymers and production thereof)," 1958.

[14] M. P. McDaniel, "A Review of the Phillips Supported Chromium Catalyst and Its Commercial Use for Ethylene Polymerization," *Advances in Catalysis*, vol. 53, pp. 123–606, 2010.

[15] J. Boor Jr., "Ziegler-Natta catalysts and polymerization," 1979.

[16] J. B. Soares and T. F. McKenna, "Polyolefin Reaction Engineering," 2013.

[17] T. J. Kealy and P. L. Pauson, "A New Type of Organo-Iron Compound," *Nature*, vol. 168, p. 1039, dec 1951.

[18] S. A. Miller, J. A. Tebboth, and J. F. Tremaine, "114. Dicyclopentadienyliron," *Journal of Chemical Society (Resumed)*, no. 0, pp. 632–635, 1952.

[19] G. Wilkinson, M. Rosenblum, M. C. Whiting, and R. B. Woodward, "The Structure of Iron Bis-Cyclopentadienyl," *Journal of the American Chemical Society*, vol. 74, pp. 2125–2126, apr 1952.

[20] B. Wang, "Ansa-metallocene polymerization catalysts: Effects of the bridges on the catalytic activities," *Coordination Chemistry Reviews*, vol. 250, no. 1-2, pp. 242–258, 2006.

[21] O. Olabisi, M. Atiqullah, and W. Kaminsky, "Group 4 metallocenes: supported and unsupported," *Journal of Macromolecular Science, Reviews in Macromolecular Chemistry and Physics*, vol. C37, no. 3, pp. 519–554, 1997.

[22] D. S. Breslow and N. R. Newburg, "Bis-(Cyclopentadienyl)-Titanium Dichloride —Alkylaluminum Complexes As Catalysts for the Polymerization of Ethylene," *Journal of the American Chemical Society*, vol. 79, no. 18, pp. 5072–5073, 1957.

[23] H. Sinn, W. Kaminsky, H. Vollmer, and R. Woldt, "Living Polymers on Polymerization with Extremely Productive Ziegler Catalysts," *Angewandte Chemie International Edition in English*, vol. 19, no. 5, pp. 390–392, 1980.

[24] N. Ueyama, T. Araki, and H. Tani, "Behavior of the $R_2AlOAlR_2$ Catalyst in the Polymerization of Propylene Oxide," *Macromolecules*, vol. 7, no. 2, pp. 153 – 160, 1974.

[25] V. Busico, R. Cipullo, and S. Ronca, "Propene/ethene-[1-13C] copolymerization as a tool for investigating catalyst regioselectivity. 1. Theory and calibration," *Macromolecules*, vol. 35, no. 5, pp. 1537–1542, 2002.

[26] P. D. Pletcher, J. M. Switzer, D. K. Steelman, G. A. Medvedev, W. N. Delgass, J. M. Caruthers, and M. M. Abu-Omar, "Quantitative Comparative Kinetics of 1-Hexene Polymerization across Group IV Bis-Phenolate Catalysts," *ACS Catalysis*, vol. 6, no. 8, pp. 5138–5145, 2016.

[27] C. R. Landis and M. D. Christianson, "Metallocene-catalyzed alkene polymerization and the observation of Zr-allyls," *Proceedings of the National Academy of Sciences*, vol. 103, no. 42, pp. 15349–15354, 2006.

[28] B. Lian, K. Beckerle, T. P. Spaniol, and J. Okuda, "Regioselective 1-hexene oligomerization using cationic bis(phenolato) group 4 metal catalysts: Switch from 1,2- to 2,1-insertion," *Angewandte Chemie - International Edition*, vol. 46, no. 44, pp. 8507–8510, 2007.

[29] E. Zurek and T. Ziegler, "Theoretical studies of the structure and function of MAO (methylaluminoxane)," *Progress in Polymer Science*, vol. 29, no. 2, pp. 107–148, 2004.

[30] E. P. Talsi, N. V. Semikolenova, V. N. Panchenko, A. P. Sobolev, D. E. Babushkin, A. A. Shubin, and V. A. Zakharov, "The metallocene/methylaluminoxane catalysts formation: EPR spin probe study of Lewis acidic sites of methylaluminoxane," *Journal of Molecular Catalysis A: Chemical*, vol. 139, no. 2-3, pp. 131–137, 1999.

[31] M. E. Velthoen, J. M. Boereboom, R. E. Bulo, and B. M. Weckhuysen, "Insights into the Activation of Silica-Supported Metallocene Olefin Polymerization Catalysts by Methylaluminoxane," *Catalysis Today*, 2018.

[32] M. E. Z. Velthoen, A. Muñoz-Murillo, A. Bouhmadi, M. Cecius, S. Diefenbach, and B. M. Weckhuysen, "The Multifaceted Role of Methylaluminoxane in Metallocene-Based Olefin Polymerization Catalysis," *Macromolecules*, vol. 51, pp. 343–355, 2018.

[33] A. Alizadeh and T. F. McKenna, "Particle Growth during the Polymerization of Olefins on Supported Catalysts. Part 2: Current Experimental Understanding and Modeling Progresses on Particle Fragmentation, Growth, and Morphology Development," *Macromolecular Reaction Engineering*, vol. 12, no. 1, 2018.

[34] S. J. Conway, J. W. Falconer, and C. H. Rochester, "Chromia / Silica-Titania Cogel Catalysts for Ethene Polymerization," *Journal of Chemical Society, Faraday Transactions 1*, vol. 85, no. 1, pp. 71–78, 1989.

[35] B. Jongsomjit, S. Ngamposri, and P. Praserthdam, "Role of titania in TiO_2/SiO_2 mixed oxides-supported metallocene catalyst during ethylene/1-octene copolymerization," *Catalysis Letters*, vol. 100, pp. 139–146, apr 2005.

[36] R. Riva, H. Miessner, R. Vitali, and G. Del Piero, "Metal–support interaction in Co/SiO_2 and Co/TiO_2," *Applied Catalysis A: General*, vol. 196, no. 1, pp. 111–123, 2000.

[37] J. Niemantsverdriet, "Spectroscopy in Catalysis: An Introduction, Third Edition," pp. 217–249, 2007.

[38] E. Parry, "An infrared study of pyridine adsorbed on acidic solids. Characterization of surface acidity," *Journal of Catalysis*, vol. 2, no. 5, pp. 371–379, 1963.

[39] M. E. Z. Velthoen, A. Muñoz-Murillo, A. Bouhmadi, M. Cecius, S. Diefenbach, and B. M. Weckhuysen, "SI: The Multifaceted Role of Methylaluminoxane in Metallocene-Based Olefin Polymerization Catalysis," *Macromolecules*, pp. 1–18, 2018.

[40] V. N. Panchenko, N. V. Semikolenova, I. G. Danilova, E. A. Paukshtis, and V. A. Zakharov, "IRS study of ethylene polymerization catalyst SiO_2/methylaluminoxane/zirconocene," *Journal of Molecular Catalysis A: Chemical*, vol. 142, no. 1, pp. 27–37, 1999.

[41] C.-P. Sherman Hsu, "Handbook of Instrumental Techniques for Analytical Chemistry," p. 262, 1997.

[42] T. Armaroli, T. Bécue, and S. Gautier, "Diffuse reflection infrared spectroscopy (DRIFTS): Application to the in situ analysis of catalysts," *Oil and Gas Science and Technology*, vol. 59, no. 2, pp. 215–237, 2004.

[43] B. G. Harvey and H. A. Meylemans, "1-Hexene: a renewable C_6 platform for full-performance jet and diesel fuels," *Green Chemistry*, vol. 16, no. 2, pp. 770–776, 2014.

[44] T. Gunasekara, A. Z. Preston, M. Zeng, and M. M. Abu-Omar, "Highly Regioselective α-Olefin Dimerization Using Zirconium and Hafnium Amine Bis(phenolate) Complexes," *Organometallics*, vol. 36, no. 15, pp. 2934–2939, 2017.

[45] D. Harvey, "Analytical Chemistry 2.0," p. 164, 2008.

[46] S. Nie, D. T. Chiu, and R. N. Zare, "Probing Individual Molecules with Confocal Fluorescence Microscopy," *Science*, vol. 266, no. 5187, pp. 1018–1021, 1994.

[47] J. B. Pawley (ed.), "Handbook of Biological Confocal Microscopy," 2006.

[48] J. Lakowicz, "Principles of Fluorescence Spectroscopy," pp. 1–5, 2006.

[49] A. Stanculescu, F. Stanculescu, L. Tugulea, and M. Socol, "Optical Properties of 3,4,9,10-perylenetetracarboxylic dianhydride and 8-hydroxyquinoline Aluminum Salt Films Prepared by Vacuum Deposition," *Materials Science Forum*, vol. 516, pp. 956–960, 2006.

[50] M. Stork, A. Herrmann, T. Nemnich, M. Klapper, and K. Müllen, "Combinatorial testing of supported catalysts for the heterogeneous polymerization of olefins," *Angewandte Chemie - International Edition*, vol. 39, no. 23, pp. 4367–4369, 2000.

[51] Y. J. Jang, C. Naundorf, M. Klapper, and K. Müllen, "Study of the fragmentation process of different supports for metallocenes by laser scanning confocal fluorescence microscopy (LSCFM)," *Macromolecular Chemistry and Physics*, vol. 206, no. 20, pp. 2027–2037, 2005.

[52] J. R. Severn, J. C. Chadwick, R. Duchateau, and N. Friederichs, ""Bound but not gagged" - Immobilizing single-site α-olefin polymerization catalysts," *Chemical Reviews*, vol. 105, no. 11, pp. 4073–4147, 2005.

[53] L. T. Zhuravlev, "Surface characterization of amorphous silica - a review of work from the former USSR," *Colloids and Surfaces A: Physicochemical and Engineering Aspects*, vol. 74, no. 1, pp. 71–90, 1993.

[54] M. Smit, X. Zheng, J. Loos, J. C. Chadwick, and C. E. Koning, "Effects of methylaluminoxane immobilization on silica on the performance of zirconocene catalysts in propylene polymerization," *Journal of Polymer Science, Part A: Polymer Chemistry*, vol. 43, no. 13, pp. 2734–2748, 2005.

[55] A. A. Tsyganenko, E. N. Storozheva, O. V. Manoilova, T. Lesage, M. Daturi, and J. Lavalley, "Brønsted acidity of silica silanol groups induced by adsorption of acids," *Catalysis Letters*, vol. 70, pp. 159–163, 2000.

[56] O. Y. Lyakin, K. P. Bryliakov, V. N. Panchenko, N. V. Semikolenova, V. A. Zakharov, and E. P. Talsi, "EPR identification of Zr(III) complexes formed upon interaction of (2-PhInd)$_2$ZrCl$_2$ and rac-Me$_2$Si(1-Ind)$_2$ZrCl$_2$ with MAO and MMAO," *Macromolecular Chemistry and Physics*, vol. 208, no. 11, pp. 1168–1175, 2007.

[57] J. N. Pédeutour, K. Radhakrishnan, H. Cramail, and A. Deffieux, "Reactivity of metallocene catalysts for olefin polymerization: Influence of activator nature and structure," *Macromolecular Rapid Communications*, vol. 22, no. 14, pp. 1095–1123, 2001.

[58] E. B. Faulkner and R. J. Schwartz, "High Performance Pigments," pp. 261–274, 2009.

[59] R. P. D'Amelia, S. Gentile, W. F. Nirode, and L. Huang, "Quantitative Analysis of Copolymers and Blends of Polyvinyl Acetate (PVAc) Using Fourier Transform Infrared Spectroscopy (FTIR) and Elemental Analysis (EA)," *World Journal of Chemical Education, Vol. 4, 2016, Pages 25-31*, vol. 4, no. 2, pp. 25–31, 2016.

[60] Z. Ristanović, M. M. Kerssens, A. V. Kubarev, F. C. Hendriks, P. Dedecker, J. Hofkens, M. B. Roeffaers, and B. M. Weckhuysen, "High-resolution single-molecule fluorescence imaging of zeolite aggregates within real-life fluid catalytic cracking particles," *Angewandte Chemie - International Edition*, vol. 54, no. 6, pp. 1836–1840, 2015.

[61] C. Willocq, A. Vantomme, and M. Slawinksi, "European Pat. 2588501 B1 (Modified catalyst supports)," 2011.

[62] E. Román, M. Barrera, S. Hernández, and E. Lissi, "Photochemistry and emission behaviour of the iron(II) mixed metallocene complexes [C$_5$R$_5$Fe(arene)]PF$_6$ (R=H or Me)," *Journal of the Chemical Society, Perkin Transactions 2*, no. 6, p. 939, 1988.

[63] H. Sitzmann, T. Dezember, O. Schmitt, F. Weber, G. Wolmershäuser, and M. Ruck, "Reactions of free cyclopentadienyl radicals. 3 Metallocenes of samarium, europium, and ytterbium with the especially bulky cyclopentadienyl ligands $C_5H(CHMe_2)_4$, $C_5H_2(CMe_3)_3$, and $C_5(CHMe_2)_5$," *Zeitschrift fur Anorganische und Allgemeine Chemie*, vol. 626, no. 11, pp. 2241–2244, 2000.

[64] N. Mäkelä-Vaarne, "Characterisation of Group 4 Metallocenes and Metallocene Catalysts - UV/VIS Spectroscopic Study," 2003.

[65] D. Coevoet, H. Cramail, and A. Deffieux, "U.V./visible spectroscopic study of the rac-$Et(Ind)_2ZrCl_2$/MAO olefin polymerization catalytic system, investigation in toluene," *Macromolecular Chemistry and Physics*, vol. 199, pp. 1451–1457, 1998.

Appendix

Appendix A: ^{1}H-NMR

This page contains the ^{1}H-NMR spectra as result of the polymerization testing procedures. Figure I.51 shows the spectra of 0%Ti at both the starting point and after 60 minutes of polymerization, while Figure I.52 shows the same time interval for 4%Ti.

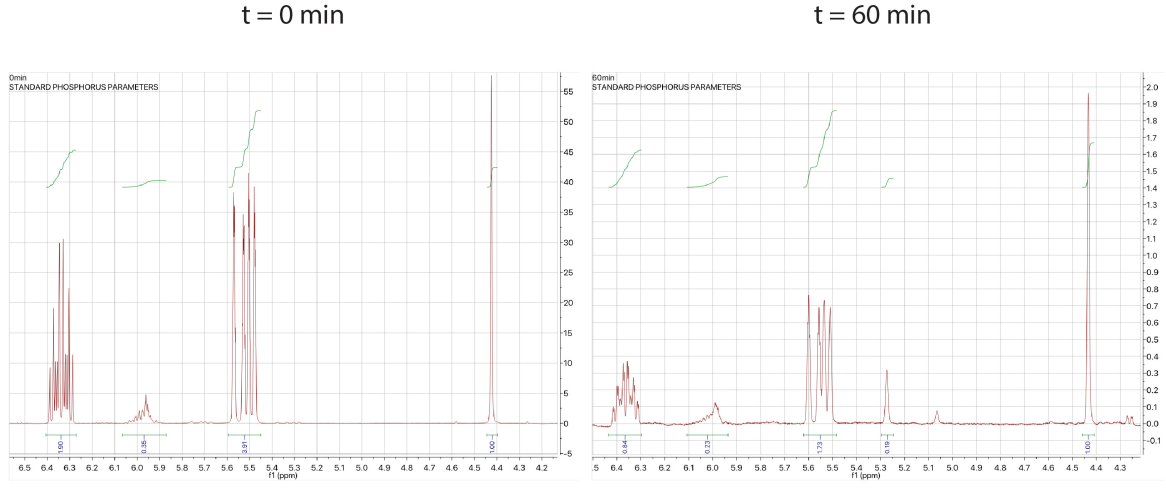

Figure I.51: ^{1}H-NMR spectra for the SiO_2-supported catalyst, before and after 60 minutes of polymerization.

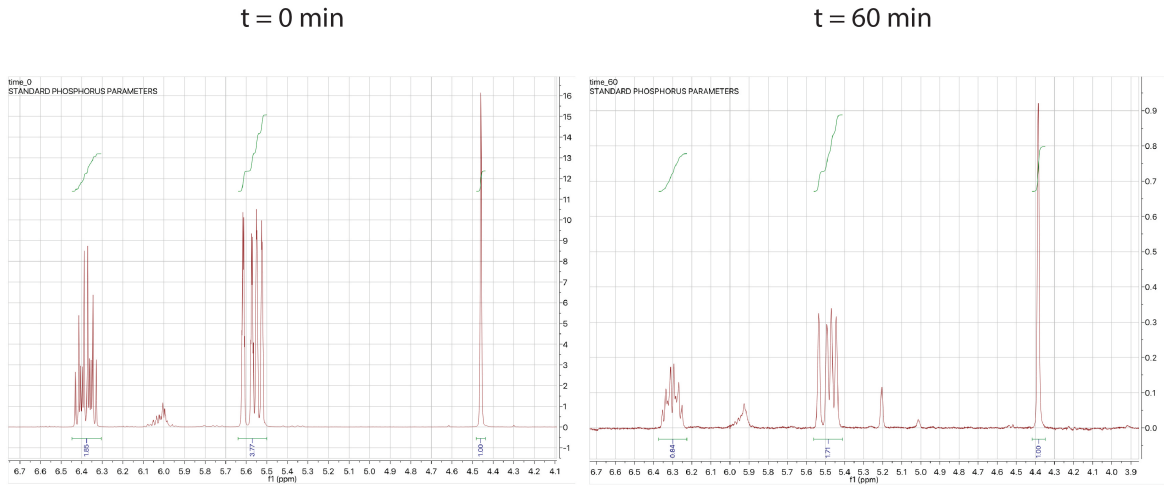

Figure I.52: ^{1}H-NMR spectra for the 4%Ti catalyst, before and after 60 minutes of polymerization.

Appendix B: ^{2}H-NMR

This page contains the ^{2}H-NMR spectra as result of the polymerization testing procedures. Figure I.51 shows the spectra of 0%Ti at the initial volume and after either 1 and 2 additions of 5 μl deuterated dichloromethane. The peaks were attributed in Figure 3.20 on page 28 and all used for the calculation of amount of active sites.

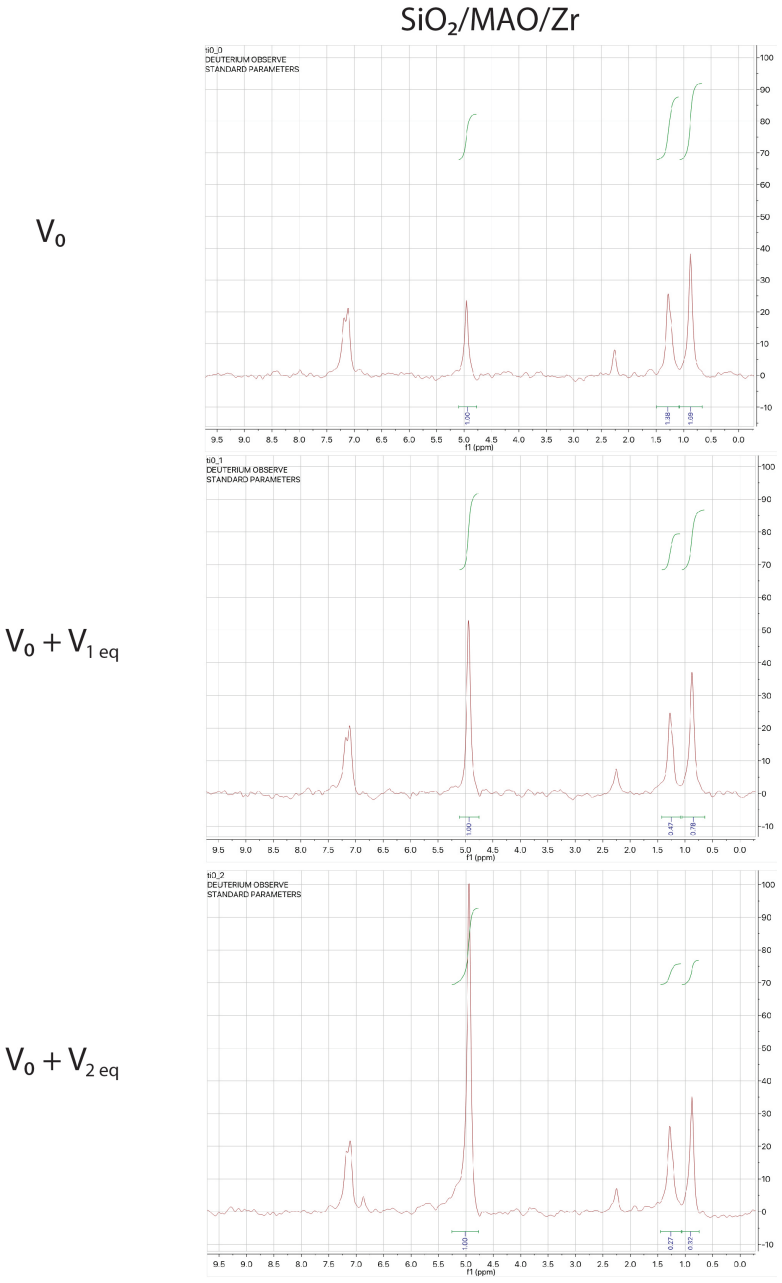

Figure I.53: ^{2}H-NMR spectra for the SiO_2-supported catalyst, at the initial volume and after either 1 and 2 additions of dichloromethane.

This page contains ^{2}H-NMR spectra as result of the polymerization testing procedures. Figure I.52 shows the same volume interval for 4%Ti, as presented on the previous page. The peaks were attributed in Figure 3.20 on page 28 and all used for the calculations of amount of active sites.

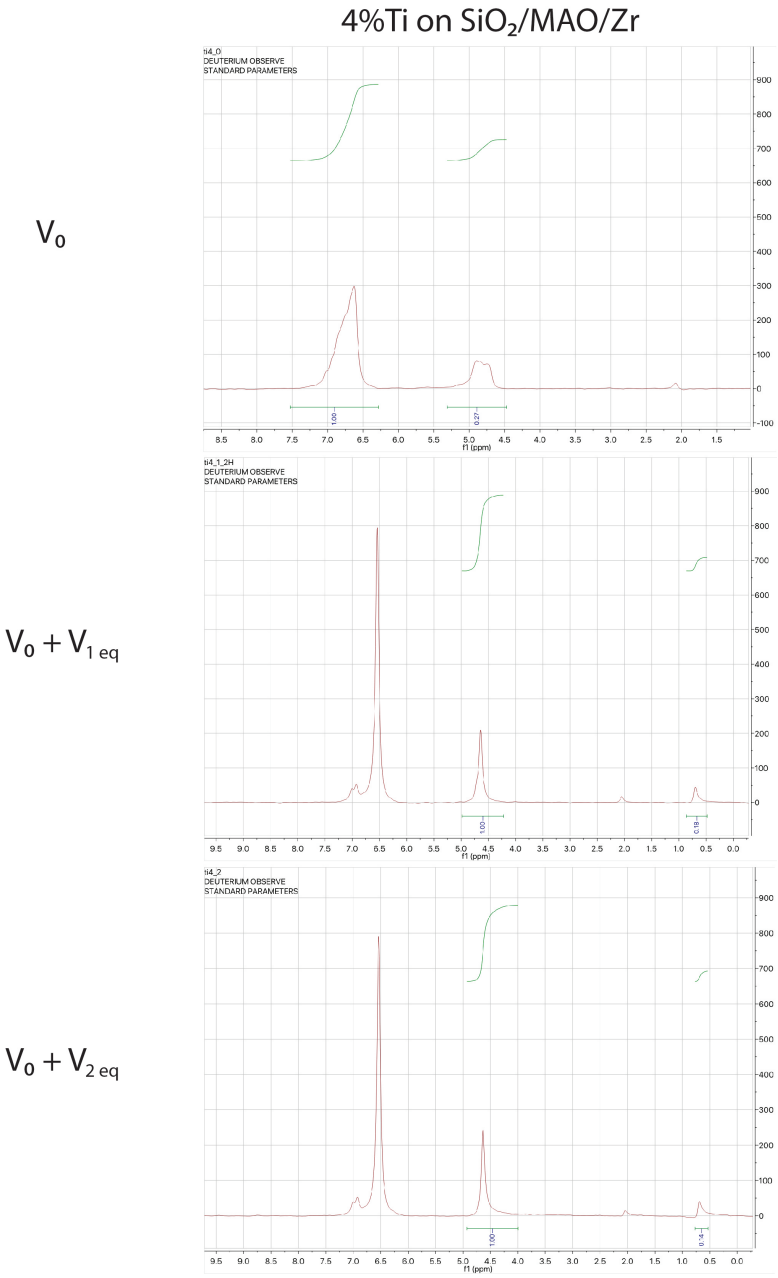

Figure I.54: ^{2}H-NMR spectra for the 4%Ti catalyst, at the initial volume and after either 1 and 2 additions of dichloromethane.

Appendix C: Mathematica code

The following script shows the Mathematica code that was used to calculate the area and concentration of acid sites after performing pyridine FTIR spectroscopy. The first line of code contains the region in which the peak used to quantify the acidity is located (in between 1440 and 1460 cm^{-1}). The second line calculates the minimum of all the y-values in that range. Followed by a few lines of code that are used to normalize (line 3) and integrate (line 5) the data. The data points (1440.57 and 1459.37) are chosen since they comprise the largest range possible within the data set. Line 6 and 7 are included to check whether the region of integration is correct. Finally, the final line of code shows the calculation of the concentration of acid sites. The area is the result from the integration, where A0 and the rho are two values based on the equation proposed by Panchenko *et al.* on page 24 [40].

```
acidsites4 = Select[data4[[6]], 1440 < #[[1]] < 1460 &];
min4 = Min[acidsites4[[All, 2]]];
acidsites4a = {acidsites4[[All, 1]], acidsites4[[All, 2]] - min4}^T;
interpolation4 = Interpolation[acidsites4a, InterpolationOrder → 1];
area4 = NIntegrate[interpolation4[x], {x, 1440.57, 1459.37}];
ListPlot[acidsites4]
ListPlot[acidsites4a]
acidsites4b = (area4 * 1000) / (A0 * rho) "umol/g on SiO2MAO1017"
```

Appendix D: SEM

Next to studying the structural differences before and after polymerization, SEM was used to study the morphology of the stained samples. As shown in the CFM results on page 53, the particles were disintegrated after stirring with a magnetic bar. This is shown in Figure I.55, where the particle disintegration is evident. The spherical shape of the particles is destroyed, which resulted in the omitting of the magnetic stirring procedure for the staining of the catalyst samples.

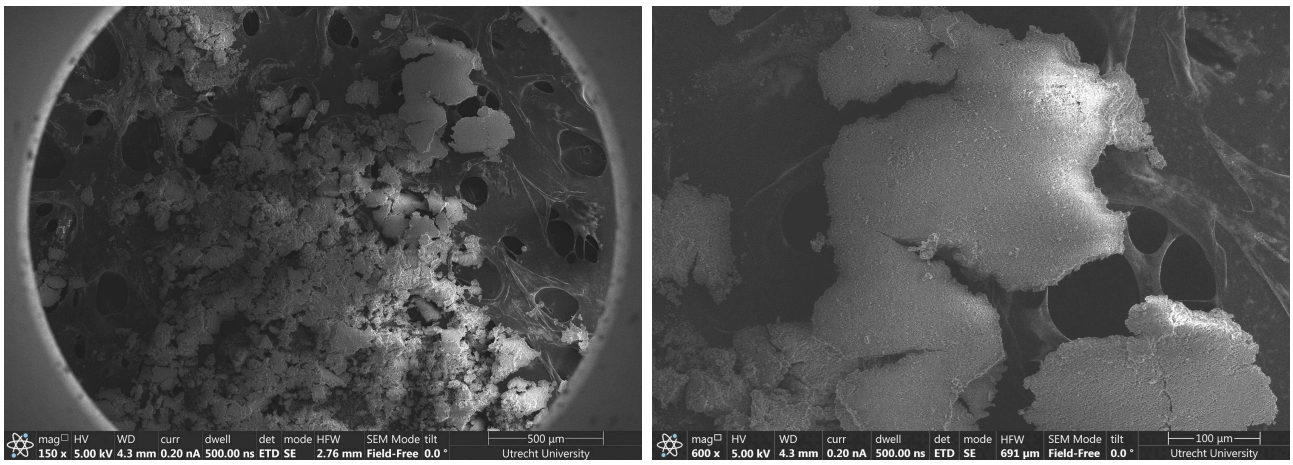

(a) **(b)**

Figure I.55: SEM images that shows a stained catalyst that is prepared by stirring with a stirring bar. Image (a) gives an overview of the disintegrated particles, where (b) shows a zoom-in of these disintegrated particles.

Appendix E: Optical Microscopy

Optical Microscopy was used as complementary technique to Confocal Fluorescence Microscopy, which helped proving the local clustering of the PTCDA dye. Figure I.56 shows the catalyst particles after autoclave polymerization, which resulted in the formation of polyethylene. However, as can be seen from both (a) and (b) is that the red particles seem to be clustered and on the outside of the particles, instead of homogeneously diffused throughout the particle.

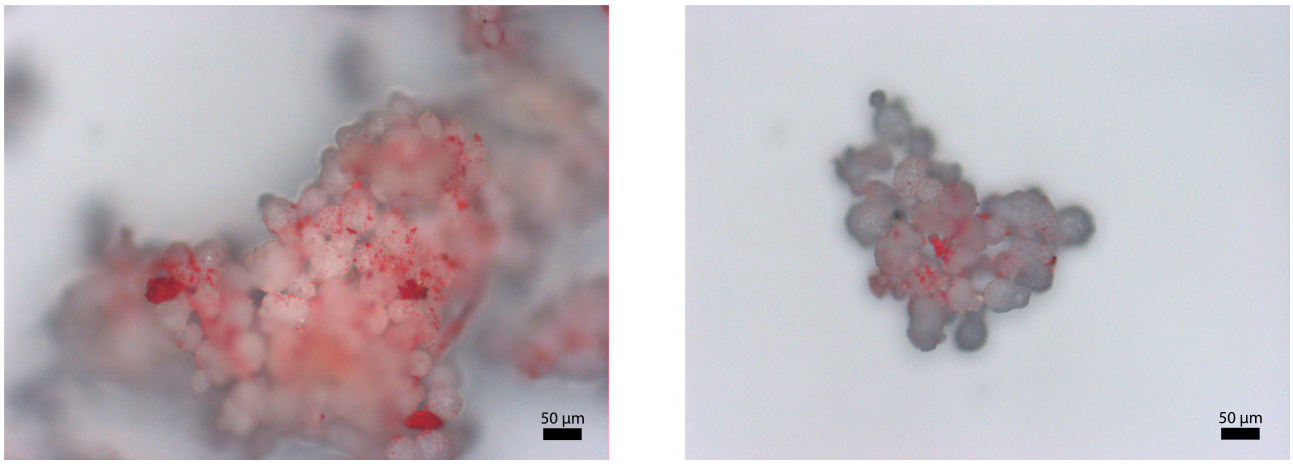

(a) **(b)**

Figure I.56: Optical Microscopy results of the NT 2%Ti on SiO_2/MAO/Zr stained samples, after the autoclave polymerization. Both samples were stained with the PTCDA dye.

Appendix F: ATR-IR

The following graphs present the results from the ATR-IR measurement performed on the samples after ethylene polymerization. The first graph, Figure I.57, shows the results after autoclave polymerization with the directly stained catalyst. The peaks, present at 2916 cm^{-1} and 2849 cm^{-1}, are corresponding to the asymmetric and symmetric CH_2 stretching vibrations of polyethylene.

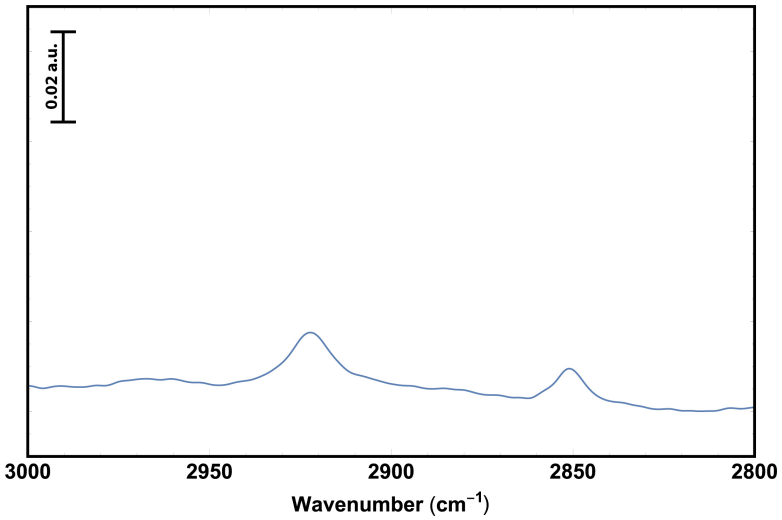

Figure I.57: ATR-IR graph of the CH_2 stretching vibration region of polyethylene, which is observed after autoclave polymerization in the NT 2%Ti on SiO2/MAO/Zr catalyst sample stained with PTCDA via the direct staining method.

Next to that, Figure I.58 shows the results after autoclave polymerization at 30 bar of ethylene pressure. The polymerization was performed with a catalyst stained via the bottom-up staining method.

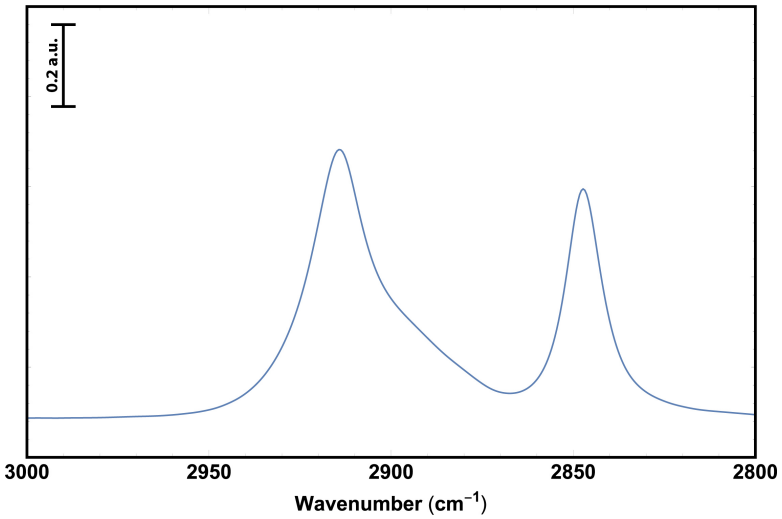

Figure I.58: ATR-IR graph of the CH_2 stretching vibration region of polyethylene, which is observed after autoclave polymerization in the SiO2/MAO/Zr catalyst sample stained with PTCDA via the bottom-up staining method.

Appendix G: FTIR

The FTIR measurements were performed to study the vibrational differences after staining of the support. As can be seen, the 375°C-dried support (green line) has a higher area around the 3700 cm^{-1} region, when comparing to the 450°C-dried support (blue line). This indicates a higher amount of silanols left. Next to that, the vibrational results from the staining of the samples is shown. The perylene-stained support (yellow line) exhibits spectral similarities to the pure support, while the PTCDA-stained support (red line) has spectral changes in the 1750-1500 cm^{-1} region. This is due to the C=O and C=C stretching vibrations, respectively.

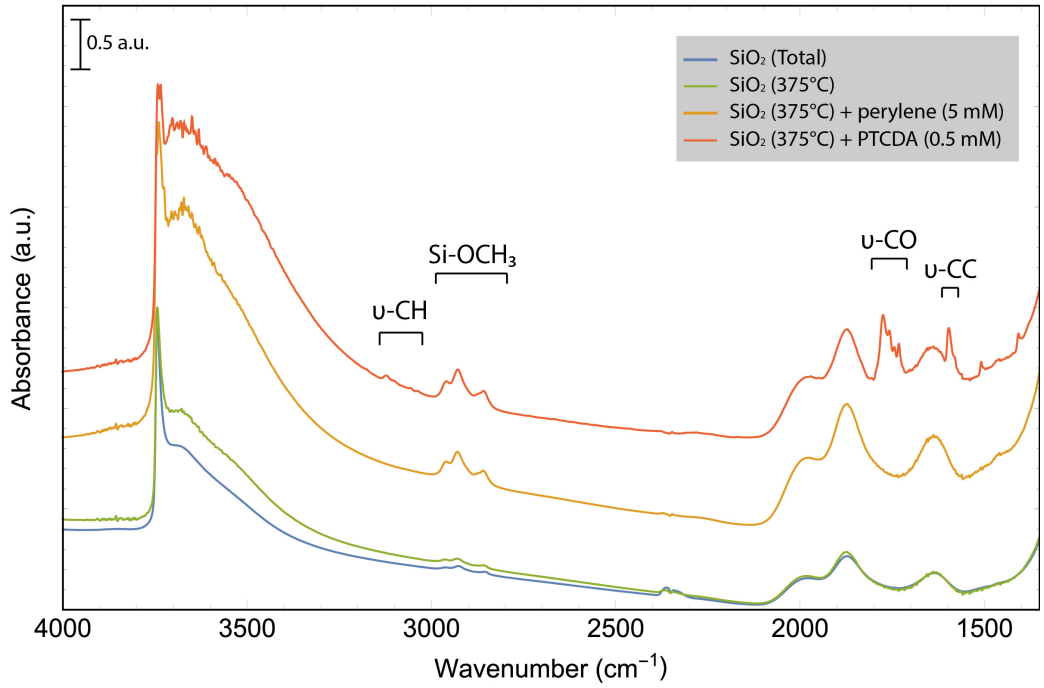

Figure I.59: FTIR results of the SiO_2 supports, before (green line) and after staining with both perylene (yellow line) and PTCDA (red line). The support used normally for the synthesis of the catalyst (blue line) is shown as reference.

Appendix H: CFM

Figure I.60 represents the top surface corresponding to the particles that were reconstructed in three dimensions as depicted in Figure 5.49 on page 59.

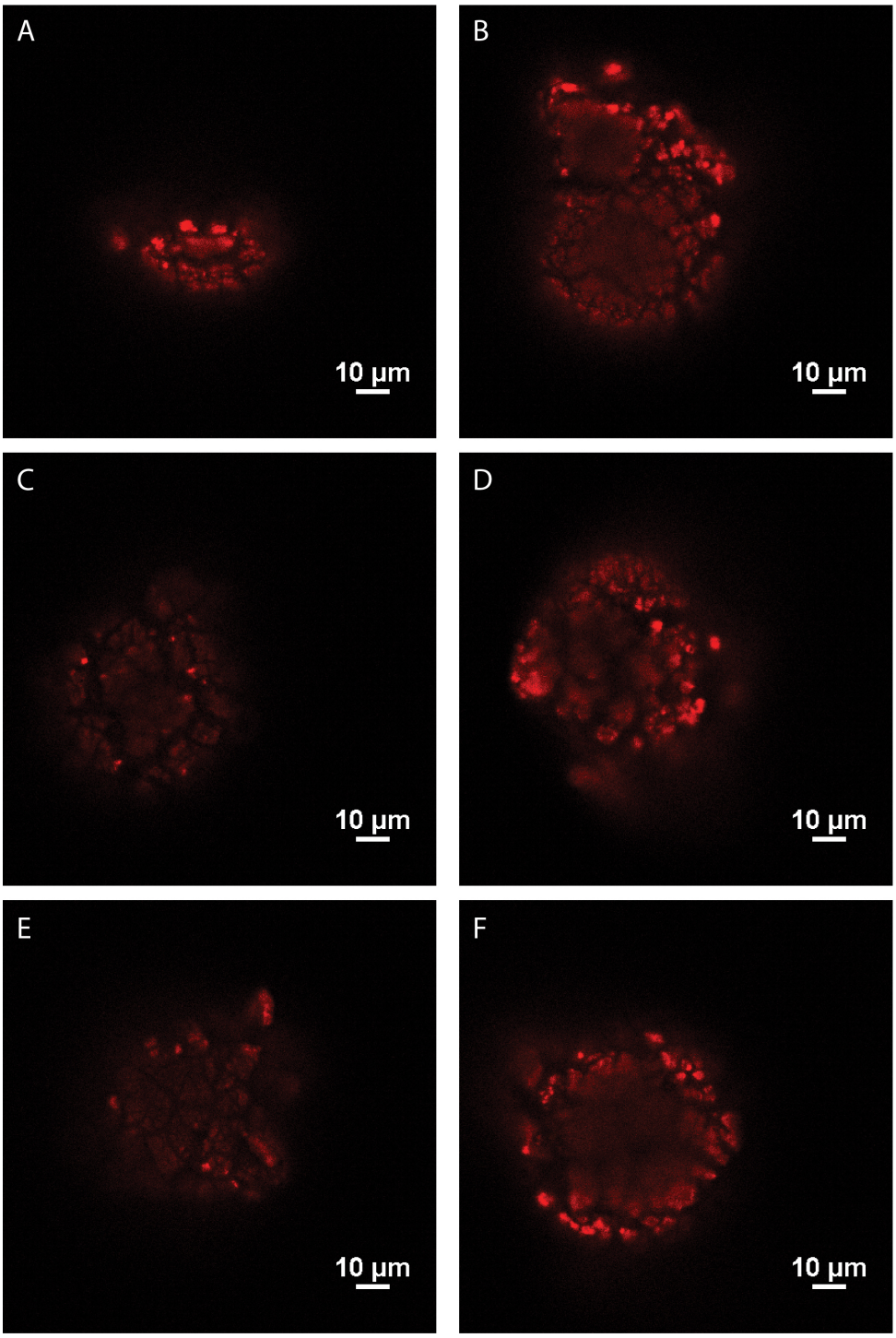

Figure I.60: CFM results of the PTCDA stained catalyst samples, prepared via the bottom-up staining method. The catalyst samples were studied after autoclave polymerization at 30 bar of ethylene pressure. Each image represents an individual fragmented particle.